

# **Strong Electron Correlations in the Ruthenates**

*A Spectroscopic Study of Ca<sub>2</sub>RuO<sub>4</sub> and Ca<sub>1.8</sub>Sr<sub>0.2</sub>RuO<sub>4</sub>*

---

## **Dissertation**

zur

Erlangung der naturwissenschaftlichen Doktorwürde  
(Dr. sc. nat.)

vorgelegt der  
Mathematisch-naturwissenschaftlichen Fakultät  
der  
**Universität Zürich**  
von

**Denys Sutter**  
aus Zeglingen BL und Basel Stadt

### **Promotionskommission**

Prof. Dr. Johan Chang (Vorsitz),  
Dr. Moritz Hoesch und  
Prof. Dr. Jürg Osterwalder

Zürich, 2019



## Abstract

Strongly correlated systems form a class of materials for which textbook quantum many-body theories for non- or weakly-interacting particles fail. Such systems typically exhibit a plethora of exotic ground states that emerge from a competition of electronic and magnetic orders. Below a certain onset temperature, instabilities of the Fermi sea occur that are characterized by a gap energy scale. A paradigmatic electronic instability in strongly correlated matter is the transition from a metal to a Mott-insulator – a phenomenon that a Hartree-Fock single-electron treatment fails to describe. In the Hubbard model, a strong Coulomb repulsion is mainly responsible for the formation of the Mott-insulating state. However, the extent of complexity proliferates with the multi-orbital nature of ruthenates. In these systems, orbital and spin degrees of freedom are influenced by a competition between two additional energy scales. As the crystal field lifts the degeneracy of the  $t_{2g}$  manifold, favouring orbital polarisation, Hund's coupling – associated with intra-atomic exchange – tends to equalize orbital populations. In recent years, Hund's coupling entered the stage of strong correlation research with a leading role.

This dissertation is an experimental study of two single-layered ruthenate compounds,  $\text{Ca}_2\text{RuO}_4$  and  $\text{Ca}_{1.8}\text{Sr}_{0.2}\text{RuO}_4$ . Both materials are surrounded by controversy regarding the nature of their ground state, in conjunction with an apparent orbital-selective Mott transition, promoted by Hund's coupling. Progress has been impeded by the lack of experimental knowledge about the band structure. Here, new insights are presented by resolving the low-energy electronic structure with angle-resolved photoemission spectroscopy, supported by ab-initio band structure calculations. The importance of Hund's coupling will be shown to be evident as it highlights aspects of orbital-selective behaviour in the  $\text{Ca}_{2-x}\text{Sr}_x\text{RuO}_4$  family. With this work, a resolution to some previous altercations is offered with a fresh view on the problem of orbital-selective physics in multi-orbital strongly correlated matter.

# List of abbreviations and acronyms

## Constants and variables

$\gamma$	Sommerfeld constant
$C^+$	Circular light polarisation
$d_{\gamma z}$	Out-of-plane $d$ -orbitals ( $d_{xz}$ and $d_{yz}$ )
$\varepsilon_{\mathbf{k}}^b$	Electron bare band energy
$\varepsilon_{\mathbf{k}}^q$	Quasiparticle excitation energy
$E_B$	Binding energy
$E_F$	Fermi energy
$\hbar$	Planck constant $\hbar/2\pi = 6.582119514 \times 10^{-34}$ eV s
$J_H$	Hund's coupling
$k_B$	Boltzmann constant $= 8.611733 \times 10^{-5}$ eV K $^{-1}$
$\lambda_{\text{IMFP}}$	Inelastic mean free path
$m_b$	Bare band electron mass
$m_e$	Free electron mass $= 5.68563 \times 10^{-32}$ eV s $^2/\text{\AA}^2$
$m^*$	Effective electron mass
$\Phi$	Material specific work function
$\bar{\pi}$	Light polarisation parallel to mirror plane
$\rho_{\text{res}}$	Residual resistivity
$\bar{\sigma}$	Light polarisation perpendicular to mirror plane
$T_c$	Critical superconducting transition temperature
$T_C$	Curie temperature
$T_{\text{FL}}$	Fermi liquid coherence temperature
$T_N$	Néel temperature
$T_S$	Structural transition temperature
$U$	Coulomb interaction
$U_c$	Critical Coulomb interaction for Mott localization
$v_b$	Bare band Fermi velocity
$v_F$	Fermi velocity
$\omega$	Excitation energy
$Z$	Quasiparticle residue / weight

---

## Functions

$\mathcal{A}(\mathbf{k}, \omega)$	Spectral function
$f(\omega, T)$	Fermi-Dirac distribution = $(e^{(\omega-\mu)/k_B T} + 1)^{-1}$
$\mathcal{G}(\mathbf{k}, \omega)$	Green's function
$\mathcal{H}$	Hamiltonian
$\mathcal{R}(\Delta\omega)$	Resolution function
$\Sigma(\mathbf{k}, \omega)$	Self-energy

## Abbreviations

ARPES	Angle-resolved photoemission spectroscopy
CMR	Colossal magnetoresistance
BCS	Theory for superconductivity by Bardeen, Cooper and Schrieffer
DFT	Density functional theory
DMFT	Dynamical mean-field theory
DOS	Density of states
EDC	Energy distribution curve
FL	Fermi liquid
FS	Fermi surface
HTSC	High temperature superconductivity
LDA	Local density approximation
LHB	Lower Hubbard band
MDC	Momentum distribution curve
MIT	Metal-insulator transition
nFL	non-Fermi liquid
OSMP	Orbital-selective Mott phase
OSMT	Orbital-selective Mott transition
QCP	Quantum critical point
QP	Quasiparticles
SC	Superconductivity
TBA	Tight binding approximation
UHB	Upper Hubbard band
vHs	Van-Hove Singularity



# Table of contents

<b>1</b>	<b>Introduction</b>	<b>1</b>
1.1	Strongly correlated systems . . . . .	2
1.2	Ruthenates: General aspects . . . . .	5
1.2.1	Infinite-layered compounds . . . . .	6
1.2.2	Tri-layered compounds . . . . .	7
1.2.3	Bi-layered compounds . . . . .	8
1.3	Single-layered $\text{Ca}_{2-x}\text{Sr}_x\text{RuO}_4$ . . . . .	10
1.3.1	$\text{Sr}_2\text{RuO}_4$ ( $x = 2$ ) . . . . .	11
1.3.2	$\text{Ca}_{1.5}\text{Sr}_{0.5}\text{RuO}_4$ ( $x = 0.5$ ) . . . . .	12
1.3.3	$\text{Ca}_{1.8}\text{Sr}_{0.2}\text{RuO}_4$ ( $x = 0.2$ ) . . . . .	13
1.3.4	$\text{Ca}_2\text{RuO}_4$ ( $x = 0$ ) . . . . .	14
1.4	Outline of the thesis . . . . .	15
<b>2</b>	<b>Concepts in condensed matter physics</b>	<b>17</b>
2.1	Many-body physics . . . . .	17
2.1.1	Green's function . . . . .	17
2.1.2	Quasiparticle residue . . . . .	19
2.2	Fermi liquid quasiparticles . . . . .	20
2.3	Non-Fermi liquids . . . . .	23
2.4	Mott physics . . . . .	24
2.5	Hund's coupling . . . . .	27
2.6	Band structure calculations . . . . .	28
2.6.1	Tight binding approximation . . . . .	28
2.6.2	Density functional theory . . . . .	33
2.6.3	Dynamical mean field theory . . . . .	35
<b>3</b>	<b>Concepts in photoemission spectroscopy</b>	<b>37</b>
3.1	Photoemission process . . . . .	38

3.1.1	Step one: Optical excitation . . . . .	39
3.1.2	Step two: Propagation to the surface . . . . .	41
3.1.3	Step three: Transmission into vacuum . . . . .	42
3.2	Experiment . . . . .	44
3.2.1	EDC's and MDC's . . . . .	44
3.2.2	Angles to $k$ -space conversion . . . . .	45
3.2.3	Matrix element effects . . . . .	47
3.2.4	Sample preparation . . . . .	47
3.2.5	Experimental environment . . . . .	49
3.2.6	Background and resolution . . . . .	52
<b>4</b>	<b>Orbital-selective Fermi liquid <math>\text{Ca}_{1.8}\text{Sr}_{0.2}\text{RuO}_4</math></b>	<b>55</b>
4.1	Introduction . . . . .	55
4.2	Methods . . . . .	57
4.2.1	Experimental . . . . .	57
4.2.2	Band structure calculations . . . . .	58
4.3	Results . . . . .	58
4.3.1	Low-energy band structure . . . . .	58
4.3.2	Orbital characters . . . . .	60
4.4	Discussion . . . . .	63
4.4.1	Band filling . . . . .	63
4.4.2	Self-energy analysis . . . . .	64
4.4.3	Temperature dependence . . . . .	66
4.5	Conclusions . . . . .	71
<b>5</b>	<b>Nature of the Mott insulator <math>\text{Ca}_2\text{RuO}_4</math></b>	<b>73</b>
5.1	Introduction . . . . .	73
5.2	Methods . . . . .	75
5.2.1	Experimental . . . . .	75
5.2.2	Band structure calculations . . . . .	75
5.3	Results . . . . .	75
5.3.1	Oxygen bands . . . . .	75
5.3.2	Ruthenium bands . . . . .	77
5.3.3	Orbital characters . . . . .	77
5.4	Discussion . . . . .	80
5.4.1	Phenomenological modeling . . . . .	80
5.4.2	DMFT and multiplet analysis . . . . .	82

---

Table of contents	ix
5.5 Conclusions . . . . .	85
<b>6 Conclusions &amp; Outlook</b>	<b>87</b>
<b>Appendix A Low-energy band structure of Ca<sub>1.7</sub>Sr<sub>0.3</sub>RuO<sub>4</sub></b>	<b>89</b>
<b>Appendix B Matrix element effects in Ca<sub>2</sub>RuO<sub>4</sub></b>	<b>91</b>
<b>Appendix C Drawings PSI sample transportation</b>	<b>93</b>
<b>References</b>	<b>97</b>



# Chapter 1

## Introduction

Essentially all technological advances in the history of human mankind – from the stone age to modern times – can be traced to new understandings or usage of materials. This ranges from the advent of metal working and tool making to silicon based inventions leading inadvertently to consecutive technological revolutions that shape our worldly experience. A main pillar of modern science is the field of condensed matter physics that is devoted to the study of solids and liquids. In our every-day lives we are permanently surrounded by matter that consists of an immensely large ensemble of interacting particles. Often times, such ensembles order electronically or magnetically in rather complex fashions. Although elementary particles obey microscopic laws, fundamentally new states of matter can emerge due to their mutual interactions [1]. In principle, all physical properties of a many-particle system can be accessed by its wavefunction  $\Psi(\mathbf{X}, \mathbf{x})$  via solving the Schrödinger equation

$$\mathcal{H}\Psi(\mathbf{X}, \mathbf{x}) = E\Psi(\mathbf{X}, \mathbf{x}), \quad (1.1)$$

where  $\mathbf{X}$  and  $\mathbf{x}$  are the space and spin coordinates of all nuclei and electrons of the system. The Hamiltonian is given by

$$\mathcal{H} = T_e + T_n + V_{ee} + V_{en} + V_{nn}, \quad (1.2)$$

where  $T_e$  and  $T_n$  represent the kinetic energy of the electrons and nuclei (with atomic number  $Z$ ), and  $V_{ee}$ ,  $V_{en}$  and  $V_{nn}$  indicate electron-electron, electron-nuclei and nuclei-nuclei interactions. In the non-relativistic approximation and by ignoring spin-spin interactions, we can write the Hamiltonian as

$$\mathcal{H} = - \sum_i \frac{\hbar^2}{2m_e} \nabla_i^2 - \sum_{\alpha} \frac{\hbar^2}{2M_{\alpha}} \nabla_{\alpha}^2 + \sum_{i < j} \frac{e^2}{|\mathbf{r}_i - \mathbf{r}_j|} - \sum_{\alpha, i} \frac{Z_{\alpha} e^2}{|\mathbf{R}_{\alpha} - \mathbf{r}_i|} + \sum_{\alpha < \beta} \frac{Z_{\alpha} Z_{\beta} e^2}{|\mathbf{R}_{\alpha} - \mathbf{R}_{\beta}|}, \quad (1.3)$$

where  $M_{\alpha}$ ,  $\mathbf{R}_{\alpha}$ ,  $\mathbf{R}_{\beta}$  are the masses and positions of the nuclei and  $m_e$ ,  $\mathbf{r}_i$ ,  $\mathbf{r}_j$  are the masses and positions of the electrons respectively. Since typical many-body systems involve  $\mathcal{O}(23)$  particles, solving the Schrödinger equation with said Hamiltonian is not feasible. Progression is made through certain simplifications depending on the specific problem. In the past century, powerful computational and theoretical tools have been developed in order to treat many-body effects (Hartree-Fock approximation, Landau's Fermi liquid theory, density functional theory, etc.).

## 1.1 Strongly correlated systems

In 1911, Heike Kamerlingh Onnes observed a sudden disappearance of electrical resistance in mercury below a certain transition temperature  $T_c$  – superconductivity (SC) has been discovered [2] (Nobel prize 1913). Almost five decades later, this phenomenon was explained in 1957 by John Bardeen, Leon Cooper, and John Robert Schrieffer (BCS theory) [3] and is widely regarded as one of the most elegant theories ever formulated in condensed matter physics (Nobel prize 1972). The key in BCS theory is a delicate net attraction of conduction electrons, mediated by crystal lattice vibrations. This subset of electrons form *Cooper-pairs*, obeying Bose-Einstein statistics as spin-singlets and condense into a single quantum state. BCS theory predicts an upper boundary for the superconducting transition temperature, set by the strength of the electron-phonon interaction and the Debye temperature. Historically, superconductivity above 30 K has not been expected. Therefore, it came as a big sensation when 1986 SC has been found in copper-based perovskite-type ceramics with a  $T_c$  well above typical BCS critical temperatures [4], that soon after exceeded the boiling point of nitrogen [5, 6]. Georg Bednorz and Karl Alex Müller (who lectured at the University of Zurich) received the Nobel prize for their discovery of high- $T_c$  superconductivity (HTSC) only one year later. The dream of SC at room temperature was reignited and lead to a tremendous boost in research activity (see Fig. 1.1). However, to this date, the exact mechanisms of HTSC remains one of the biggest unresolved mystery of nature.

The enormous efforts in HTSC research was accompanied by a rapidly growing interest in oxide compounds that host transition metals or rare earth atoms with partially

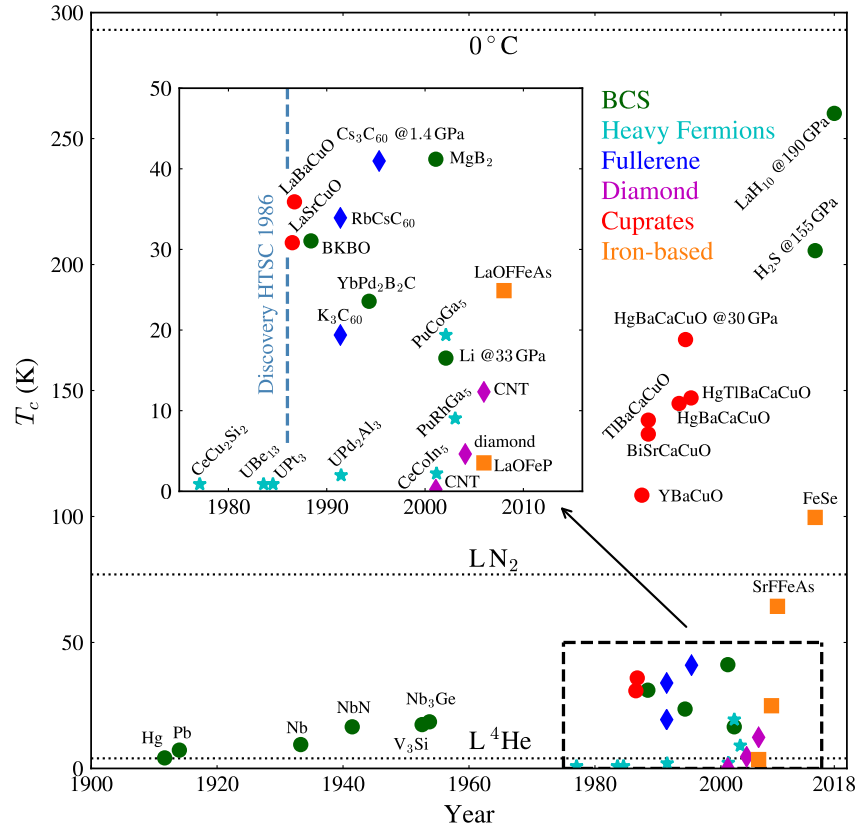


**Fig. 1.1** Timeline of  $T_c$ 's reached over time of different compounds. Color code is given in the figure. Dotted lines mark  $0^\circ\text{C}$ , the evaporation temperature of liquid nitrogen (77 K) and liquid helium (4.2 K) at 1 atmosphere pressure. The inset is a zoom on the region, indicated by the dashed lines.

filled  $d$ - or  $f$ -shells. Particularly interesting is the Ruddlesden-Popper phase of the form  $\text{A}_{n+1}\text{B}_n\text{O}_{3n+1}$ , where A and B are cations and O is oxygen. There, a spacer layer intrudes the crystal structure after every  $n$  layers of the  $\text{ABO}_3$  perovskite lattice (see Fig. 1.2). Typically, A has a large atomic radius (e.g. La or Sr) and B is a transition metal in a  $\text{BO}_6$  octahedron (e.g. Mn, Ni, Co, Cu). Often these systems exhibit strong electron correlations and generate exotic states of matter. From this field of condensed matter physics many relevant technological developments and applications followed. For example, read heads of data-storage devices make use of the colossal magnetoresistance (CMR) in manganites [7, 8] (Nobel prize 2007 for the discovery of the giant magnetoresistance (GMR) in Fe/Cr films). In cobaltates a large thermopower and water-induced superconductivity are found [9–11].

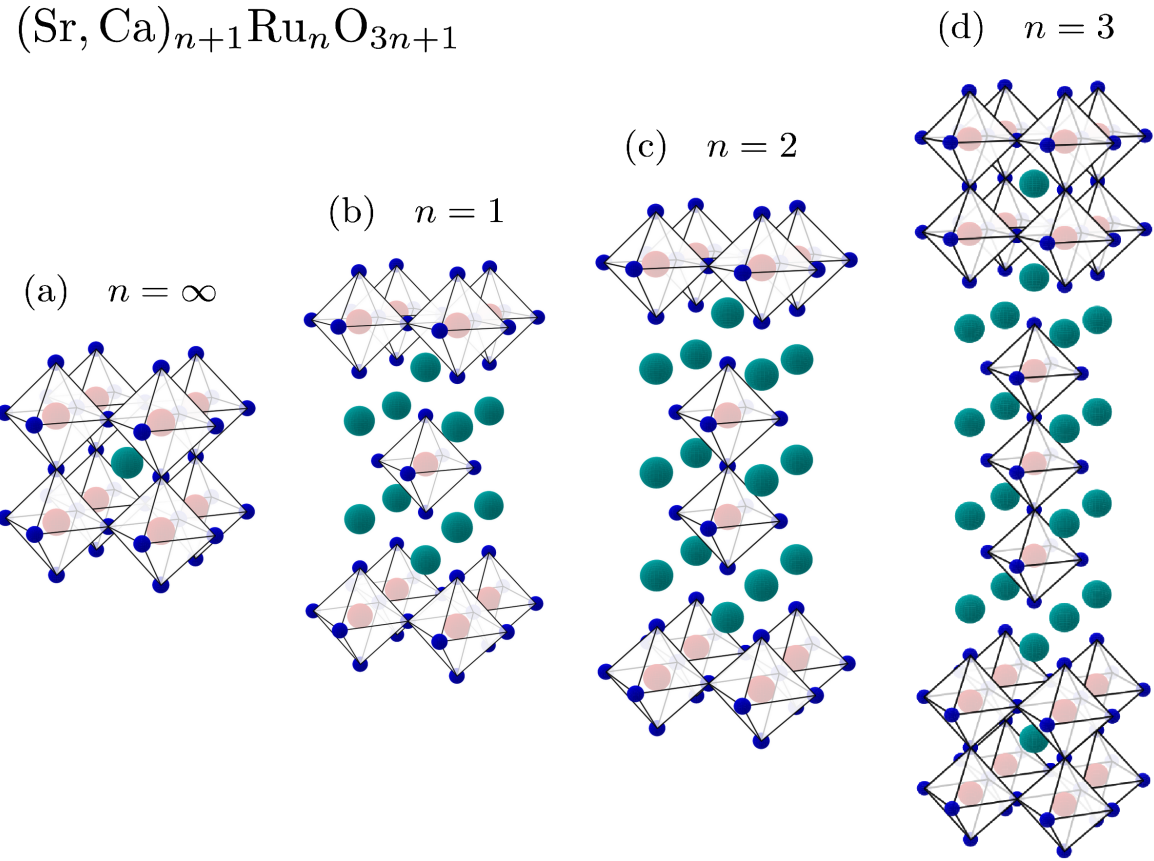


**Fig. 1.2** Illustration of the (tetragonal) Ruddlesden-Popper phases  $(\text{Sr, Ca})_{n+1}\text{Ru}_n\text{O}_{3n+1}$  for  $n = \{\infty, 1, 2, 3\}$ . The oxygen-octahedra enclose each a Ru atom and Sr or Ca atoms are located between the layers.

The most prominent representative of strongly correlated electrons are Mott-insulators. Already in 1938, the significance of electron correlations was noticed when the metal-insulator transition (MIT) in nickelates has been explained [12, 13]. Research activity steered towards controlling magnetic properties and the MIT of rare-earth nickelates via heterostructure architectures, epitaxial strain, doping or quantum confinement [14, 15]. Mott-insulators are systems predicted to be metallic from a band-theory perspective but are in fact insulating due to Coloumb repulsion [16, 17]. Typically, HTSC emerges through (electron- or hole-) doping a Mott-insulating parent compound [18, 19]. In this way, Mott-insulators gained a lot of attention and have been considered a paradigmatic phenomenon in the field of strongly correlated electrons. In recent years, however, it became apparent that Hund's coupling  $J_H$  (associated to intra-atomic exchange) plays a significant role in multi-orbital materials with strong correlations [20]. The importance of Hund's coupling has been reinforced with the discovery of (multi-orbital)

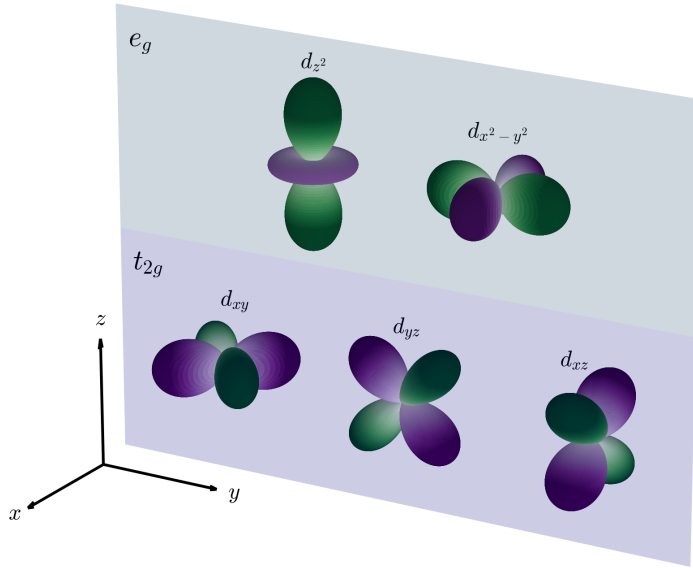


**Fig. 1.3** Degeneracy lifting in an octahedral crystal field. The  $e_g$ -states are higher in energy than the  $t_{2g}$ -orbitals.

iron-based superconductors in 2008 [21] and the description of spin and electronic degrees of freedom in the ruthenates [20, 22–24].

## 1.2 Ruthenates: General aspects

In 1994, Yoshiteru Maeno *et al.* proved with the discovery of SC in  $\text{Sr}_2\text{RuO}_4$  that copper was not a necessary ingredient to produce SC in compounds that are isostructural to  $\text{La}_{2-x}\text{Ba}_x\text{CuO}_4$  [25]. This triggered a wide scientific interest in the ruthenates. A more detailed discussion of  $\text{Sr}_2\text{RuO}_4$  will be given later in this PhD work.

The Ruddlesden-Popper series ruthenates  $(\text{Sr}, \text{Ca})_{n+1}\text{Ru}_n\text{O}_{3n+1}$  (see Fig. 1.2) exhibit a very rich variety of exotic ground states. In these materials, the octahedral crystal field environment lifts the degeneracy of the  $d$ -orbitals. The  $d_{z^2}$ - and  $d_{x^2-y^2}$ -orbitals form the  $e_g$ -states and are higher in energy than the  $t_{2g}$ -manifold that include  $d_{xy}$ - and  $d_{yz}$ -orbitals with  $\gamma = \{x, y\}$  (see Fig. 1.4). Here, four electrons occupy the  $t_{2g}$  subset. Although the bandwidth of the  $4d$ -orbitals are comparable to the Coulomb interaction, these systems turn out to be strongly correlated with large specific heat renormalizations  $\gamma/\gamma_{\text{LDA}} > 4$  and exciting many-body phenomena.

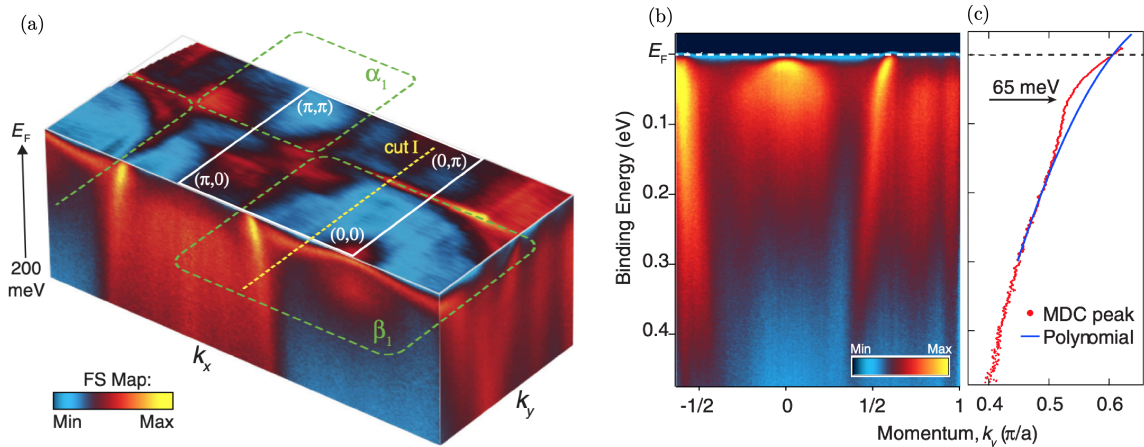


**Fig. 1.4** (a) Fermi surface map of SrRuO<sub>3</sub> at  $T = 20\text{ K}$  integrated within  $E_{\text{F}} \pm 5\text{ meV}$ . (b) ARPES spectrum along cut 1, indicated in (a). (c) Extracted MDC peaks, revealing a kink at 65 meV binding energy. Taken from ref. [34].

### 1.2.1 Infinite-layered compounds

SrRuO<sub>3</sub> ( $n = \infty$ , see Fig. 1.2 (a)) is an itinerant ferromagnet with Curie temperature  $T_C = 160\text{ K}$  [26]. The perovskite crystal structure is orthorhombically distorted at low temperatures and transforms into a tetragonal and finally cubic structure at high temperatures (550°C and 680°C respectively) [27]. Below 15 K (although sensitive to disorder), resistivity of SrRuO<sub>3</sub> exhibits a  $T^2$ -dependence as expected for Fermi liquids (FL) [28]. Above the ferromagnetic transition temperature, resistivity scales nearly linearly up to 1000 K [28, 29]. Surprisingly, optical spectroscopy measurements reveal a deviation from FL behaviour at low temperatures with  $\Re\sigma(\omega) \propto \omega^{-0.5}$  [30, 31]. Furthermore, enhancements of specific heat capacity of factor  $\sim 4$  were observed [29, 32] and an anomalous Hall effect [33]. In an angle-resolved photoemission spectroscopy (ARPES) study, well-defined Landau quasiparticles (QP) have been reported [34]. The QP dispersions display a bosonic kink at low excitation energies that may influence the effective electron masses, contributing to the specific heat. SrRuO<sub>3</sub> is technologically attractive because its properties can be combined by epitaxial growth onto other oxides with matching lattice parameters. This enables functionalization of layered hetero structures, interfaces and junctions. Generally, when substituting Ca for Sr, orthorhombic distortions are either introduced or enhanced due to the smaller ionic radius of Ca [35, 36]. CaRuO<sub>3</sub> is a paramagnet with non-Fermi liquid (nFL)  $T^{1.5}$ -resistivity dependence at low temperatures [28, 37, 38]. An even larger specific heat capacity is reported with a seven times higher value than the prediction in the local

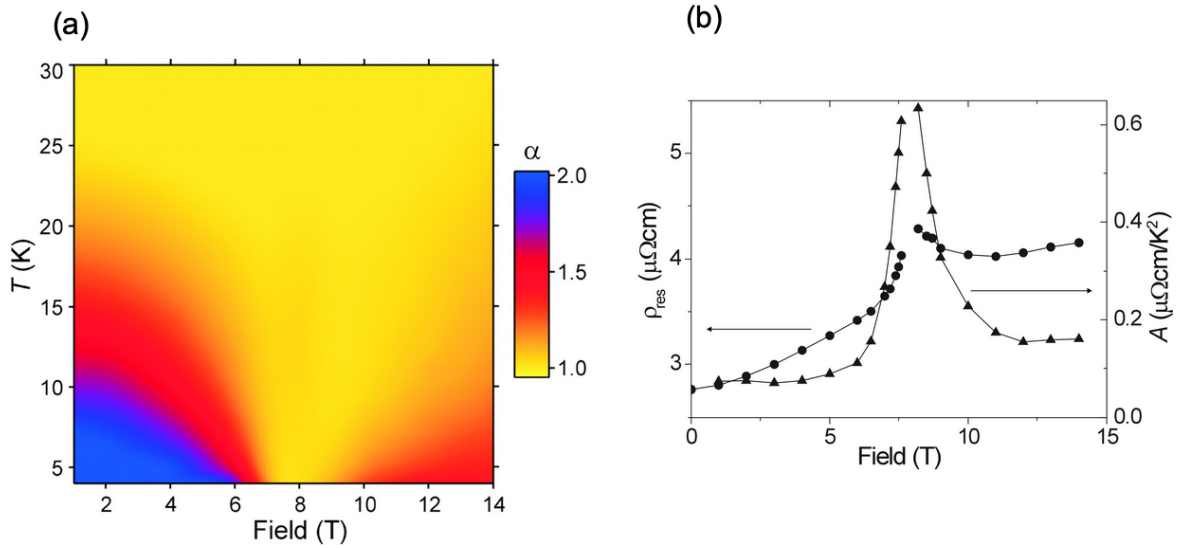


**Fig. 1.5** (a) Magneto-resistivity phase diagram of  $\text{Sr}_3\text{Ru}_2\text{O}_7$ . The intensity map is colour-coded with the magnitude of  $\alpha$  in the resistivity- $T^\alpha$  dependence. At low magnetic fields, the system is a FL. Gradual increase of the external field, suppresses the FL coherence temperature scale and vanishes at the metamagnetic QCP at  $\sim 7.9$  T. (b) Residual resistivity  $\rho_{\text{res}}$  and temperature-scaling factor  $A$  diverge at 7.9 T external magnetic field.

density approximation (LDA) [39] and an additional  $\log T$ -correction to FL part  $\gamma_{\text{FL}}$  [40]. Similar to its sister compound  $\text{SrRuO}_3$ , optical conductivity results yield the peculiar dependency of  $\Re\sigma(\omega) \propto \omega^{-0.5}$  [38]. It has been argued on a theoretical level, that this behaviour originates from Hund's coupling induced frozen local moments, where the spin-spin correlation function does not vanish at long times [20, 41]. However, a comprehensive understanding of bad metal properties in  $\text{SrRuO}_3$  and  $\text{CaRuO}_3$  is still lacking [42].

### 1.2.2 Tri-layered compounds

Less is known about the tri-layered ruthenates ( $n = 3$ , see Fig. 1.2 (b)).  $\text{Sr}_4\text{Ru}_3\text{O}_{10}$  exhibits complex itinerant metamagnetic responses (rapid increase of magnetization  $M$  over a narrow window of external field  $H$ ) and a pressure-induced intralayer antiferromagnetism emerging from interlayer ferromagnetism ( $T_C = 105$  K with easy axis along  $c$ ) [43–47]. Transport experiments on  $\text{Sr}_4\text{Ru}_3\text{O}_{10}$  demonstrate FL behaviour below  $T_{\text{FL}} \simeq 25$  K. With fields close to the metamagnetic transition at  $T_M = 50$  K, the FL coherence temperature scale  $T_{\text{FL}}$  is suppressed [48], attributed to magnetic domain boundary scattering [44, 48]. Specific heat measurements extract a large Wilson-ratio

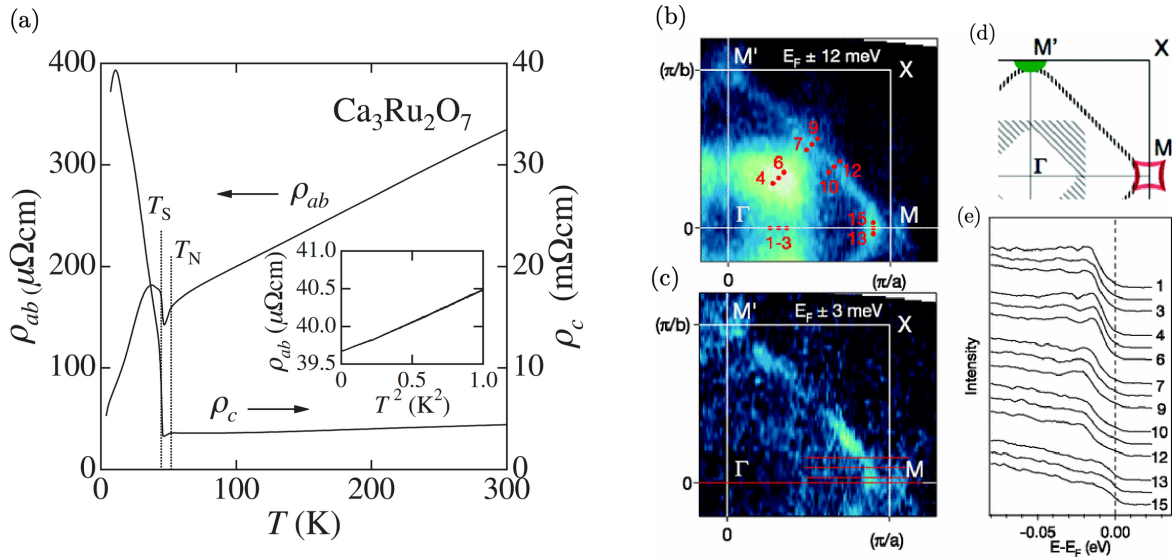


**Fig. 1.6** (a) Resistivity versus Temperature, taken from ref. [52]. The Néel antiferromagnetic ordering occurs at  $T_N = 56$  K and a structural phase transition at  $T_S = 48$  K. In the  $ab$ -plane the resistivity curve inflects at  $T^* = 30$  K. (b, c) are FS maps recorded with ARPES, integrated over an energy range as indicated. (d) Sketch of the FS and pockets drawn in red and green as possibly indicated by the data. (e) EDC's, labeled according to the red dots in (b). Taken from ref. [53].

$R_W \sim 4.5$  (for a free electron gas  $R_W = 1$ ), indicating the importance of electron correlations [49]. At low temperatures (similar to  $\text{CaRuO}_3$ ), a logarithmic (possibly spin-) contribution to the electronic specific heat has been suggested [50]. Partial Sr substitution by Ca distorts the crystal structure and enhances the magnetic anisotropy and electron correlations. Indeed, at low temperatures  $(\text{Sr}_{0.87}\text{Ca}_{0.13})_4\text{Ru}_3\text{O}_{10}$  displays nFL resistivity with a  $T^{3/2}$ -dependence [51].

### 1.2.3 Bi-layered compounds

$\text{Sr}_3\text{Ru}_2\text{O}_7$  is a paramagnet with  $T^2$ -resistivity below 7 K [28] and a large carrier mass enhancement of  $\gamma/\gamma_{\text{LDA}} \sim 10$  [54]. The magneto-resistivity phase diagram of  $\text{Sr}_3\text{Ru}_2\text{O}_7$  contains a quantum critical point (QCP) at  $\sim 7.9$  T when applied along the  $c$ -axis [55, 56]. At these fields, metamagnetism is found, accompanied by a FL-breakdown with linear resistivity  $\alpha = 1$  in  $T^\alpha$  (see Fig. 1.5 (a)). At low temperatures, the residual resistivity  $\rho_{\text{res}}$  (see Fig. 1.5 (b)) and heat capacity become divergent. In general, magnetic instabilities may be favorable by a van-Hove singularity (vHs) near the Fermi level. This has been observed in ARPES studies for the  $d_{xy}$ -orbital driven bands [57, 58]. Furthermore, when the system is field-tuned through the QCP, a strong

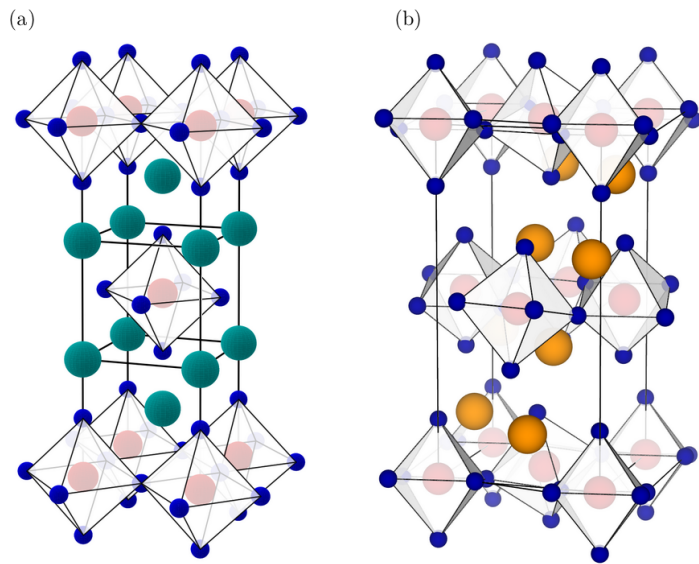


**Fig. 1.7** Illustrative crystal structure of  $\text{Ca}_{2-x}\text{Sr}_x\text{RuO}_4$ . (a) Tetragonal (I4/mmm) unit cell of  $\text{Sr}_2\text{RuO}_4$ . Red, turquoise and blue spheres are Ru-, Sr- and O-atoms, respectively. (b) Orthorhombic (Pbca) unit cell of  $\text{Ca}_2\text{RuO}_4$ . Orange spheres represent Ca atoms.

anisotropy in the magneto-resistivity is found [54, 59]. In a more recent neutron scattering experiment, it was shown that the field-induced electronic nematicity correlates strongly with the emergence of a spin-density-wave [60]. This offers a natural order parameter to associate with the QCP and the electronic nematicity.

Orthorhombic  $\text{Ca}_3\text{Ru}_2\text{O}_7$  is isostructural to  $\text{Sr}_3\text{Ru}_2\text{O}_7$  [61, 62]. At high temperatures,  $\text{Ca}_3\text{Ru}_2\text{O}_7$  is a metallic paramagnet with linear resistivity versus temperature dependence. At  $T_N = 56$  K antiferromagnetic order sets in and below  $T_S = 48$  K  $\text{Ca}_3\text{Ru}_2\text{O}_7$  resistivity rises with lower temperatures until  $T^* = 30$  K, where the opposite trend is observed [61, 63, 64]. At  $T_S$  many properties change. First of all, the sudden resistivity enhancement and emergence of electronic anisotropy coincides with a structural phase transition, where the  $a$  and  $b$  lattice constants enlarge while the  $c$ -axis contracts [62, 65]. The first-order transition also manifests in the heat capacity, as it diverges at  $T_S$  [63, 66]. It has also been shown that the phase transition is accompanied by a CMR effect at  $\sim 6$  T [67, 68] and simultaneous avoidance of ferromagnetic ordering [69]. This is rather peculiar, since CMR is usually driven by ferromagnetism in other materials. Later on this has been explained experimentally and theoretically by the occurrence of an interlayer spin-valve effect in the bulk [70–72]. By further temperature decrease, transport experiments demonstrate an inflection point in the resistivity curves at  $T^* = 30$  K. Metallic behaviour persists down to low temperatures and is reflected in

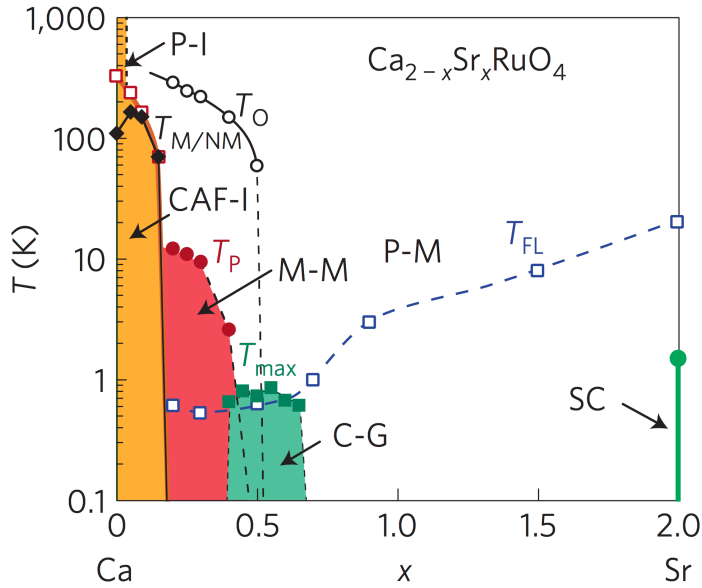


**Fig. 1.8** Phase diagram of  $\text{Ca}_{2-x}\text{Sr}_x\text{RuO}_4$ , taken from ref. [76]. Different ground states are depicted: superconductivity (SC), paramagnetic metal (P-M), paramagnetic insulator (P-I), cluster-glass (C-G), glassy magnetic metal (M-M) and commensurate antiferromagnetic insulator (CAF-I). Below  $T_{\text{FL}}$ , the system is a FL and  $T_{\text{M/NM}}$ ,  $T_P$  and  $T_{\text{max}}$  indicate phase transition temperatures.

the heat capacity [63, 65, 52]. Indeed, an ARPES study finds well-defined Landau QP bands below  $T^*$ . Additional evidence of an electronic instability at  $T_S$  has been found, that gaps out large portions of the Fermi surface (FS) in a Peierls-like fashion (see Fig. 1.6 (b)) [53]. Although (in agreement with quantum oscillation experiments) small pockets are found near the zone corner, the detailed structure of the QP's were not resolved. It is still an outstanding question if the electronic instability is the driving or secondary mechanism for the structural and magnetic phase transition.

### 1.3 Single-layered $\text{Ca}_{2-x}\text{Sr}_x\text{RuO}_4$

Research activity steered also towards exploration of the dense phase diagram of  $\text{Ca}_{2-x}\text{Sr}_x\text{RuO}_4$ , especially on the Mott-insulating Ca-rich region [73–75] (see Fig. 1.8). Scientific contributions, associated to this PhD work, involve the exploration of the electronic structure of  $\text{Ca}_2\text{RuO}_4$  and  $\text{Ca}_{1.8}\text{Sr}_{0.2}\text{RuO}_4$ . In the following, some relevant key aspects of this compound family are outlined.

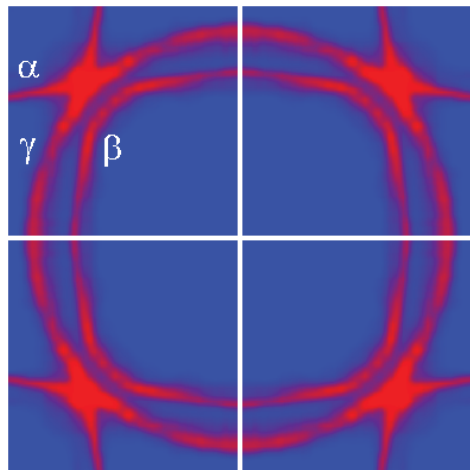


**Fig. 1.9** FS of  $\text{Sr}_2\text{RuO}_4$  measured with ARPES. Three sheets are observed, labeled  $\alpha$  (hole-like),  $\beta$  and  $\gamma$  (both electron-like). Taken from ref. [79].

### 1.3.1 $\text{Sr}_2\text{RuO}_4$ ( $x = 2$ )

$\text{Sr}_2\text{RuO}_4$  crystallizes in the I4/mmm  $\text{K}_2\text{NiF}_4$ -structure with local tetragonal symmetry of the  $\text{Ru}^{4+}$ -ions (see illustratively Fig. 1.7(a)). The lattice constants of  $\text{Sr}_2\text{RuO}_4$  are  $a = b = 3.86 \text{ \AA}$ ,  $c = 12.73 \text{ \AA}$  (at  $T = 20 \text{ K}$ ) with a slightly elongated  $c$ -axis of the  $\text{RuO}_6$ -octahedra [35, 77, 78].  $\text{Sr}_2\text{RuO}_4$  is an unconventional superconductor with  $T_c \simeq 1.7 \text{ K}$  [80]. In general, the superconducting state is a result of quantum-coherent pairing of electrons to Cooper pairs and is characterized by the *order parameter* or gap function  $\Delta(\mathbf{k})$ . In conventional (*s*-wave) SC,  $\Delta(\mathbf{k})$  is isotropic and described by BCS theory [3]. In contrast,  $\Delta(\mathbf{k})$  in unconventional SC (i. e. spin-triplet or *p*-wave SC) often takes on non-trivial forms with

$$\sum_{\mathbf{k}} \Delta(\mathbf{k}) = 0, \quad (1.4)$$

summed over the FS [80] (eq. (1.4) does not hold for *s*-wave SC). This insight and the quantitative congruency with  ${}^3\text{He}$  lead to the suggestion that SC in  $\text{Sr}_2\text{RuO}_4$  is tightly linked to a spin triplet configuration of Cooper-pairs ( $S = 1$ ) [81, 82]. In recent strain experiments,  $T_c$  could be enhanced up to 3.5 K [83, 84], possibly by driving the system through a van Hove singularity (vHs) [85, 86]. Although there exist some thousand publications, in favor or disfavor of the spin-triplet hypothesis, no consensus has been reached yet [80, 87, 88].

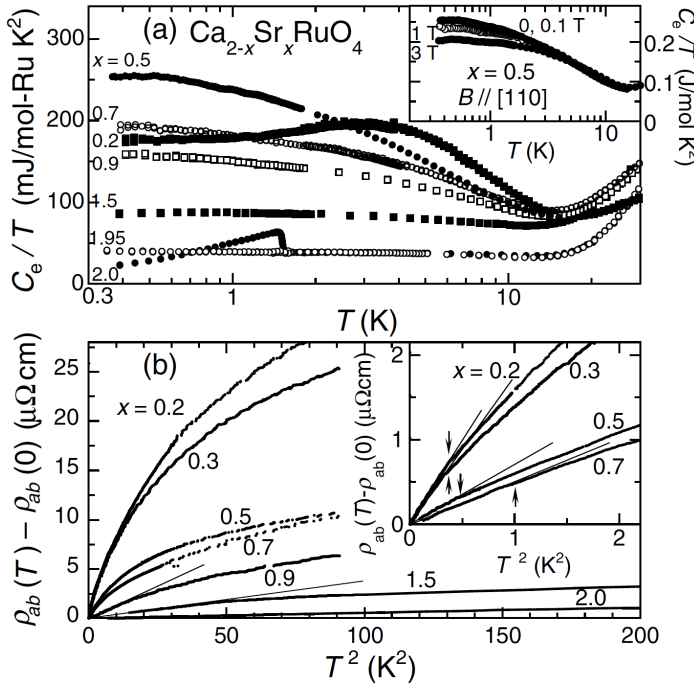


**Fig. 1.10** Properties of  $\text{Ca}_{2-x}\text{Sr}_x\text{RuO}_4$  at low temperatures. (a) Electronic heat capacity  $C_e/T$  versus  $\ln T$  with inset for  $x = 0.5$ . (b) Resistivity curves  $\rho_{ab}(T) - \rho_{ab}(0)$  versus  $T^2$  (the inset is a low-temperature zoom). Arrows in the inset indicate deviation from FL behaviour. Taken from ref. [75].

Below  $T_{\text{FL}} = 30 \text{ K}$ ,  $\text{Sr}_2\text{RuO}_4$  is a Fermi liquid [80]. This has been confirmed by quantum oscillation experiments [89], in agreement with theoretical calculations [90]. In contrast, very recent experiments with Fourier transform scanning tunneling spectroscopy and momentum-resolved electron energy loss spectroscopy question its FL nature by revealing strong correlation effects [91]. De Haas-van Alphen measurements and ARPES results reveal three sheets crossing the Fermi level [89, 92, 79, 93]. The hole-like pocket centered around the zone corner is labeled  $\alpha$ . The electron-like  $\beta$ - and larger  $\gamma$ -band are centered around the  $\Gamma$ -point (see Fig. 1.9). Optical spectroscopy and quantum oscillation experiments have demonstrated that the  $d_{xy}$ -band is (2 – 3 times) heavier and stronger correlated than the  $d_{\gamma z}$ -bands [89, 94, 95]. This introduced the notion and reoccurring theme of orbital-selectivity in the ruthenates.

### 1.3.2 $\text{Ca}_{1.5}\text{Sr}_{0.5}\text{RuO}_4$ ( $x = 0.5$ )

Already slight isovalent substitution of Sr by Ca destroys SC [73, 74]. Starting from  $x = 1.5$ , the smaller size of the Ca-atoms introduces azimuthal rotations of the oc-

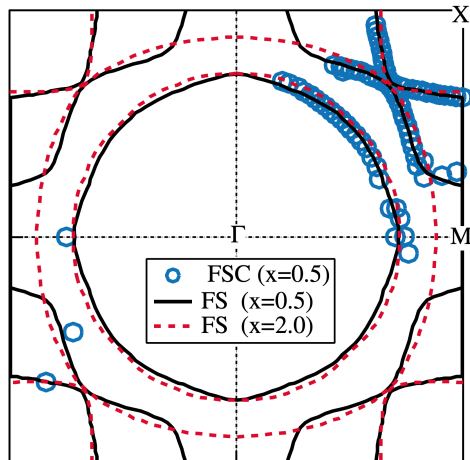


**Fig. 1.11** Extracted crossings of the FS of  $\text{Ca}_{1.5}\text{Sr}_{0.5}\text{RuO}_4$  indicated as blue circles. Black is a modeling fit and the dashed red line represents the  $\text{Sr}_2\text{RuO}_4$  FS. Taken from ref. [100].

tahedra that increase with diminishing  $x$  up to  $13^\circ$  at  $x = 0.5$ . In that substitution region, an enhanced Curie-Weiss type ferromagnetic susceptibility is observed with  $S = 1/2$  [73] (instead of expected  $S = 1$ ). A peculiarity of this system are the coexisting transport of itinerant electrons and an unusually high Sommerfeld constant of  $\gamma = 250 \text{ mJ/mol K}^2$  ( $\sim 20$  times the LDA value) [75], see Fig. 1.10 (a). The coexistence of metallicity and a  $S = 1/2$ -moment lead to the interpretation of an orbital-selective Mott phase (OSMP) [35]. In this scenario three electrons localize in the  $d_{\gamma z}$ -channel while the other electrons with  $d_{xy}$ -character cross the Fermi level. This possible explanation ignited a controversy surrounding the OSMT [35, 96–99]. It is believed, that the OSMT is triggered by a large enough  $J_H$  to suppress orbital fluctuations. In this fashion the orbitals are decoupled and may localize separately for different critical Coulomb interactions  $U_c$  [20, 22–24].

ARPES studies on  $\text{Ca}_{1.5}\text{Sr}_{0.5}\text{RuO}_4$  revealed the existence of three FS sheets, corresponding to the  $\alpha$ -,  $\beta$ - and  $\gamma$ -bands in the parent compound [100, 101]. These experiments demonstrated the absence of orbital-selective Mott physics in  $\text{Ca}_{1.5}\text{Sr}_{0.5}\text{RuO}_4$ . However, the  $\gamma$ -band has been found to be hole-like, instead of electron-like as in  $\text{Sr}_2\text{RuO}_4$  (see Fig. 1.11).

### 1.3.3 $\text{Ca}_{1.8}\text{Sr}_{0.2}\text{RuO}_4$ ( $x = 0.2$ )

Between  $0.2 < x < 0.5$ , additional tilting of the octahedra sets in [102], which further narrows the  $d_{xy}$ -bandwidth.  $\text{Ca}_{1.8}\text{Sr}_{0.2}\text{RuO}_4$  is the critical composition of

the metal-Mott-insulator transition in the  $\text{Ca}_{2-x}\text{Sr}_x\text{RuO}_4$ -phase diagram. Resistivity measurements reveal a very low coherence temperature ( $T_{\text{FL}} < 1 \text{ K}$ ) below which  $\text{Ca}_{1.8}\text{Sr}_{0.2}\text{RuO}_4$  is a FL (see Fig. 1.10 (b)) [75].

So far, there exist two ARPES studies with contradicting conclusions. In one experiment, the authors do not observe the  $d_{xy}$ -band, attributing this absence to orbital-selective Mott localization [97]. In another study, however, all three FS sheets were found, disfavoring the OSMT scenario [98]. Details of the experimental controversy will be given later. This direct contradiction is yet unresolved and calls for an experimental resolution which will be presented in this PhD work.

### 1.3.4 $\text{Ca}_2\text{RuO}_4$ ( $x = 0$ )

In  $\text{Ca}_2\text{RuO}_4$ , the other end member of the series, distortions of the crystal lattice are the strongest (see Fig. 1.7 (b)). It crystallizes in two orthorhombic Pbca-structures. In the high-temperature L-Pbca phase the  $\text{RuO}_6$ -octahedra are elongated ( $a = 5.36 \text{ \AA}$ ,  $b = 5.35 \text{ \AA}$  and  $c = 12.26 \text{ \AA}$  at  $T = 400 \text{ K}$ ), while they are compressed below  $T_S = 356 \text{ K}$  in the S-Pbca phase ( $a = 5.39 \text{ \AA}$ ,  $b = 5.60 \text{ \AA}$  and  $c = 11.77 \text{ \AA}$ ) [103].  $\text{Ca}_2\text{RuO}_4$  has fascinating properties. Firstly, it is a structurally driven Mott insulator and orders antiferromagnetically below  $T_N = 110 \text{ K}$  [104]. Experiments indicate the appearance of SC by flattening the  $\text{RuO}_6$  octahedra when high pressure is applied [105] or when  $\text{Ca}_2\text{RuO}_4$  is grown as nanofilm single crystals (with a bias current) [106]. Dilute Cr doping for Ru induces a negative volume thermal expansion, that holds potential for technical applications [107]. Recently, it has been demonstrated how a bias current turns  $\text{Ca}_2\text{RuO}_4$  into a semimetal and exhibits a record-high diamagnetic response [108]. It is also worth mentioning, that a collective amplitude mode in  $\text{Ca}_2\text{RuO}_4$ , observed in recent neutron and Raman scattering experiments, resembles aspects of the Higgs mode known in particle physics [109, 110].

With four electrons in the  $t_{2g}$ -manifold per Ru site, it is not straight forward to reconcile how the Mott-insulating state of  $\text{Ca}_2\text{RuO}_4$  is realized. Two scenarios have been proposed. One situation encompasses an extension of the OSMT-idea, where orbital-selective Mott gaps are imposed on different  $t_{2g}$ -subbands [111]. In the other scenario, the  $c$ -axis is stabilized such that the  $d_{xy}$ -states are band-insulating and the half-filled  $d_{\gamma z}$ -bands are Mott-insulating [96, 99]. No consensus has yet been reached experimentally. In this PhD work, ARPES results combined in conjunction with band structure calculations are presented that explain the low-energy electronic structure.

## 1.4 Outline of the thesis

Structurally, this PhD work starts with a theoretical block addressing important concepts, relevant to the physics of the ruthenates. In the next chapter, the fundamentals of ARPES are laid out, from ab-initio theory to data transformations and analysis. Chapter 4 & 5 contain the main results and expand on two first-authored publications in a detailed fashion. Lastly, I summarize the conclusions and give an outlook for future experiments. I aim that this thesis provides a coherent introduction to the ruthenates and supports future PhD-students who are interested in the ARPES-methodology, applied to strongly correlated systems.



# Chapter 2

## Concepts in condensed matter physics

### 2.1 Many-body physics

In order to describe elementary excitations in molecules and solids, many-body perturbation theory has been proven as a useful tool in solid state physics [112, 113]. The main idea is to consider the response of an electronic system as a whole, upon removal/addition of an electron from/to a single particle state. The response is given in terms of the complex and energy dependent *self-energy*  $\Sigma(\mathbf{k}, \omega)$ , which describes screening effects and finite lifetime of QP excitations  $\tau_{\mathbf{k}} \simeq \frac{\hbar}{2\Im\Sigma(\mathbf{k}, \omega)}$ . In many-body perturbation theory, a more general set of equations have to be solved [114]:

$$\left( -\frac{\hbar^2}{2m} \nabla^2 + V(\mathbf{x}) \right) f_s(\mathbf{x}) + \int \Sigma(\mathbf{x}, \mathbf{x}', \omega) f_s(\mathbf{x}') d\mathbf{x}' = \varepsilon_s f_s(\mathbf{x}) \quad (2.1)$$

where  $\mathbf{x} = (\mathbf{r}, \sigma)$  are space and spin coordinates. The excited state with quantum number  $s$ , is described by the QP amplitude  $f_s(\mathbf{x})$ . A natural way to find practical approximations to the self energy are one-electron addition (+) and removal (-) Green's functions for interacting electrons  $\mathcal{G}^{\pm}(\mathbf{k}, \omega)$ . They describe the time evolution of an extra added electron / hole due to ionization of the system.

#### 2.1.1 Green's function

To briefly introduce the concept of the Green's function, let's start with the time-dependent Schrödinger equation for a single electron in an external potential  $V(\mathbf{x}, t)$

and free particle Hamiltonian  $\mathcal{H}_0 = -\frac{\hbar^2}{2m}\nabla^2$ :

$$\left(\frac{\hbar}{i}\frac{\partial}{\partial t} + \mathcal{H}_0(\mathbf{x})\right)\psi(\mathbf{x}, t) = -V(\mathbf{x}, t)\psi(\mathbf{x}, t) \quad (2.2)$$

The Green's function  $\mathcal{G}_0(\mathbf{x}, \mathbf{x}', t)$  satisfies the equation

$$\left(\frac{\hbar}{i}\frac{\partial}{\partial t} + \mathcal{H}_0(\mathbf{x})\right)\mathcal{G}_0(\mathbf{x}, \mathbf{x}', t) = -\delta(\mathbf{x} - \mathbf{x}')\delta(t). \quad (2.3)$$

$\mathcal{G}_0(\mathbf{x}, \mathbf{x}', t)$  is the Fourier transform of  $\mathcal{G}_0(\mathbf{x}, \mathbf{x}', \omega)$  with

$$\mathcal{G}_0(\mathbf{x}, \mathbf{x}', t) = \frac{1}{2\pi} \int_{-\infty}^{+\infty} \mathcal{G}_0(\mathbf{x}, \mathbf{x}', \omega) e^{-i\omega t} d\omega \quad (2.4)$$

It can be shown that  $\mathcal{G}_0(\mathbf{x}, \mathbf{x}', \omega)$  is the real space representation of the projection operator with eigenfunctions  $\{\phi_i(\mathbf{x})\}$  of  $\mathcal{H}_0(\mathbf{x})$  and associated eigenvalues  $\{\varepsilon_i^0\}$ :

$$\mathcal{G}_0^+(\mathbf{x}, \mathbf{x}', \omega) = \sum_i \frac{\langle \mathbf{x} | \phi_i \rangle \langle \phi_i | \mathbf{x}' \rangle}{\omega - \varepsilon_i^0 + i\eta}, \quad \eta > 0 \quad (2.5)$$

where a positive infinitesimal  $\eta$  is introduced to handle the poles on the real axis. From eq. (2.5) it is clear that eigenstates of the system correspond to the poles of the Green's function. The Fourier transform eq. (2.4) can now be computed as a contour integral in the lower half complex plane<sup>1</sup>. Eq. (2.2) can now be formally solved:

$$\psi(\mathbf{x}, t) = \phi(\mathbf{x}, t) + \int \mathcal{G}_0^+(\mathbf{x}, \mathbf{x}', t - t') V(\mathbf{x}', t') \psi(\mathbf{x}', t') d\mathbf{x}' dt' \quad (2.6)$$

The concept of Green's functions can be expanded to systems of interacting electrons. Similar to eq. (2.5), it is found:

$$\mathcal{G}^\pm(\mathbf{k}, \omega) = \sum_m \frac{|\langle \Psi_m^{N\pm 1} | \hat{c}_{\mathbf{k}}^\pm | \Psi_i^N \rangle|^2}{\omega \mp (E_m^{N\pm 1} - E_i^N) \pm i\eta} \quad (2.7)$$

But now, the amplitudes are matrix elements of electron creation  $\hat{c}_{\mathbf{k}}^+$  and annihilation  $\hat{c}_{\mathbf{k}}^-$  between many-body states. The one-electron addition and removal spectra  $\mathcal{A}^\pm(\mathbf{k}, \omega)$  describe the single particle excitation spectrum

$$\mathcal{A}^\pm(\mathbf{k}, \omega) = \sum_m |\langle \Psi_m^{N\pm 1} | \hat{c}_{\mathbf{k}}^\pm | \Psi_i^N \rangle|^2 \delta(\omega - E_m^{N\pm 1} + E_i^N) \quad (2.8)$$

Using the representation of the delta distribution

---

<sup>1</sup>For negative times, the contour has to be closed in the upper half plane to converge. Since it contains no poles, the result is  $\mathcal{G}_0(\mathbf{x}, \mathbf{x}', t) = 0$ .

$$\delta(x - x_0) = \lim_{\eta \rightarrow 0^+} \frac{\mp 1}{\pi} \Im \frac{1}{x - x_0 \pm i\eta}, \quad (2.9)$$

the one-electron spectral function  $\mathcal{A}(\mathbf{k}, \omega) = \mathcal{A}^+(\mathbf{k}, \omega) + \mathcal{A}^-(\mathbf{k}, \omega)$  reads:

$$\mathcal{A}(\mathbf{k}, \omega) = -\frac{1}{\pi} \Im \mathcal{G}(\mathbf{k}, \omega) \quad (2.10)$$

with  $\mathcal{G}(\mathbf{k}, \omega) = \mathcal{G}^+(\mathbf{k}, \omega) + (\mathcal{G}^-(\mathbf{k}, \omega))^*$ . By virtue of eq. (2.1), the Green's function satisfies:

$$\left( -\frac{\hbar^2}{2m} \nabla^2 + V(\mathbf{x}) - \omega \right) \mathcal{G}(\mathbf{x}, \mathbf{x}', \omega) + \int \Sigma(\mathbf{x}, \mathbf{x}'', \omega) \mathcal{G}(\mathbf{x}'', \mathbf{x}', \omega) d\mathbf{x}'' = -\delta(\mathbf{x} - \mathbf{x}') \quad (2.11)$$

In operator form:

$$(\mathcal{H}_0 + V - \omega) \mathcal{G}(\omega) + \Sigma(\omega) \mathcal{G}(\omega) = -\mathbf{1} \quad (2.12)$$

Taking diagonal matrix elements in the basis of Bloch functions with band index  $n$ , wave vector  $\mathbf{k}$  and using eq. (2.10) we end up with

$$\mathcal{G}(\mathbf{k}, \omega) = \frac{1}{\omega - \varepsilon_{\mathbf{k}}^b - \Sigma(\mathbf{k}, \omega)}, \quad (2.13)$$

$$\mathcal{A}(\mathbf{k}, \omega) = -\frac{1}{\pi} \frac{\Im \Sigma(\mathbf{k}, \omega)}{\left[ \omega - \varepsilon_{\mathbf{k}}^b - \Re \Sigma(\mathbf{k}, \omega) \right]^2 + [\Im \Sigma(\mathbf{k}, \omega)]^2} \quad (2.14)$$

where  $\varepsilon_{\mathbf{k}}^b$  is the bare band dispersion.

### 2.1.2 Quasiparticle residue

Note that the self-energy has to be evaluated at the true excitation energy  $\omega$ , which is given by the implicit equation

$$\omega = \varepsilon_{\mathbf{k}}^b + \Sigma(\mathbf{k}, \omega) = \frac{k^2 - k_F^2}{2m_b} + \Sigma(\mathbf{k}, \omega), \quad (2.15)$$

with the bare band mass  $m_b$ , extracted as a fit parameter of a simple tight binding model or a local parabolic dispersion, that is fitted to a DFT band structure calculation near the Fermi level [115, 116]. It is usually assumed that the self-energy varies slowly, so expanding around  $(k = k_F, \omega = 0)$  leads to:

$$\omega = \frac{k^2 - k_F^2}{2m_b} + \left( \frac{\partial \Sigma}{\partial k} \right)_{k=k_F} (k - k_F) + \left( \frac{\partial \Sigma}{\partial \omega} \right)_{\omega=0} \omega. \quad (2.16)$$

In the effective mass approximation, the ansatz  $\omega = (k^2 - k_F^2)/2m^*$  is used:

$$\frac{m_b}{m^*} = \frac{1 + (m/k_F)(\partial \Sigma / \partial k)_{k=k_F}}{1 - (\partial \Sigma / \partial \omega)_{\omega=0}}. \quad (2.17)$$

If the self-energy varies slow enough with  $k$ , we neglect  $\partial \Sigma / \partial k$  and introduce the quasiparticle residue  $Z$  as a measure of correlation strength:

$$Z \equiv \left( 1 - \left. \frac{\partial \Sigma}{\partial \omega} \right|_{\omega=0} \right)^{-1}. \quad (2.18)$$

$Z$  yields the spectral weight of the excitation which is equal to one for non-interacting systems and smaller than one in the presence of electron interactions. By linearization of the band dispersion close to the Fermi level  $\varepsilon_{\mathbf{k}}^b \simeq v_F^b(k - k_F)$  with bare band velocity  $v_F^b$ ,  $Z = m_b/m^* = v_F/v_F^b$ .

In the FL description, one can split the spectral function into a coherent pole part  $\mathcal{A}_{\text{coh}}(\mathbf{k}, \omega)$  and an incoherent part without poles  $\mathcal{A}_{\text{inc}}(\mathbf{k}, \omega)$ . The spectral function, observed in photoemission  $\varepsilon_{\mathbf{k}}^b < E_F$  is then

$$\mathcal{A}(\mathbf{k}, \omega) \simeq -\frac{Z}{\pi} \frac{\Gamma}{(\omega - \varepsilon_{\mathbf{k}}^q)^2 + \Gamma^2} + \mathcal{A}_{\text{inc}}, \quad (2.19)$$

with quasiparticle excitation energy  $\varepsilon_{\mathbf{k}}^q = Z(\varepsilon_{\mathbf{k}}^b + \Re \Sigma(\omega = 0))$  and inverse quasiparticle life-time  $\Gamma = Z|\Im \Sigma(\omega = 0)|$ .

Since the spectral function describes the probability of removing or adding an electron with momentum  $\mathbf{k}$  and energy  $\omega$ , the following sum rule has to hold:

$$\int_{-\infty}^{\infty} d\omega \mathcal{A}(\mathbf{k}, \omega) = 1 \quad (2.20)$$

and therefore  $\int_{-\infty}^{\infty} d\omega \mathcal{A}_{\text{coh}}(\mathbf{k}, \omega) = Z$  and  $\int_{-\infty}^{\infty} d\omega \mathcal{A}_{\text{inc}}(\mathbf{k}, \omega) = 1 - Z$ . The spectral function is the meeting point of many-body physics and the ARPES experiment.

## 2.2 Fermi liquid quasiparticles

Next, we discuss QP excitations through the lens of FL theory. A thorough discussion of this very deep theory goes beyond the scope of this introduction. In the following,

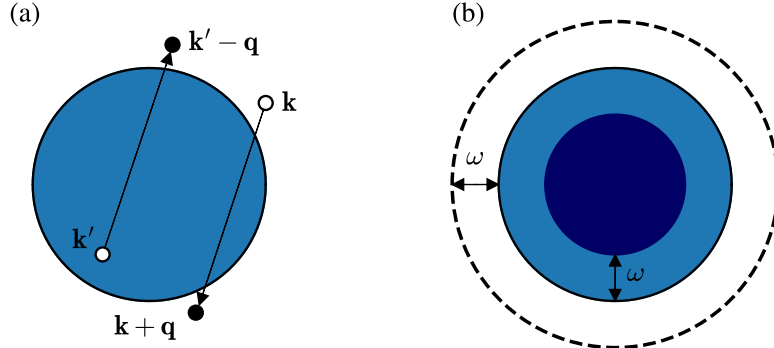


**Fig. 2.1** (a) Schematics of the decay of an electron with momentum  $\mathbf{k}$  in the presence of a filled Fermi sea. As the momentum of the electron changes to  $\mathbf{k} + \mathbf{q}$ , a particle-hole pair appears with momenta  $\mathbf{k}'$  and  $\mathbf{k}' + \mathbf{q}$ , respectively. (b) Phase space available for scattering events of the initial (inner dark shaded circle) and final state (dashed line). Both scale with energy, hence a inverse QP life-time proportional to the excitation energy  $\omega$ , relative to the Fermi level.

some important key aspects, relevant to this work are laid out. Originally, the concept of a FL has been developed by Landau in order to describe the properties of liquid  $^3\text{He}$  with fermionic character, hence the name of that theory. Landau received the Nobel prize in physics in 1962 for his theory of superfluidity in helium II below 2.17 K [117]. The basic assumption is that there exists a one-to-one correspondence between a free electron gas of independent Fermions and the interacting system by turning on the interactions adiabatically.

Considering a filled Fermi sea and an electron with momentum  $\mathbf{k}$ , the dominant decay process of the electron involves the creation of a particle-hole pair. As the electron scatters into  $\mathbf{k} + \mathbf{q}$ , a hole in the Fermi sea appears at  $\mathbf{k}'$  with a second electron outside the Fermi sea at  $\mathbf{k}' - \mathbf{q}$  (see Fig. 2.1 (a)), obeying momentum and energy conservation. The transition rate of the initial state into the many-body state is calculated via Fermi's golden rule. For small QP excitation energies  $\omega$  near the Fermi level  $E_F$ , the transition rate  $\tau_{\mathbf{k}}^{-1}$  is approximated by

$$\frac{1}{\tau_{\mathbf{k}}} = \frac{1}{8\pi\hbar^3} \frac{N(E_F)}{v_F^2} (\varepsilon_{\mathbf{k}} - E_F)^2 \int dq |V(q)|^2, \quad (2.21)$$

where  $v_F$  is the Fermi velocity,  $N(E_F)$  is the density of states (DOS) at the Fermi level and  $V(q)$  is the Fourier transform of the (short-ranged) scattering potential. The essential result is that

$$\frac{1}{\tau_{\mathbf{k}}} \propto (\varepsilon_{\mathbf{k}} - E_F)^2, \quad (2.22)$$

the phase space available for scattering events scales with energy squared, relative to the Fermi level (Fig. 2.1(b)). The spectral function of the state features a QP resonance peak of width  $\hbar/\tau_{\mathbf{k}}$ , which becomes infinitely sharp at the Fermi surface

$$\lim_{k \rightarrow k_F} \frac{\hbar/\tau_{\mathbf{k}}}{\varepsilon_{\mathbf{k}} - E_F} = 0. \quad (2.23)$$

Referring back to the form of the spectral function in eq. (2.19), we observe that the inverse QP life-time (or width) is proportional to the imaginary part of the self-energy. Our considerations imply that  $\Im\Sigma(\omega \rightarrow 0) = 0$  and  $\Im\Sigma(\omega) \propto \omega^2$ . The real part of the self-energy is obtained via a Kramers-Kronig transformation, for which one assumes a cut-off energy for the high- and low-energy region. This is known as the *tail-problem* [118]. Up to higher order terms,  $\Re\Sigma(\omega)$  is proportional to  $\omega$ , yielding

$$\Sigma = \gamma_0\omega + i\alpha_0[\omega^2 + (\pi k_B T)^2], \quad (2.24)$$

where  $\gamma_0$  and  $\alpha_0$  are constants [119, 120]. In order to have a coherent QP – similar to the resonance phenomenon of a damped harmonic oscillator – its excitation energy has to be larger than the inverse QP life-time [121]

$$\omega > -Z\Im\Sigma(\omega). \quad (2.25)$$

Together with the definition of  $Z$  (2.18) and the FL self-energy (2.24) we obtain a criterion for a coherent FL QP:

$$\frac{\Re\Sigma(\omega)}{1 - Z} > \Im\Sigma(\omega), \quad 0 < Z < 1. \quad (2.26)$$

An important class of Fermi liquids are *heavy Fermion*-systems. These are (cerium- or uranium-based) materials, that are characterized by effective electron masses and Sommerfeld constants  $\mathcal{O}(3)$  larger as expected from free-electron theory [122, 123]. A universal value has been found, that characterizes heavy Fermions. This value, known as the Kadowaki-Woods ratio (KWR) [124, 125], is observed as  $A/\gamma^2 \simeq 1.0 \times 10^{-5} \mu\Omega\text{cm}$ ,

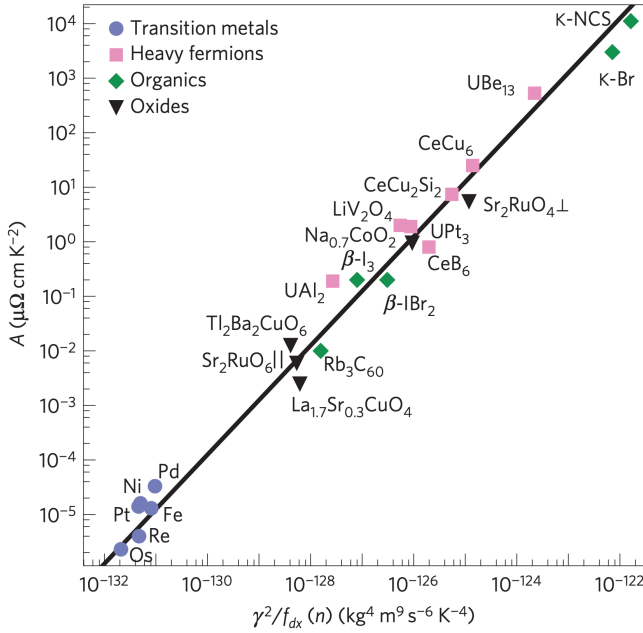


**Fig. 2.2** Modified KWR for transition metals, heavy fermions, organics and oxide materials. Taken from ref. [126].

where  $A$  and  $\gamma$  are coefficients from the resistivity  $\rho(T)$  and heat capacity  $c_{\text{el}}(T)$ , predicted from FL-theory:

$$\rho(T) = \rho_{\text{res}} + AT^2, \quad c_{\text{el}} = \gamma T. \quad (2.27)$$

It has been shown later, that the KWR can be expanded to other strongly correlated systems by taking into account some system-dependent effects like carrier density and dimensionality [126, 127].

## 2.3 Non-Fermi liquids

Generally, non-Fermi liquid (nFL) systems exhibit thermodynamic and transport properties at low temperatures that are fundamentally different from those of usual metals, described by FL-theory. Commonly, it is assumed that the FL self-energy is local, i. e. only dependent on  $\omega$  and not on  $k$  [112].  $\text{La}_{1.77}\text{Sr}_{0.23}\text{CuO}_4$  is an example where  $\Sigma(\mathbf{k}, \omega)$  is highly anisotropic [128]. From the momentum-dependent breakdown of FL QPs suggests that the KWR ratio is not obeyed.

On a theoretical level, a *Luttinger liquid* demonstrates a breakdown of FL-theory in one dimension [129, 130]. Experimental demonstration of Luttinger liquids, e. g. carbon

nanotubes [131], are still object of ongoing experimental research.

A rather prominent example of nFL-behaviour is the *strange metal*-phase in cuprate high  $T_c$  superconductors [132–134]. The strange metal phase is characterized by the absence of QPs that manifests physically in a linear temperature dependence of the electrical resistivity. The microscopic explanation is still controversial. The *marginal FL* is an attempt to describe a vanishing  $Z$  [119], requiring the self-energy to be singular at  $k_F$  (see eq. (2.18)),

$$\Sigma(k_F, \omega) \simeq \lambda \left[ \omega \ln \frac{\omega_c}{\omega} + i|\omega| \right], \quad (2.28)$$

with coupling constant  $\lambda$  and characteristic energy cutoff  $\omega_c$ .

## 2.4 Mott physics

Band theory is based on a one-electron picture in the Hartree-Fock approximation. There, the distinction between metals and insulators is clear. For insulators the atomic electrons fill up exactly an integer number of bands while all other bands are empty. Occupied and unoccupied bands are separated by an energy gap. Metals exhibit partially filled bands and we can describe low energy excitations as QPs in Landau's Fermi liquid theory [135]. Insulators have an even number, while metals have an odd number of electrons per unit cell. However, some transition metal oxides like NiO with an odd number of electrons per unit cell are insulating [136]. In a half-filled valence band, each atomic site is singly occupied. Charge conductance would require at least one electron to hop to a neighboring site, creating an empty orbital and a doubly occupied one. Coulomb repulsion of two electrons occupying the same site might be so strong, that such hopping transitions are energetically too expensive, resulting in localization. This was pointed out early on by Nevill Mott and Rudolf Peierls [137]. Such a system becomes a *Mott-insulator*. With shrinking lattice constant  $a$  (or increasing orbital radial extensions relative to  $a$ ), orbital overlap increases and a metallic state emerges. This transformation is known as a Mott-Hubbard-transition. The most simple model for  $d$ -electrons in transition metals and their compounds is the single-band Hubbard model. The Hamiltonian reads

$$\mathcal{H} = \mathcal{H}_{\text{Band}} + \mathcal{H}_{\text{Coulomb}} = -t \sum_{ij,\sigma} \hat{c}_{i\sigma}^+ \hat{c}_{j\sigma}^- + U \sum_i \hat{n}_{i\uparrow} \hat{n}_{i\downarrow} \quad (2.29)$$

describing nearest neighbor hopping only, via matrix element  $-t$ , related to the bandwidth  $W = 2D = 12t$  (in three dimensions), where  $D$  is the half-bandwidth.  $\hat{c}_{i\sigma}^\pm$

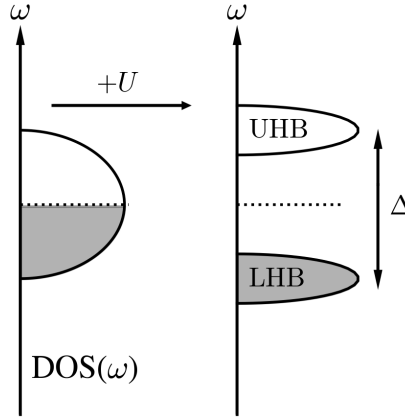


**Fig. 2.3** Schematic representation of the DOS of the MIT in the Hubbard-model. Starting from metallic half filled band, a strong Coulomb repulsion  $U$  splits the band into two Hubbard sub-bands, seperated by a Mott gap  $\Delta$ .

are real-space field operators on the lattice site  $i$  with spin  $\sigma$ ,  $\hat{n}_{i\sigma} = \hat{c}_{i\sigma}^+ \hat{c}_{i\sigma}^-$  is the density operator and  $U$  is the matrix element of the Coulomb potential. We focus here on one electron per atomic site (half filling). In the metallic band limit  $U = 0$ , the band energy is given by a simple Fourier transform:

$$\mathcal{H}_{\text{Band}} = \sum_{\mathbf{k}} \sum_{\sigma} \varepsilon_{\mathbf{k}} \hat{c}_{\mathbf{k},\sigma}^+ \hat{c}_{\mathbf{k},\sigma}^- \quad (2.30)$$

with the dispersion relation:

$$\varepsilon_{\mathbf{k}} = -t \sum_{\mathbf{a}} e^{i\mathbf{k}\cdot\mathbf{a}}, \quad (2.31)$$

where the sum runs over all lattice vectors  $\mathbf{a}$ , connecting nearest neighbors with unique ground state

$$|\Psi_{U=0}\rangle = \prod_{\mathbf{k}} \Theta(-\varepsilon_{\mathbf{k}}) \hat{c}_{\mathbf{k},\uparrow}^+ \hat{c}_{\mathbf{k},\downarrow}^+ |0\rangle \quad (2.32)$$

In the atomic limit  $t = 0$  and  $U > 0$ , the ground state has exactly one electron per site of the form

$$|\Psi\{\sigma_i\}\rangle = \prod_i \hat{c}_{i\sigma_i}^+ |0\rangle. \quad (2.33)$$

with a high ground state degeneracy of  $2^N$  due to the spin degree of freedom. The first excited state has one empty and one doubly occupied site with energy  $U$ , thus the system is an insulator. Suppose we have  $N + 1$  electrons where  $N$  electrons are

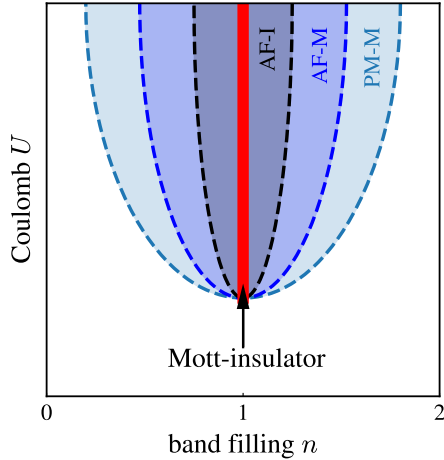


**Fig. 2.4** Generic phase diagram of the Mott-insulator transition via filling control versus Coulomb  $U$ . The Mott state is stabilized for a half-filled band. For other dopings, the system tends to drive away from the Mott-insulating ground state into an insulating or metallic antiferromagnet (AF-I, AF-M) or paramagnetic metal (PM-M) [17, 138, 139].

localized on their sites. The motion of the extra electron, freely hopping between sites, can be described via an electronic band of width  $D$ . By the same token, a hole for  $N - 1$  electrons can move freely. Therefore, by starting from the metallic limit and increasing  $U$  up to a critical value  $U_c \approx 25t \sim 4D$ , the DOS splits into an *upper Hubbard band* (UHB) and a *lower Hubbard band* (LHB). Both have a width of  $D$ , separated by a Mott gap  $\Delta = U$  (Fig. 2.3). Despite its simplicity, the single-band Hubbard model is able to describe a variety of phenomena such as itinerant ferromagnetism, MIT and some important aspects of HTSC in layered cuprates [17].

Starting from the single-layered Mott-insulator  $\text{La}_2\text{CuO}_4$ , SC emerges upon hole or electron doping [19]. This created much attention towards a more elaborate two-dimensional Hubbard model. As a consequence, filling-controlled MITs have been studied vividly and are still object of ongoing research [17, 138, 139]. Generally, the Mott insulating state is stabilized at half-filling and becomes metallic with charge carrier doping. Experimentally, however, it has been shown that the critical doping to destroy the Mott state can deviate from half-filling, i. e., in nickelates [140] or vanadates [141]. A generic phase diagram is shown in Fig. 2.4 [139].

## 2.5 Hund's coupling

Based on empirical data, Friedrich Hund, Henri Norris Russell, Frederick Albert Saunders formulated in 1925 a set of rules to determine the ground state of electron configurations [142]. Provided sufficient degeneracy, such that non-equivalent wave functions can be constructed. The three *Hund's rules* are:

1. The lowest energy state corresponds to a state with maximum spin number  $S$ .
2. Given  $S$ , the total angular momentum  $L$  has to be maximized.
3.  $J = L + S$  minimizes the energy if the shell is more than half-filled and  $J = |L - S|$  if the shell is less than half-filled.

The Pauli principle states that the total wavefunction (combined orbital and spin part) must be antisymmetric with respect to particle exchange. From this follows that if orbital degeneracy is provided, the triplet configuration is energetically favored. If degeneracy is absent, the singlet state is lower in energy because of the Pauli principle. Intuitively, when two electrons are configured in a symmetric triplet state, the antisymmetric orbital wave function ensures that the electrons are placed far away from each other on average (with respect to a symmetric wave function) and thus lowers the energy. Hund's coupling  $J_H$ , associated to intra-atomic exchange, therefore fundamentally shapes the ground state spin configurations in multi-orbital systems. In general, strongly correlated electron systems such as ruthenates, iron pnictides and chalcogenides are multi-band materials that display strong correlations while not necessarily being close to a Mott insulating state [23, 143–149]. In the past decade, it became more evident that  $J_H$  represents an additional channel for strong electron correlations [20, 23, 143].

Fig. 2.5 shows a colormap of the QP weight  $Z$  for different  $t_{2g}$  fillings plotted versus  $U$ , normalized by  $D$  for a fixed  $J_H = 0.15 U$  [23]. Thick black bars indicate the predicted Mott insulating state. From this model calculation it becomes apparent that the Mott state is stabilized for  $n = 3$  and breaks down when deviating from half-filling. Remarkably, for  $n = 2, 4$ ,  $Z$  is close to zero even though the system is not in proximity to a Mott insulating ground state. In this regime, strong correlations are manifested in a poor ability to screen local moments, electrical resistivity far above the Mott-Ioffe limit or a low coherence temperature scale  $T_{FL}$ , above which FL theory breaks down. The simultaneous increase of the Mott-critical  $U_c$  and bad metal behaviour are characteristic features of *Hund's metals* [20].

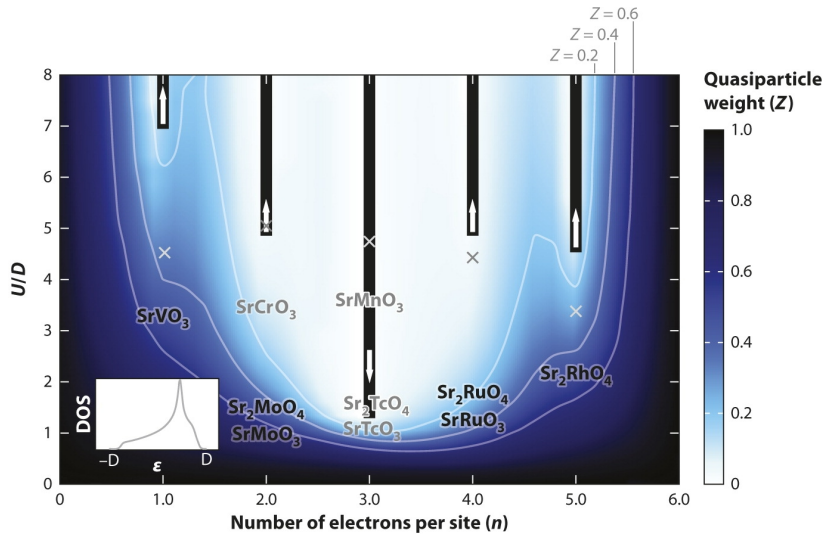


**Fig. 2.5** Intensity map of QP weight  $Z$  of a three-orbital model, plotted for different band fillings versus interaction strength  $U$  normalized by the half-width  $D$ . The Hund's coupling has been fixed to  $J_H = 0.15 U$ . Vertical black bars indicate the Mott-insulating phase. White arrows mark the evolution of  $U_c$  upon increasing  $J_H$ . Gray crosses are the values for  $U_c$  at  $J_H = 0$ . The inset displays the DOS, used in this model. Materials have been placed according to their experimental value from heat capacity experiments. Taken from [23].

## 2.6 Band structure calculations

In general, the study of strongly correlated systems with photoemission spectroscopy techniques turns out to be a non-trivial task. Electronic interactions induce broadening of the spectral function and produce spectra that are smeared out in both momentum and energy. Specific experimental challenges are described later. In order to support the experimental data analysis, powerful theoretical tools have been used, which will be summarized in the following.

### 2.6.1 Tight binding approximation

We consider a highly practical model in which the formation of bands is understood intuitively. In the *tight binding approximation* (TBA) picture, electronic bands arise by constructing linear combinations of localized atomic orbitals that form Bloch states:

$$\psi_{n,\mathbf{k}}(\mathbf{r}) = \frac{1}{\sqrt{N}} \sum_{\mathbf{R}_j} e^{i\mathbf{k}\cdot\mathbf{R}_j} \phi_n(\mathbf{r} - \mathbf{R}_j), \quad (2.34)$$

with number of lattice sites  $N$ . The main idea in the TBA is to treat the single-particle Hamiltonian perturbatively by combining all potentials of the atoms on the regular lattice sitting at  $\mathbf{R}_j$ ,

$$\mathcal{H} = \mathcal{H}_a(\mathbf{R}_j) + \Delta V_{\mathbf{R}_j}(\mathbf{r}) \quad (2.35)$$

where the perturbation is introduced as:

$$\Delta V_{\mathbf{R}_j}(\mathbf{r}) = \sum_{\mathbf{R}_{j'} \neq \mathbf{R}_j} V_a(\mathbf{r} - \mathbf{R}_{j'}) \quad (2.36)$$

The energy can now be estimated (setting  $\mathbf{R}_{j'} = 0$  due to translational invariance and summed over, eliminating the factor  $1/N$ ):

$$\begin{aligned} \langle \mathcal{H} \rangle_{nn'}(\mathbf{k}) &= 1/N \sum_{\mathbf{R}_j, \mathbf{R}_{j'}} \int d^3r e^{i\mathbf{k} \cdot (\mathbf{R}_{j'} - \mathbf{R}_j)} \phi_n^*(\mathbf{r} - \mathbf{R}_j) [\mathcal{H}_a(\mathbf{R}_{j'}) + \Delta V_{\mathbf{R}_{j'}}(\mathbf{r})] \phi_{n'}(\mathbf{r} - \mathbf{R}_{j'}) \\ &= E_{n'} - \Delta E_{nn'} - \sum_{\mathbf{R}_j \neq 0} e^{-i\mathbf{k} \cdot \mathbf{R}_j} \gamma_{nn'}(\mathbf{R}_j), \end{aligned} \quad (2.37)$$

with

$$\Delta E_{nn'} = - \int d^3r \phi_n^*(\mathbf{r}) \Delta V_{\mathbf{R}_{j'}=0}(\mathbf{r}) \phi_{n'}(\mathbf{r}) \quad (2.38)$$

$$\gamma_{nn'}(\mathbf{R}_j) = - \int d^3r \phi_n^*(\mathbf{r} - \mathbf{R}_j) \Delta V_{\mathbf{R}_{j'}=0}(\mathbf{r}) \phi_{n'}(\mathbf{r}). \quad (2.39)$$

The energy lowering  $\Delta E_{nn'}$ -term can be understood as the electrons feel and benefit from the potential of neighbouring atoms. The second term leads to a  $\mathbf{k}$ -dependence of the eigenenergies. Via the secular equation we can calculate the energies:

$$\det(\langle \mathcal{H} \rangle_{nn'}(\mathbf{k}) - \varepsilon_{\mathbf{k}}) = 0. \quad (2.40)$$

### Bandstructure with $s$ -orbitals

As an example, let's look at  $s$ -orbitals imposed on a simple cubic lattice with lattice parameter  $a$ .

$$\gamma_{s,s'}(\mathbf{R}_j) = \begin{cases} t, & \mathbf{R}_j: \text{nearest neighbours (n. n.)} \\ t', & \mathbf{R}_j: \text{next n. n.,} \end{cases} \quad (2.41)$$

leading to the band structure

$$\begin{aligned}
\varepsilon_{\mathbf{k}} &= E_s + \Delta E_s - t \sum_{\mathbf{R}_j}^{\text{n. n.}} e^{-i\mathbf{k}\cdot\mathbf{R}_j} - t \sum_{\mathbf{R}_j}^{\text{n. n. n.}} e^{-i\mathbf{k}\cdot\mathbf{R}_j} \\
&= E_s + \Delta E_s - 2t \left[ \cos(k_x a) + \cos(k_y a) + \cos(k_z a) \right] \\
&\quad - 4t' \left[ \cos(k_x a) \cos(k_y a) + \cos(k_y a) \cos(k_z a) + \cos(k_z a) \cos(k_x a) \right].
\end{aligned} \tag{2.42}$$

Expanding around  $\mathbf{k} = 0$  (" $\mathbf{k} \cdot \mathbf{p}$ -approximation") yields

$$\varepsilon_{\mathbf{k}} = E_s + \Delta E_s + 6t + 12t' + \frac{\hbar^2}{2m^*} \mathbf{k}^2 + \dots, \tag{2.43}$$

with inverse effective mass

$$\frac{1}{m^*} = \frac{2}{\hbar^2} (t + 4t'). \tag{2.44}$$

### Bandstructure with $t_{2g}$ -orbitals

Next I introduce an application of the TBA of the well-studied FS of  $\text{Sr}_2\text{RuO}_4$  [79, 93, 150–152]. The inner electron-like  $\beta$ -band and the large electron-like  $\gamma$ -band are centered around  $\Gamma$  and the hole-like  $\alpha$ -pocket is located around the zone corner. Let us consider an effective TBA model on a square lattice with lattice constant  $a$  [151, 153, 154]. Here, the weak  $k_z$ -dispersion is neglected. We use the basis  $\Psi(\mathbf{k}) = (\phi_{yz,\mathbf{k}}, \phi_{xz,\mathbf{k}}, \phi_{xy,\mathbf{k}})^\top$ , where  $\phi_{i,\mathbf{k}}$  annihilates a  $t_{2g}$ -orbital  $i \in \{yz, xz, xy\}$  with momentum  $\mathbf{k}$ . Furthermore, the momentum-space Hamiltonian is:

$$\mathcal{H}(\mathbf{k}) = \begin{pmatrix} \varepsilon_{\mathbf{k}}^{yz} - \mu & \varepsilon_{\mathbf{k}}^{\text{off}} + i\lambda & -\lambda \\ \varepsilon_{\mathbf{k}}^{\text{off}} - i\lambda & \varepsilon_{\mathbf{k}}^{xz} - \mu & i\lambda \\ -\lambda & -i\lambda & \varepsilon_{\mathbf{k}}^{xy} - \mu \end{pmatrix}, \tag{2.45}$$

where  $\mu$  denotes the chemical potential and  $\lambda$  parametrizes the spin-orbit coupling. The  $\mathbf{k}$ -dependent matrix elements correspond to the dispersive term in eq. (2.37) and can be written as:

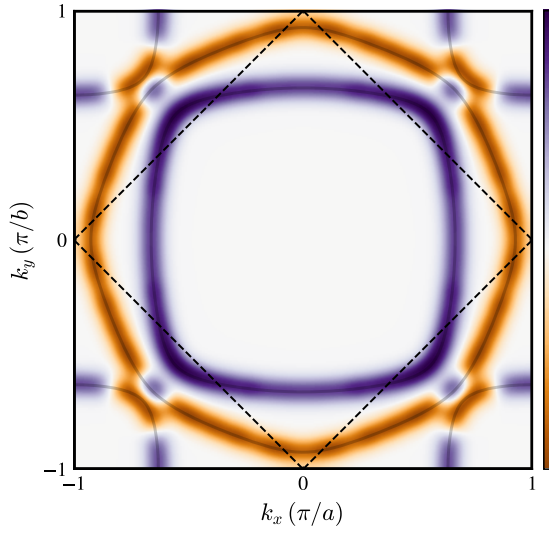


**Fig. 2.6** Tight binding Fermi surface of  $\text{Sr}_2\text{RuO}_4$ , plotted in orbital weight representation. Purple color measures the  $d_{\gamma z}$ -orbital weight and the orange color the  $d_{xy}$ -weight respectively. The thick line marks the first BZ, the dashed line indicates the boundary in a hypothetical band-folding scenario.

$$\begin{aligned}
 -\varepsilon_{\mathbf{k}}^{yz} &= 2t_{yz}^{\perp} \cos(k_x a) + 2t_{yz}^{\parallel} \cos(k_y a), \\
 -\varepsilon_{\mathbf{k}}^{xz} &= 2t_{xz}^{\parallel} \cos(k_x a) + 2t_{xz}^{\perp} \cos(k_y a), \\
 -\varepsilon_{\mathbf{k}}^{xy} &= 2t_{xy} \left[ \cos(k_x a) + \cos(k_y a) \right] + \\
 &\quad 4t'_{xy} \left[ \cos(k_x a) \cos(k_y a) \right] + \\
 &\quad 2t''_{xy} \left[ \cos(2k_x a) + \cos(2k_y a) \right] \\
 -\varepsilon_{\mathbf{k}}^{\text{off}} &= 4t_{\text{off}} \sin(k_x a) \sin(k_y a),
 \end{aligned} \tag{2.46}$$

where values for  $\mu$ ,  $\lambda$  and the matrix elements are taken from ref. [151]:

$$\begin{aligned}
 \mu &= 0.122 \text{ eV}, \quad \lambda = 0.032 \text{ eV} \\
 t_{yz}^\perp &= \gamma_{yz,yz'}(\mathbf{R}_j) = 0.016 \text{ eV} & (\mathbf{R}_j : \text{n. n. along } x) \\
 t_{yz}^\parallel &= \gamma_{yz,yz'}(\mathbf{R}_j) = 0.145 \text{ eV} & (\mathbf{R}_j : \text{n. n. along } y) \\
 t_{xz}^\perp &= \gamma_{xz,xz'}(\mathbf{R}_j) = 0.016 \text{ eV} & (\mathbf{R}_j : \text{n. n. along } y) \\
 t_{xz}^\parallel &= \gamma_{xz,xz'}(\mathbf{R}_j) = 0.145 \text{ eV} & (\mathbf{R}_j : \text{n. n. along } x) \\
 t_{xy} &= \gamma_{xy,xy'}(\mathbf{R}_j) = 0.081 \text{ eV} & (\mathbf{R}_j : \text{n. n.}) \\
 t'_{xy} &= \gamma_{xy,xy'}(\mathbf{R}_j) = 0.039 \text{ eV} & (\mathbf{R}_j : \text{next n. n.}) \\
 t''_{xy} &= \gamma_{xy,xy'}(\mathbf{R}_j) = 0.005 \text{ eV} & (\mathbf{R}_j : \text{next-next n. n.}) \\
 t_{\text{off}} &= \gamma_{nz,nz'}(\mathbf{R}_j) = 0.000 \text{ eV} & (\mathbf{R}_j : \text{n. n.})
 \end{aligned}$$

We can now calculate the band structure by diagonalizing the Hamiltonian and plot the Fermi surface orbitally projected. The components of the resulting eigenvectors are the fractions of the corresponding orbital weights. In Fig. 2.6, the  $d_{yz}$ -weight is plotted in purple and  $d_{xy}$ -weight is orange. Note that along the zone diagonal the spin-orbit interaction  $\lambda$  mixes orbital characters, especially where bands come close to each other along the zone diagonal.

The crystal structure in the Ca-rich region of the  $\text{Ca}_{2-x}\text{Sr}_x\text{RuO}_4$ -phase diagram is orthorhombically distorted. Consequent doubling of the unit cell corresponds to a Brillouin zone (BZ)-halving. To take band folding into account, we formulate the TBA model on two sub-lattices  $\mathcal{A}$  and  $\mathcal{B}$ . In the new basis  $\Psi(\mathbf{k}) = (\phi_{yz,\mathbf{k}}^{\mathcal{A}}, \phi_{xz,\mathbf{k}}^{\mathcal{A}}, \phi_{xy,\mathbf{k}}^{\mathcal{A}}, \mathcal{A} \leftrightarrow \mathcal{B})^\top$  the operator  $\psi_i^n$  annihilates an electron with momentum  $\mathbf{k}$  in a  $t_{2g}$ -orbital  $d_i$  on lattice site  $n$ , with  $i \in \{xy, xz, yz\}$  and  $n \in \{\mathcal{A}, \mathcal{B}\}$ . The tight-binding Hamiltonian is then given by:

$$\mathcal{H}(\mathbf{k}) = \begin{pmatrix} \mathcal{M}_{\mathcal{A}} & \mathcal{M}_{\mathcal{B}} \\ \mathcal{M}_{\mathcal{B}}^\dagger & \mathcal{M}_{\mathcal{A}} \end{pmatrix}, \quad (2.47)$$

where

$$\mathcal{M}_{\mathcal{A}} = \begin{pmatrix} -\mu & i\lambda & -\lambda & 0 \\ -i\lambda & -\mu & i\lambda & 0 \\ -\lambda & -i\lambda & \varepsilon_{\mathbf{k}}^{xy'} - \mu & 0 \end{pmatrix}, \quad \mathcal{M}_{\mathcal{B}} = \begin{pmatrix} \varepsilon_{\mathbf{k}}^{yz} & 0 & 0 \\ 0 & \varepsilon_{\mathbf{k}}^{xz} & 0 \\ 0 & 0 & \varepsilon_{\mathbf{k}}^{xy} \end{pmatrix}, \quad (2.48)$$

$$\begin{aligned}
-\varepsilon_{\mathbf{k}}^{xz} &= 2t_{xz}^{\parallel} \cos(k_+a) + 2t_{xz}^{\perp} \cos(k_-a), \\
-\varepsilon_{\mathbf{k}}^{yz} &= 2t_{yz}^{\perp} \cos(k_+a) + 2t_{yz}^{\parallel} \cos(k_-a), \\
-\varepsilon_{\mathbf{k}}^{xy} &= 2t_{xy} [\cos(k_+a) + \cos(k_-a)], \\
-\varepsilon_{\mathbf{k}}^{xy'} &= 2t'_{xy} [\cos(k_xa) + \cos(k_ya)] + \\
&\quad 2t''_{xy} [\cos(2k_+a) + \cos(2k_-a)]
\end{aligned} \tag{2.49}$$

with  $k_+ = (k_x + k_y)/2$  and  $k_- = (k_x - k_y)/2$ .

### FS fitting procedure

The fitting procedure requires an appropriate metric to measure the deviation of the model prediction  $\varepsilon(\mathbf{k}_i, \theta)$  with fit parameters  $\theta = \{\gamma_{nn'}(\mathbf{R}_j), \mu, \lambda\}$  from the experimental data  $\varepsilon_i^{\text{exp}}$ . Data points are extracted either by fitting MDCs with Lorentzians, EDCs with model spectral functions or manually, if data quality allows. For  $N$  such data points, the *fitness* norm  $\xi$  is defined as:

$$\xi(\theta) = \frac{1}{N} \sum_{i=0}^{N-1} \min_{\varepsilon(\mathbf{k}_i, \theta) \in \text{diag}\mathcal{H}(\mathbf{k}_i, \theta)} |\varepsilon_i^{\text{exp}} - \varepsilon(\mathbf{k}_i, \theta)|. \tag{2.50}$$

The objective is to minimize  $\xi$  iteratively with a better choice of tight binding parameters  $\theta_i$ . Until convergence is reached, the parameters  $\theta_t$  are updated after every iteration step  $t$  as follows [155]:

$$\begin{aligned}
t &\leftarrow t + 1 \\
m_t &\leftarrow \beta_1 \cdot m_{t-1} + (1 - \beta_1) \cdot \nabla_{\theta_i, t-1} \xi(\theta_{t-1}) \\
v_t &\leftarrow \beta_2 \cdot v_{t-1} + (1 - \beta_2) \cdot (\nabla_{\theta_i, t-1} \xi(\theta_{t-1}))^2 \\
\theta_t &\leftarrow \theta_{t-1} - \hat{\alpha} \cdot \frac{m_t}{\sqrt{v_t} + \varepsilon},
\end{aligned} \tag{2.51}$$

where  $m_0 = 0$  (first moment),  $v_0 = 0$  (second moment), decay rates  $\beta_1 = 0.9$ ,  $\beta_2 = 0.999$ ,  $\varepsilon = 1 \times 10^{-8}$  and learning rate  $\hat{\alpha} = \alpha \cdot \sqrt{\frac{1-\beta_2}{1-\beta_1}}$  with  $\alpha = \mathcal{O}(-4)$ .

### 2.6.2 Density functional theory

Density functional theory (DFT) is a powerful *ab initio* method that forms the basis of all modern electronic structure calculations [114]. It is based on the implementation of the Hohenberg-Kohn (HK) theorem which are known as the Kohn-Sham (KS) equations, which are solved self-consistently. The KS eigenvalues are usually interpreted as the

true single particle energies. DFT works reasonably well for metals but does not describe gapped systems well. For a system of  $N$  interacting Fermions, consider the Hamiltonian

$$\mathcal{H} = T + V + W = -\frac{\hbar^2}{2m} \sum_i \nabla_i^2 + \sum_i V(\mathbf{r}_i) + \frac{1}{2} \sum_{i \neq j} W(|\mathbf{r}_i - \mathbf{r}_j|), \quad (2.52)$$

where  $T$  represents the kinetic energy,  $V$  is the Coulomb potential and  $W$  describes electron-electron interactions. For a given external potential  $V_{\text{ext}}(\mathbf{r})$ , the HK theorem states that the energy functional for the ground state

$$E_{\mathcal{G}}[n] = \langle \Psi_{\mathcal{G}}[n] | \mathcal{H}^{(V_{\text{ext}})} | \Psi_{\mathcal{G}}[n] \rangle = \langle \Psi_{\mathcal{G}}[n] | T + W + V_{\text{ext}} | \Psi_{\mathcal{G}}[n] \rangle \quad (2.53)$$

reaches its minimum when the particle number density  $n(\mathbf{r})$  is equal to the true ground state density with ground state energy  $E_0$ . Also the map that relates the density to the ground state wavefunction  $\Psi_{\mathcal{G}}(\mathbf{r})$  does not depend on the explicit form of  $V_{\text{ext}}(\mathbf{r})$ . We can then split the energy functional into

$$E_{\mathcal{G}}[n] = F_{\text{HK}}[n] + \int d\mathbf{r}^3 V_{\text{ext}}(\mathbf{r}) n(\mathbf{r}) \quad (2.54)$$

with the universal functional

$$F_{\text{HK}}[n] = T[n] + W[n] = \langle \Psi_{\mathcal{G}}[n] | T + W | \Psi_{\mathcal{G}}[n] \rangle. \quad (2.55)$$

The difficulty is now to find appropriate approximations of the exact form of  $F_{\text{HK}}$  that are needed to solve the problem. Kohn and Sham proposed, that there exists a (reference) system of non-interacting particles with the same ground state density as the interacting one, with a corresponding (unique) energy functional

$$E_{\mathcal{G}}^{\text{ref}}[n] = T^{\text{ref}}[n] + \int d\mathbf{r}^3 V^{\text{ref}}(\mathbf{r}) n(\mathbf{r}), \quad (2.56)$$

with ground state density  $n_{\text{ref}}(\mathbf{r})$  when solving the variational problem  $\delta E_{\mathcal{G}}^{\text{ref}}[n] = 0$ .  $T^{\text{ref}}[n]$  is the "left-over" from  $F_{\text{HK}}[n]$  for non-interacting particles. The objective is to find the external reference potential  $V_{\text{ext}}^{\text{ref}}(\mathbf{r})$ . Details of the derivation can be found in various text books, which finally yield:

$$V_{\text{ext}}^{\text{ref}}(\mathbf{r}) = V_{\text{ext}}(\mathbf{r}) + \int d\mathbf{r}'^3 W(\mathbf{r}, \mathbf{r}') n_{\text{ext}}(\mathbf{r}') + V_{\text{xc}}([n_{\text{ext}}], \mathbf{r}). \quad (2.57)$$

This means that if we had the knowledge about the exact form of the exchange-correlation potential  $V_{\text{xc}}([n_{\text{ext}}], \mathbf{r})$ , we could solve the KS equations

$$\left( -\frac{\hbar^2}{2m} \nabla^2 + V_{\text{ext}}^{\text{ref}}(\mathbf{r}) \right) \psi_i(\mathbf{r}) = \varepsilon_i \psi_i(\mathbf{r}), \quad \varepsilon_1 \leq \varepsilon_2 \leq \dots \quad (2.58)$$

and therefore determine the true ground state density of the interacting system

$$n(\mathbf{r}) = \sum_i^N |\psi_i(\mathbf{r})|^2. \quad (2.59)$$

In the LDA, the exchange energy per particle can be computed exactly for the homogeneous electron gas. The correlation energy can be calculated by efficient algorithms (i. e. Monte Carlo) and then parametrized as a function of the density. With that knowledge, the key idea in LDA is to consider the real system being composed of infinitesimal volume elements of constant, local density.

### 2.6.3 Dynamical mean field theory

In the 1990s, a highly potent computational method emerged in condensed matter physics. Dynamical mean field theory (DMFT) allows a quantitative estimate of the self-energy  $\Sigma(\omega)$ , enhancing the predictive power of band structure calculations dramatically. Instead of viewing the solid as an inhomogeneous electron gas, DMFT takes into account the multiplet structure of the atom. The idea is to generalize the concept of the Weiss-field in magnetism to quantum many-body systems [112]. In the mean field approximation in magnetism, the many-body problem (with two-spin operators) is reduced to a single particle problem, understood as a paramagnet in a magnetic field. The thermal average of the spin projection is then obtained self-consistently with the help of the Brillouin function. In DMFT the observable is the local Green's function. It can be calculated by considering the coupling of an atomic shell to an effective medium. The coupling is represented by an energy-dependent dynamical mean field  $\Delta$ . A central assumption in DMFT is that the self energy of this quantum impurity model  $\Sigma_{\text{imp}}$  can be viewed as an approximation of the self-energy of the solid  $\Sigma$ . The self-consistency condition is the requirement that the impurity Green's function coincides with the local lattice Green's function. Details to the DMFT loop and theoretical calculations can be found in ref. [112].



# Chapter 3

## Concepts in photoemission spectroscopy

Already a decade before the discovery of the electron by Sir Joseph John Thomson in 1897 [156], Heinrich Hertz observed that an electric spark between two electrodes is more easily created by illuminating them with ultraviolet light [157]. At the beginning of the next century, Philipp Lenard carried out more systematic experiments, investigating the rays produced by irradiating metals. He found that the energy of the rays was independent of the light intensity, but scaled with its frequency [158]. This intriguing result was explained by Albert Einstein in his miraculous year 1905 by introducing the light quantum of energy  $h\nu$  [159], yielding the equation

$$\hat{E}_{\text{kin}} = h\nu - \Phi \quad (3.1)$$

where  $\hat{E}_{\text{kin}}$  is the kinetic energy of the fastest emitted electrons and  $\Phi$  is the *work function* of the metal surface. This relation has been confirmed 1916 by Robert Millikan [160], thus providing direct measurement of Planck's constant  $h$ . With the development of quantum mechanics and theoretical concepts in atomic and solid state physics, the fundamentals for photoelectron spectroscopy have been laid out. In the 1950's Ralph Steinhardt [161] and Kai Siegbahn [162] developed independently X-ray photoelectron spectroscopy (XPS) for general chemical analysis. The DOS can be measured as a function of binding energy  $E_B$  (Fig.3.1) by using the energy conservation law

$$E_{\text{kin}} = h\nu - \Phi - E_B \quad (3.2)$$

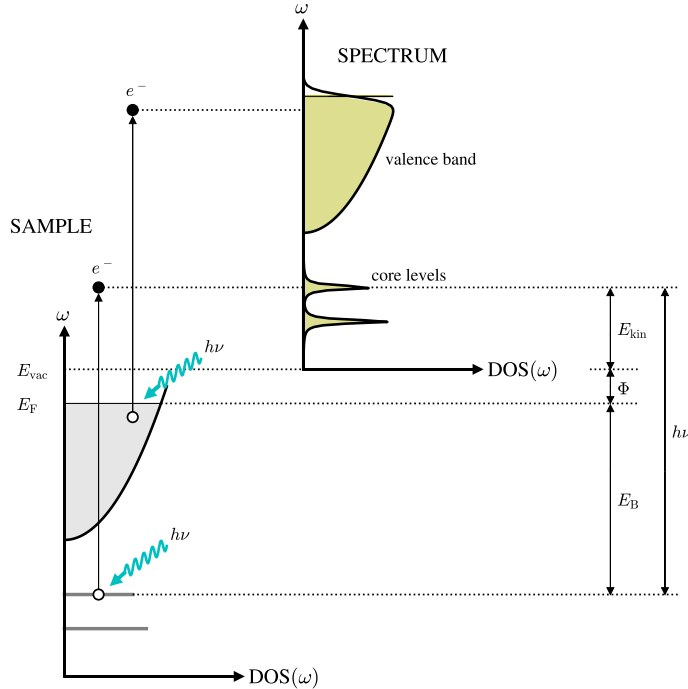


**Fig. 3.1** Schematic illustration of the density of states inside the sample and in vacuum. Electrons excited from the valence band (filled up to the Fermi energy  $E_F$ ) or core levels obey energy conservation.

In the following decades powerful instruments have been developed. With ARPES, direct access to momentum space has been reached. This boosted ARPES to one of the most powerful and widely used experimental tools in condensed matter physics [120, 163], as it enables a full mapping of the electronic band structure. Recent developments are time resolving pump-probe experiments [164], spin-resolved photoemission [165] and spectromicroscopic nano-ARPES [166].

### 3.1 Photoemission process

After Einstein's explanation of the photoelectric effect, sophisticated models contributed to a more profound understanding of the photoemission process. A rigorous quantum mechanical treatment of the process goes beyond the scope of this introduction. In the ARPES community, a simplified *three-step model* is widely used. Despite its phenomenological origin, it has been proven to be rather successful [167–169].

- Step one: Absorption of the photon and optical excitation of an electron in the bulk,
- Step two: Electron transport to the surface,
- Step three: Transmission through the surface and escape into vacuum.

### 3.1.1 Step one: Optical excitation

Time dependent perturbation theory in quantum mechanics predicts electronic transition probabilities for  $N$ -electron systems upon a perturbation or interaction Hamiltonian  $\mathcal{H}_{\text{int}}(t)$ . In the interaction picture (*Dirac picture*) of quantum mechanics, the transition rate only depends on  $\mathcal{H}_{\text{int}}(t)$ . Considering a finite light wave perturbing a system of  $N$  charged particles with Hamiltonian

$$\mathcal{H}(t) = \sum_{j=1}^N \frac{1}{2m} \left( \mathbf{p}_j - e\mathbf{A}(\mathbf{r}_j, t) \right)^2 + V(\mathbf{r}_1, \dots, \mathbf{r}_N) \equiv \mathcal{H}_0 + \mathcal{H}_{\text{int}}(t) \quad (3.3)$$

In the Coulomb gauge  $\nabla \cdot \mathbf{A}(\mathbf{r}, t) = 0 = -i\hbar \sum_{i=1}^3 \partial_i A_i = \sum_{i=1}^3 [p_i, A_i]$ :

$$\mathcal{H}_0 = \sum_{j=1}^N \frac{1}{2m} \mathbf{p}_j^2 + V(\mathbf{r}_1, \dots, \mathbf{r}_N) \quad (3.4)$$

$$\mathcal{H}_{\text{int}}(t) = - \sum_{j=1}^N \frac{e}{m} \mathbf{A}(\mathbf{r}_j, t) \cdot \mathbf{p}_j + \sum_{j=1}^N \frac{e^2}{2m} \mathbf{A}(\mathbf{r}_j, t)^2 \quad (3.5)$$

For wavelengths much larger than the atomic length scale,  $\mathbf{A}(\mathbf{r}_j, t)$  is independent of  $\mathbf{r}_j$ . This is the dipole approximation.

$$\mathbf{A}(\mathbf{r}_j, t) \Psi_i^N(\mathbf{r}_1, \dots, \mathbf{r}_N) \approx \mathbf{A}(0, t) \Psi_i^N(\mathbf{r}_1, \dots, \mathbf{r}_N) \quad (3.6)$$

$\Psi_i^N$  is the initial  $N$ -body wave function. In this fashion, the quadratic term in  $\mathcal{H}_{\text{int}}(t)$  is a constant and can be dropped (it only contributes a phase factor when evaluating the matrix element). Using the commutation relation  $\frac{i}{\hbar} [\mathcal{H}_0, \mathbf{r}_j] = \frac{\mathbf{p}_j}{m}$

$$\mathcal{H}_{\text{int}}(t) = - \frac{e}{m} \mathbf{A}(0, t) \cdot \sum_{j=1}^N \mathbf{p}_j = - \mathbf{A}(0, t) \cdot \frac{i}{\hbar} [\mathcal{H}_0, \mathbf{P}], \quad \mathbf{P} = e \sum_{j=1}^N \mathbf{r}_j \quad (3.7)$$

with electric dipole operator  $\mathbf{P}$ . Assuming a harmonic perturbation the transition rate is derived, known as *Fermi's golden rule*:

$$\Gamma_{i \rightarrow f} = \frac{2\pi}{\hbar} |\langle \Psi_f^N | \mathcal{H}_{\text{int}} | \Psi_i^N \rangle|^2 \delta(E_f^N - E_i^N - h\nu) \quad (3.8)$$

with the matrix element

$$\langle \Psi_f^N | \mathcal{H}_{\text{int}} | \Psi_i^N \rangle = \langle \Psi_f^N | [\mathcal{H}_0, \mathbf{P}] | \Psi_i^N \rangle = (E_i^N - E_f^N) \langle \Psi_f^N | \mathbf{P} | \Psi_i^N \rangle. \quad (3.9)$$

The absorption of a photon of energy  $h\nu$  excites an initial state  $|\Psi_i^N\rangle$  of energy  $E_i^N$  to a final state  $\langle\Psi_f^N|$  of energy  $E_f^N$ .

It is convenient to factorize the  $N$ -particle state into a single photoelectron state  $|\phi^k\rangle$  and a  $N - 1$  particle state  $|\Psi^{N-1}\rangle$ . Since the system will relax after the excitation process and screen the photohole, we make use of the *sudden approximation*. As the name suggests, we assume the photoemission process to be sudden (instantaneous electron removal), with no further interactions between the free photoelectron and the  $N - 1$  electron system accompanied by a discontinuous change of its effective potential. To account for proper fermionic spin-statistics we use the orthogonal projector  $\hat{\mathcal{A}}$  to antisymmetrize the product states:

$$|\Psi_\alpha^N\rangle = \hat{\mathcal{A}}(|\phi_\alpha^k\rangle \otimes |\Psi_\alpha^{N-1}\rangle), \quad \alpha = \{i, f\} \quad (3.10)$$

This approximation is valid for high kinetic energies of the photoelectrons but has proven its validity even to some degree for kinetic energies down to 20 eV in cuprate high- $T_c$  superconductors [170]. For the initial state we use this factorized form by means of a Slater determinant in the Hartree-Fock formalism. We define the photoelectron dipole matrix element  $\mathcal{M}_{i,f} \equiv \langle \phi_f^k | \mathcal{H}_{\text{int}} | \phi_i^k \rangle$  and decompose the  $N - 1$  final state into its eigenstate components  $\Psi_f^{N-1} = \sum_m \Psi_{f,m}^{N-1}$  with the overlap integrals  $c_{m,i} = \langle \Psi_m^{N-1} | \Psi_i^{N-1} \rangle$ . The total photoemission intensity  $I_0(\mathbf{k}, E_{\text{kin}}) \propto \sum_{i,f} \Gamma_{i \rightarrow f}$  is proportional to:

$$I_0(\mathbf{k}, E_{\text{kin}}) \propto \sum_{i,f} |\mathcal{M}_{i,f}|^2 \sum_m |c_{m,i}|^2 \delta(E_{\text{kin}} + E_m^{N-1} - E_i^N - h\nu) \quad (3.11)$$

In solids with strong electronic correlations the removal of the photoelectron results in a strong change of the effective potential such that  $\Psi_i^{N-1}$  overlaps with many eigenstates  $\Psi_m^{N-1}$ . A rigorous determination of the  $c_{m,i}$ 's would be complicated and inefficient. In the framework of many-body perturbation theory a slightly different expression has been developed to describe quasiparticle excitations near the Fermi level with excitation energy  $\omega$ :

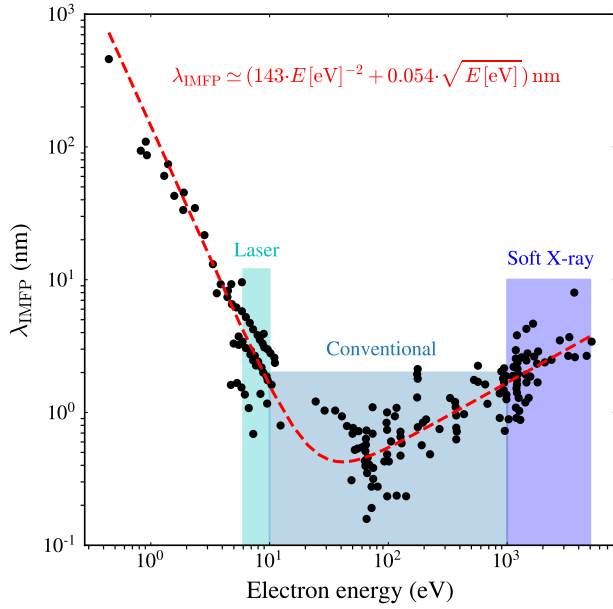


**Fig. 3.2** Electron energy versus inelastic mean free path. Black data points of different materials, taken from [171]. The universal curve is approximated by the red dashed line. Shaded areas indicate the range for several photon sources: Laser-, conventional- and soft X-ray-ARPES.

$$I_0(\mathbf{k}, \omega) \propto \sum_{i,f} |\mathcal{M}_{i,f}|^2 \mathcal{A}(\mathbf{k}, \omega) f(\omega, T) \quad (3.12)$$

where  $\mathcal{A}(\mathbf{k}, \omega)$  is the one particle spectral function that contains all the many-body effects of the electronic excitation and  $f(\omega, T) = (e^{(\omega-\mu)/k_B T} + 1)^{-1}$  is the Fermi-Dirac distribution for state occupation statistics.

### 3.1.2 Step two: Propagation to the surface

When the optically excited photoelectron travels deep from the sample to the surface, it may suffer inelastic scattering events. In a simplified fashion, one can describe inelastic scattering interactions by an empirical *universal curve* for the inelastic mean free path  $\lambda_{\text{IMFP}}$ , which turns out to be nearly material independent as a function of electron kinetic energy [171] (Fig. 3.2).

During our performed synchrotron experiments photon energies in the range of  $h\nu = 30 - 120$  eV were used corresponding to an escape depth of order  $\lambda_{\text{IMFP}} \sim 5$  Å, thus dealing with extreme surface sensitivity. To probe a larger bulk contribution, other photon energy ranges have to be chosen. In the lower end, laser sources ( $\sim 6 - 10$  eV)

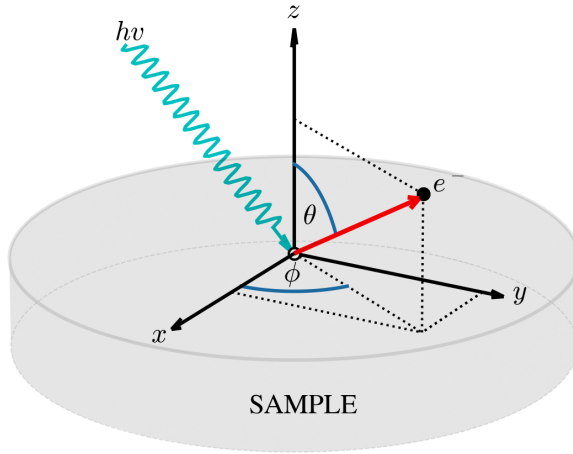


**Fig. 3.3** Schematic illustration of the photon-in / electron-out geometry with azimuth  $\phi$  and polar angle  $\theta$ .

provide excellent energy and momentum resolution but only access a small part of reciprocal space. At high energies, soft X-rays ( $\sim 1\text{--}5\text{ keV}$ ) probe higher zones on the cost of experimental resolution. The short probe depth is comparable to the layer spacing in transition metal oxides, in favour of the sudden approximation.

### 3.1.3 Step three: Transmission into vacuum

A fundamental difficulty in ARPES is the relation between the wave vector  $\mathbf{k}_f$  of the photoelectron at the detector and  $\mathbf{K}_f$  inside the crystal. This problem arises from the fact that only the kinetic energy of the electron is measured and not its momentum [172]. The transmission process must obey energy and momentum conservation, dictating the kinetic energy of the photoelectrons with binding energy  $E_B$ , given by eq. (3.2). Together with detector angles, polar  $\theta$  and azimuthal  $\phi$  (see Fig. 3.3) the final state wave vector of a free electron in vacuum is given as

$$\mathbf{k}_f = \frac{1}{\hbar} \sqrt{2mE_{\text{kin}}} (\sin \theta \cos \phi, \sin \theta \sin \phi, \cos \theta)^\top \quad (3.13)$$

As the dispersion  $\epsilon_{\mathbf{K}_f}$  of the photoelectron inside the solid is generally unknown, derivation of  $\mathbf{K}_f$  is not possible. In addition, the photoelectron has to overcome the surface barrier resulting in refraction. In this process, the periodic crystal potential ensures conservation of the parallel components  $\mathbf{k}_f^{\parallel} = \mathbf{K}_f^{\parallel}$ . Perpendicular to the surface, translation symmetry of the crystal potential is broken by a potential step  $-V_0$  in the solid to zero in vacuum.  $V_0$  arises as a mean potential, that the photoelectron has to overcome and is of order 10 eV. The complexity of this problem is reduced in the *free*

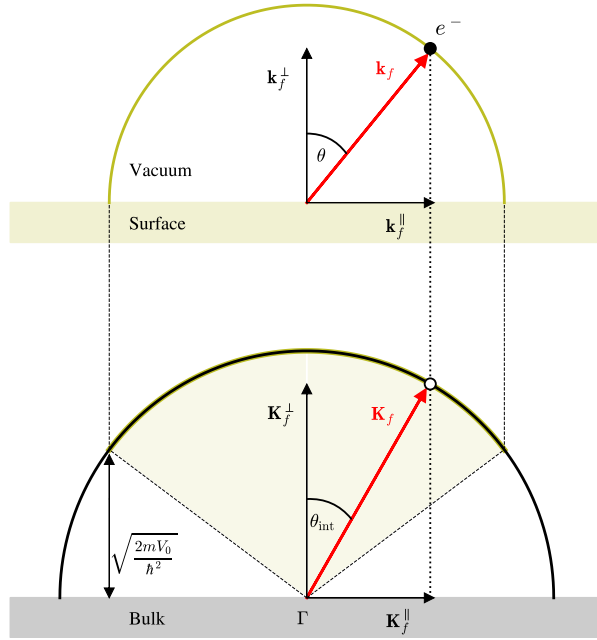


**Fig. 3.4** Electron transmission through the surface. The inner potential  $V_0$  that has to be overcome breaks crystal translational symmetry perpendicular to the surface.

*electron final state approximation*, where the photoelectron inside the bulk is treated as a single plane wave such that:

$$\mathbf{K}_f = \frac{1}{\hbar} \sqrt{2m(E_{\text{kin}} + V_0)} (\sin \theta_{\text{int}} \cos \phi, \sin \theta_{\text{int}} \sin \phi, \cos \theta_{\text{int}})^{\top} \quad (3.14)$$

where  $\theta_{\text{int}}$  is the internal polar angle in the crystal. These relations imply immediately that for photons with higher energies, we are able to probe higher Brillouin zones (BZ), thus increasing  $\mathbf{K}_f^{\perp}$  when  $\mathbf{K}_f^{\parallel}$  is fixated. This leads to an analogous of Snell's refraction law in optics (Fig. 3.4):

$$\sin \theta_{\text{int}} = \sin \theta \sqrt{\frac{E_{\text{kin}}}{E_{\text{kin}} + V_0}}. \quad (3.15)$$

Furthermore, the conservation of  $\mathbf{k}_f^{\parallel}$  leads to exact mapping of the energy dispersion of two-dimensional systems and other surface states, i. e. Shockley state on a clean Cu(111) surface [173].

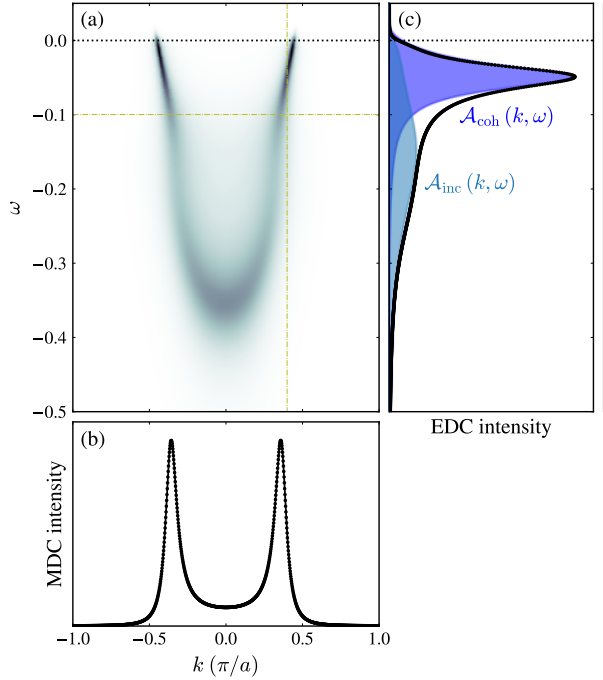


**Fig. 3.5** (a) Model spectral function multiplied with a Fermi Dirac distribution. (b) MDC at energy  $\omega = -0.1$  eV. (c) EDC at momentum  $k$ . Coherent pole and incoherent weight are indicated by the shaded area.

## 3.2 Experiment

### 3.2.1 EDC's and MDC's

Modern energy analyzers in ARPES experiments collect data, simultaneously resolving energy and momentum. It is convenient however, to slice the intensity maps where either momentum is fixated in an energy distribution curve (EDC) or energy is fixated in a momentum distribution curve (MDC), shown in Fig. 3.5.

In the vicinity of  $E_F$  and far from the band bottom, the bare band energy in eq. 2.14 can be written as  $\epsilon_{\mathbf{k}}^b = v_F^b(k - k_F)$ , with the band velocity at the Fermi level  $v_F^b = \partial\epsilon_{\mathbf{k}}^b/\partial k$ . The MDC is given by:

$$\mathcal{A}(\mathbf{k}, \omega) \simeq -\frac{1}{\pi} \frac{\Im\Sigma(\omega)}{\left[\omega - \Re\Sigma(\omega) - v_F^b(k - k_F)\right]^2 + \Im\Sigma(\omega)^2}, \quad (3.16)$$

a Lorentzian with half width at half maximum  $\Delta k_{\text{HWHM}}(\omega) = \Gamma = \Im\Sigma(\omega)/v_F^b$  [174, 175]. The symmetric lineshape and the simple background makes an MDC less complicated to analyze than an EDC.

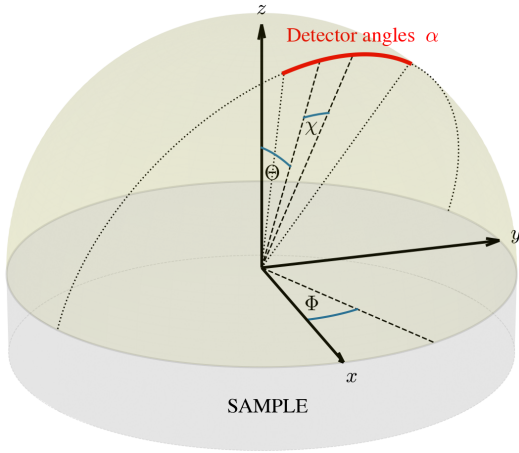


**Fig. 3.6** Sketch of the rotational degrees of freedom of a six-axis ARPES manipulator.

As a general note, for anisotropic systems with commonly rather complex Fermi surfaces, the self-energy  $\Sigma(\omega)$  is not momentum independent [128]. However, the energy dependence should still dominate over the momentum dependence of i. e. electron-phonon coupling contributions as demonstrated in the charge density wave system 2H-TaSe<sub>2</sub> [176].

### 3.2.2 Angles to $k$ -space conversion

In order to display the intensity maps properly in  $k$ -space, the angles have to be transformed in the spirit of equation (3.13). Six-axis manipulators have three translational and three rotational degrees of freedom. This is illustrated in Fig. 3.6 and is demonstrated as follows.

Let us start with the intrinsic coordinate system of the manipulator  $\Sigma'(x', y', z')$  aligned with the laboratory coordinate system  $\Sigma(x, y, z)$ . For now, it is assumed that the crystallographic axes  $a, b, c$  are congruent with the manipulator axes as well. The analyzer slit lies in the  $yz$ -plane with  $\alpha$  denoting the detector angle (rotation around  $x$ ). In this initial configuration the momentum of the photoelectron is:

$$\mathbf{k} = \frac{1}{\hbar} \sqrt{2mE_{\text{kin}}} \begin{pmatrix} -\sin \alpha \\ 0 \\ \cos \alpha \end{pmatrix} \quad (3.17)$$

For an arbitrary angular setting of the manipulator, the rotations are described by  $\Theta$  (around  $y$ ),  $\chi$  (around  $x'$ ) and  $\Phi$  (around  $z'$ ). The corresponding rotation matrices are given as

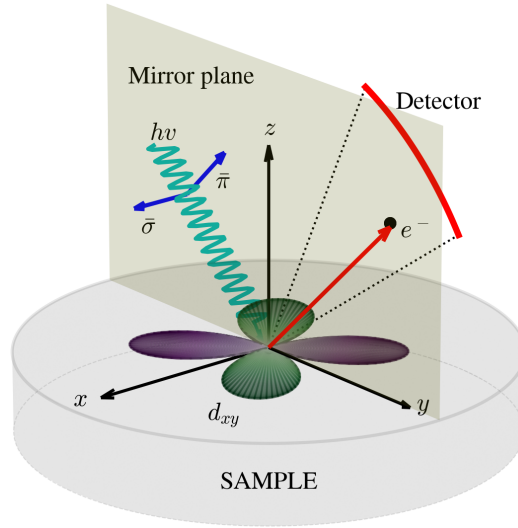


**Fig. 3.7** Experimental setup for matrix element analysis. The mirror plane, spanned by the outgoing photoelectron and the incoming light, defines the parity of a given orbital (here  $d_{xy}$  is shown). The  $\bar{\pi}$ -polarization vector lies within the plane and the  $\bar{\sigma}$  vector points out-of-plane.

$$R_\Theta = \begin{pmatrix} \cos \Theta & 0 & -\sin \Theta \\ 0 & 1 & 0 \\ \sin \Theta & 0 & \cos \Theta \end{pmatrix}, R_\chi = \begin{pmatrix} 1 & 0 & 0 \\ 0 & \cos \chi & \sin \chi \\ 0 & -\sin \chi & \cos \chi \end{pmatrix}, R_\Phi = \begin{pmatrix} \cos \Phi & -\sin \Phi & 0 \\ \sin \Phi & \cos \Phi & 0 \\ 0 & 0 & 1 \end{pmatrix}$$

To account for the common case, that the crystal  $c$ -axis is misaligned with respect to the manipulator  $z'$ -axis, the final adjustment is done with rotations  $\gamma$  (mismatch  $c$ -axis and  $z'$ -axis) and  $\beta$  (angle between  $a$ -axis and  $x'$ -axis).

$$R_\gamma = \begin{pmatrix} \cos \gamma & 0 & -\sin \gamma \\ 0 & 1 & 0 \\ \sin \gamma & 0 & \cos \gamma \end{pmatrix}, R_\beta = \begin{pmatrix} \cos \beta & -\sin \beta & 0 \\ \sin \beta & \cos \beta & 0 \\ 0 & 0 & 1 \end{pmatrix}$$

By careful observation how the rotation matrices manipulate the  $\mathbf{k}$ -vector, the transformed momentum  $\mathbf{k}'$  of the photoelectron is

$$\mathbf{k}' = R_\beta R_\gamma R_{-\beta} R_\Phi R_\chi R_\Theta \mathbf{k}. \quad (3.18)$$

<b>P</b>	$d_{xy}$	$d_{xz}$	$d_{yz}$	$d_{z^2}$	$d_{x^2-y^2}$
Orientation along $b$ -axis (transition metal – oxygen direction)					
$\bar{\sigma}$	$\langle +  -   - \rangle \neq 0$	$\langle +  -   - \rangle \neq 0$	$\langle +  -   + \rangle = 0$	$\langle +  -   + \rangle = 0$	$\langle +  -   + \rangle = 0$
$\bar{\pi}$	$\langle +  +   - \rangle = 0$	$\langle +  +   - \rangle = 0$	$\langle +  +   + \rangle \neq 0$	$\langle +  +   + \rangle \neq 0$	$\langle +  +   + \rangle \neq 0$

**Table 3.1** Matrix elements. Photoemission selection rules are dictated by the total parity of the product  $\langle \phi_f | \mathbf{P} | \phi_i \rangle$ . The table is based on the sketch in Fig. 3.7.

### 3.2.3 Matrix element effects

The measured photocurrent in ARPES is governed by the matrix element of the optical transition  $\mathcal{M}_{i,f}$ . By varying light polarization or photon energy,  $\mathcal{M}_{i,f}$  and therefore the intensity of spectral features transform. Such changes contain information about the orbital character of the electronic bands. Consider an experimental setup in which the incoming light and the outgoing photoelectron span a mirror plane, perpendicular to the sample surface (see Fig. 3.7). With respect to this plane, the light polarization vector  $\varepsilon$  has either even parity "+" ( $\bar{\pi}$ -polarization) or odd parity "-" ( $\bar{\sigma}$ ) and an assumed free electron final state with even parity. The total parity of  $\mathcal{M}_{i,f} = \langle \phi_f | \mathcal{H}_{\text{int}} | \phi_i \rangle \propto \langle \phi_f | \mathbf{P} | \phi_i \rangle$  eq. (3.9) dictates if the matrix element vanishes or not (see Tab. 3.1).

### 3.2.4 Sample preparation

High quality ruthenate single crystals were grown at the SPIN institute near Salerno, Italy<sup>1</sup>. For all crystals, the flux-feeding floating-zone technique was used. In this process, polycrystals are melted locally and subsequently solidified in a single crystalline form. At the same time, impurities are carried away as the molten zone is moved along the crystal. Synthesis of the ruthenate crystals follows a recipe outlined by S. Nakatsuji and Y. Maeno [177]. Quality of single-crystallinity at room temperature was checked by Laue X-ray diffraction.

Prior to our ARPES experiments, the crystals were glued on a metallic sample holder using electrically conducting, two component silver epoxy paste (EPO-TEK E4110). The silver epoxy cured over night using a heating plate. For  $\text{Ca}_2\text{RuO}_4$  the curing temperature was stabilized at  $75^\circ\text{C}$ , just below the structural phase transition temperature  $T_S \approx 350\text{ K}$ . For other crystals higher temperatures ( $> 100^\circ\text{C}$ ) are used for curing and

---

<sup>1</sup>by Rosalba Fittipaldi, Veronica Granata and Antonio Vecchione

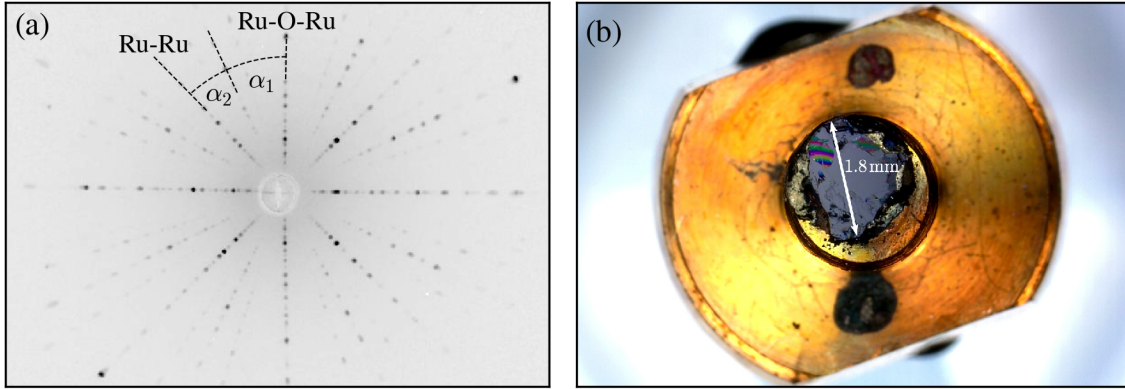


**Fig. 3.8** a) Laue diffraction pattern of  $\text{Ca}_2\text{RuO}_4$  in the  $ab$  plane with angles  $\alpha_1 > \alpha_2$  between zero- and first-order resonances as indicated. b) Corresponding sample (black) glued with silver-epoxy on the sample holder.

thus generally improved conductivity is achieved. Usage of conducting glue is crucial to electrically ground the sample. Since in the photoemission process electrons are removed from the material, an insulating sample is prone to charge up electrostatically. In an ARPES spectra this induces unwanted shifts of the Fermi level which is typically sensitive to the incident photon flux. The silver epoxy provides an electronic and mechanical connection of the sample to an electron reservoir (sample holder). We can align the crystallographic axes of the sample with a Laue X-ray diffractometer. A typical Laue-pattern of a Pbca crystal structure of our ruthenates is shown in Fig. 3.8 (X-ray beam along the  $c$ -axis). The brightest zero-order pattern form two hair crosses rotated 45 deg to each other. Relative to the first-order resonances, the Ru-Ru bond represents the hair cross enclosing a smaller angle. For transport from our laboratory to the synchrotron beamlines, specific sample boxes were used (drawing in the Appendix C).

ARPES probes the first few layers of the crystal, so it is absolutely crucial that the surface is and stays clean. During the experiment, the samples are held in an ultra high vacuum environment with base pressure of order  $10^{-11}$  mbar. The layered structure of our ruthenate crystals allows cleaving the sample *in-situ* with a top-post.

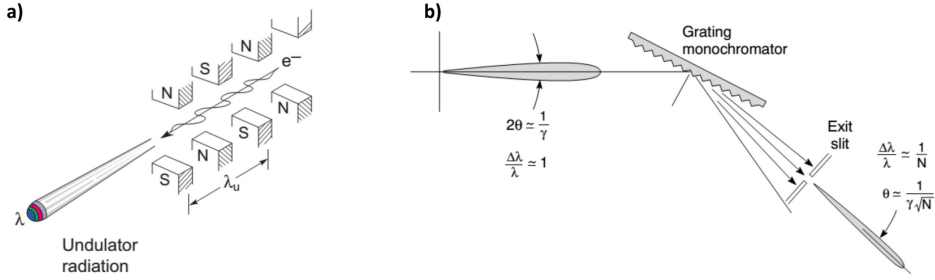


**Fig. 3.9** Schematic illustration of synchrotron light generation. a) Electrons traversing the undulator undergo meander-like oscillations and radiate. b) The narrow beam cone is optimized by different optical elements. Adapted from ref. [179].

	I05	SIS	MAESTRO	$1^3$
Photon spot size ( $\mu\text{m}^2$ )	$< 50 \times 50$	$< 50 \times 100$	$< 10 \times 10$	unkown
Energy resolution (meV)	5 – 10	$\sim 10$	$\sim 10$	$\sim 1$
Angular resolution ( $^\circ$ )	$\sim 0.1$	$\sim 0.15$	$\sim 0.1$	$\sim 0.1$
Photon energies (eV)	18 – 240	10 – 800	20 – 1000	4 – 200
Temperatures (K)	6 – 300	10 – 300	$< 12 – 400$	1 – 3

**Table 3.2** Endstation specifications at different synchrotron facilities, see main text.

### 3.2.5 Experimental environment

#### Synchrotron facilities

The biggest advantage of synchrotron light over conventional gas-discharge lamps (i.e. He, Xe) or laser sources is the possibility to tune the photon energy over a wide range at a high intensity and to change polarization of the incident light. In generic synchrotron facilities, electrons are brought to high velocities ( $v \approx c$ ) by a linear accelerator and injected into a storage ring, equipped with *undulators* (an array of  $N$  aligned, pole alternating magnet pairs). The electrons in the storage ring are kept at a constant kinetic energy (2.4 GeV at SLS) and produce the synchrotron light due to their meander-shaped motion in the undulators. Details of a synchrotron light source can be found in ref. [178]. At relativistic speeds the angular distribution of the light forms a very narrow cone<sup>2</sup> of width  $2/\gamma$  ( $\gamma = (1 - \beta)^{-1/2}$ ,  $\beta = v/c$ ). Before the photons hit the sample, they are directed onto plane gratings (monochromator) and through the exit slit (collimator) that together set the energy resolution of the beam.

<sup>2</sup>for  $v \ll c$ , the light is emitted isotropically similar to an oscillating dipole or antenna.

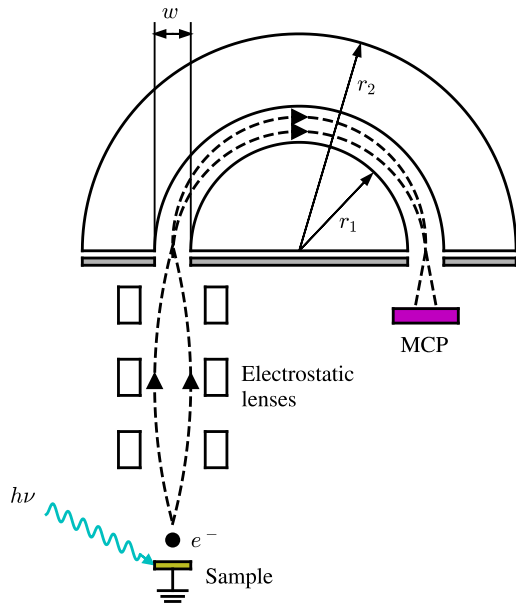


**Fig. 3.10** Emitted photoelectron are focused by electrostatic lenses and pass through the hemispherical analyzer before reaching the MCP.

Experiments were carried out at the Surface and Interface Spectroscopy (SIS) beamline [180] at the Swiss Light Source (SLS) at the Paul Scherrer Institute (PSI), at the  $1^3$  beamline at Bessy II in Berlin, at the I05 beamline [181] at Diamond Light Source Ltd. (DLS) near Oxford, UK and at the MAESTRO beamline at the Advanced Light Source (ALS) in the Berkeley labs, US (see Tab. 3.2).

## Hemispherical analyzer

State-of-the-art, commercially available hemispherical energy analyzers (Scienta R4000) were used in all our experiments. They consist of two metallic hemispheres with a voltage  $V_H$  applied between them. An incoming electron beam is focused by electrostatic lenses and follows a trajectory according to their kinetic energy. High energetic electrons hit the outer hemisphere with radius  $r_2$ , while the low energetic electrons are captured by the inner one with radius  $r_1$ . Tuning the applied voltage selects the desired electron energy (Fig. 3.10). Since the resolution is proportional to the electron energy, improvement is reached by decelerating the electrons with a retarding potential  $V_R$  before entering the hemispheres. The pass energy  $E_p$  at which the electrons are transmitted by the analyzer is given by

$$E_p = E_{\text{kin}} - eV_R - \Phi_A = eV_H (r_2/r_1 - r_1/r_2)^{-1}, \quad (3.19)$$

where  $\Phi_A$  is the work function of the analyzer. At the other end of the analyzer, the electrons are multiplied by a micro-channel plate (MCP) and finally detected by a CCD chip as light spots on a fluorescent screen. Given a slit width  $w$ , the energy resolution is

$$\Delta E = \frac{wE_p}{r_1 + r_2}. \quad (3.20)$$

Sweeping  $E_{\text{kin}}$  requires changing either the pass energy or the retarding potential. Usually, however,  $E_p$  is kept constant and  $V_R$  is swept to preserve a constant energy resolution.

## Normalization

Before the data analysis can start, one has to take care of a proper normalization of the measured signal. We performed this reference measurements on polycrystalline copper or on a gold coated surface. First of all, the efficiency of the detector channels varies strongly and depends on the photon energy. The integrated intensities are a good measure for the relative detector efficiencies, thus providing the possibility to normalize each channel  $n$ :

$$I_{\text{norm.}}(n, E_B) = \frac{I_{\text{meas.}}(n, E_B)}{\sum_{E_B} I_{\text{Au}}(n, E_B)} \quad (3.21)$$

To display spectra on a binding energy scale we can fit the end of the spectrum by a Fermi-Dirac (FD) distribution in the reference measurement and determine the Fermi energy in each channel. We then define the energy scale:

$$\omega \equiv -E_B = E_{\text{kin}} - E_F \quad (3.22)$$

Note that with this procedure (Fig. 3.11), this scale only holds for the sample when it is in thermodynamical and electrical equilibrium with the reference material. In an ARPES experiment, the electrons leave the sample with a kinetic energy  $h\nu - E_B - \Phi$ . When they penetrate the detector material with workfunction  $\Phi_A$ , they gain the energy difference. Thus, yielding a sample independent energy scale with  $E_{\text{kin}} = h\nu - E_B - \Phi + (\Phi - \Phi_A) = h\nu - E_B - \Phi_A = E_p - eV_R - \Phi_A$  (Fig. 3.12).

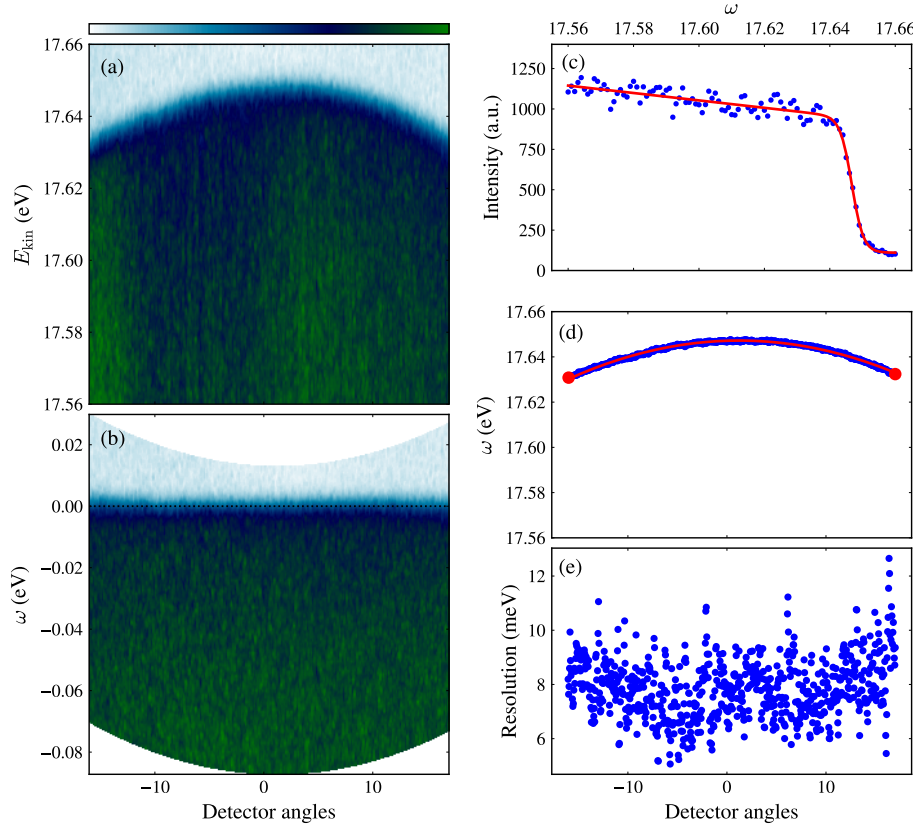


**Fig. 3.11** ARPES measurements taken on polycrystalline gold. (a) Kinetic energy vs detector angles. (b) Normalized intensities on the binding energy scale. (c) EDC fitted with a Fermi Dirac function on a slope. (d) Extracted  $E_F$  fitted with a quadratic function and (e) energy resolution for all detector angles.

### 3.2.6 Background and resolution

Both extrinsic and intrinsic effects are responsible for broadening of the ARPES signal. When an optically excited photoelectron travels to the surface, they may suffer additional inelastic collisions and form an intrinsic background tail. Theoretical treatment of secondary electrons is complicated and cumbersome. To make progress, experimentalists usually chose the background to be constant or more elaborate, i.e. a Shirley background [182]. A straight forward method is subtracting for every energy step the minimum intensity for all detector channels (see Fig. 3.13). With a photon energy of  $h\nu = 40$  eV and an angular resolution of  $1.5^\circ$  we resolve  $\sim 1/100$  of a BZ with a typical lattice parameter  $a \sim 3.9$  Å. Thus the momentum resolution is usually not the limiting factor. Extrinsic effects are given for example by the instrumental resolution. The energy resolution of standard hemispherical analyzers improved over time down to  $5 - 10$  meV [180, 181]. An estimation of the instrumental energy resolution  $\Delta\omega$  can be

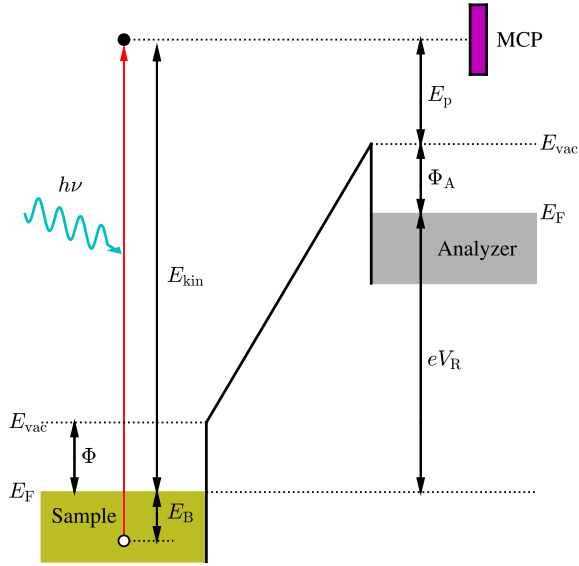


**Fig. 3.12** Energy relations of the photoelectron leaving the sample and reaching the analyzer on a retarding potential  $V_R$ .

estimated by fitting the Fermi-Dirac distribution and use  $T_{\text{fit}} = \sqrt{T_{\text{sample}}^2 + (\Delta\omega/4k_B)^2}$ . Another determination of  $\Delta\omega$  can be obtained by extrapolation of fitted  $T_{\text{fit}}$  for multiple sample temperatures through zero (see Fig. 3.14 (a)). A more realistic description of the measured ARPES intensity  $I(\mathbf{k}, \omega)$  is given by [183, 184]

$$I(\mathbf{k}, \omega) = [I_0(\mathbf{k}, \omega) + B] \otimes \mathcal{R}(\Delta\omega), \quad (3.23)$$

where  $I_0(\mathbf{k}, \omega)$  is given by eq. (3.12) and  $\mathcal{R}(\Delta\omega)$  is the resolution function, usually described as a Gaussian. Note that the intrinsic signal  $I_0(\mathbf{k}, \omega)$  is proportional to the Fermi-Dirac distribution, the spectral function and the matrix element. Experimentally this is demonstrated in Fig. 3.14. Panel (b) shows a normalized ARPES spectrum of polycrystalline gold. In panel (c) the EDCs are averaged and fitted with a Gaussian convoluted with a Fermi-Dirac function on a sloped background. The temperature is fixated and the FWHM of the Gaussian in the convolution is a fit parameter that measures the instrumental energy resolution. In this example FWHM =  $\Delta\omega = 7.4 \pm 1.5$  meV.

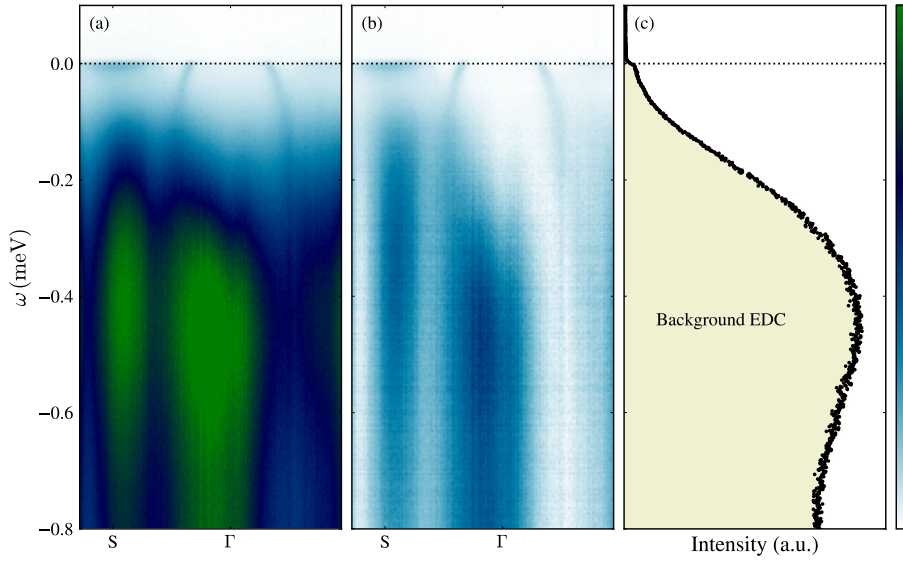


**Fig. 3.13** ARPES background subtraction. For every energy step of the original ARPES spectra (a), the minimum intensity is subtracted for all angular channels (c). (b) Background subtracted data.

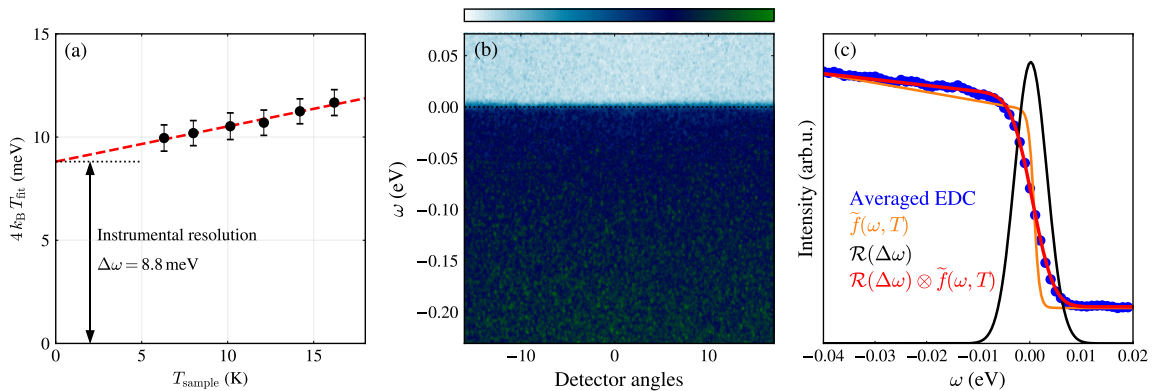


**Fig. 3.14** Instrumental resolution extraction. From the ARPES data of polycrystalline gold (a), the EDCs are averaged (blue) and fitted (b). The fit function (red) is a convolution of a Fermi-Dirac function on a sloped background (orange) and a resolution function (black). (c) Determination of the instrumental resolution by extracting  $T_{\text{fit}}$  from a Fermi-Dirac fit for different sample temperatures. The extrapolation through zero gives a good estimate for  $\Delta\omega \approx 4 k_B T_{\text{fit}}$ .

# Chapter 4

## Orbital-selective Fermi liquid $\text{Ca}_{1.8}\text{Sr}_{0.2}\text{RuO}_4$

### 4.1 Introduction

Multi-orbital strongly correlated systems together with Hund's coupling  $J_{\text{H}}$  generate conceptually important physics [20]. Regarding the ruthenates, the OSMT is a controversial concept, initially proposed by Anisimov *et al.* in order to explain the coexistence of a spin  $S = 1/2$  moment and metallicity in  $\text{Ca}_{1.5}\text{Sr}_{0.5}\text{RuO}_4$  [35]. In this scenario, the four  $t_{2g}$  electrons occupy the ( $d_{\gamma z}$ ,  $d_{xy}$ )-orbitals in a (3, 1)-configuration, where the  $d_{xy}$  electrons undergo the Mott transition and the  $d_{\gamma z}$  states remain itinerant. From several DMFT studies, it has been suggested that orbital-selective behaviour is triggered by a sufficiently high  $J_{\text{H}}$  [20, 22, 35, 111]. In this fashion, orbital fluctuations are suppressed and the  $t_{2g}$ -orbitals localize depending on their individual filling. Beside the OSMT,  $J_{\text{H}}$  and proximity to a vHs are expected to renormalize band masses in an orbitally differentiated fashion [23, 143]. Such strongly correlated *Hund's metals* are represented by  $\text{Sr}_2\text{RuO}_4$  and iron-based superconductors [143, 144, 148, 149].

$\text{Ca}_{1.8}\text{Sr}_{0.2}\text{RuO}_4$  is in close proximity to the Mott-Hubbard transition [75, 185]. Two ARPES experiments investigated the low-energy band structure of  $\text{Ca}_{1.8}\text{Sr}_{0.2}\text{RuO}_4$ , but with contradicting results [97, 98]. One study found limited resemblance to the electronic structure of the parent compound  $\text{Sr}_2\text{RuO}_4$  [97]. In Fig. 4.1 (a) ARPES data along  $\Gamma - \text{X}$  reveal spectral features close to the Fermi level. (b) and (e) are second derivatives along  $\Gamma - \text{X}$  and  $\Gamma - \text{M}$  respectively. (c, d) display MDCs, from which a linear dispersion is extracted. In (f) the FS is shown in a schematic fashion. Following the band labeling convention of  $\text{Sr}_2\text{RuO}_4$ , the ARPES study finds states

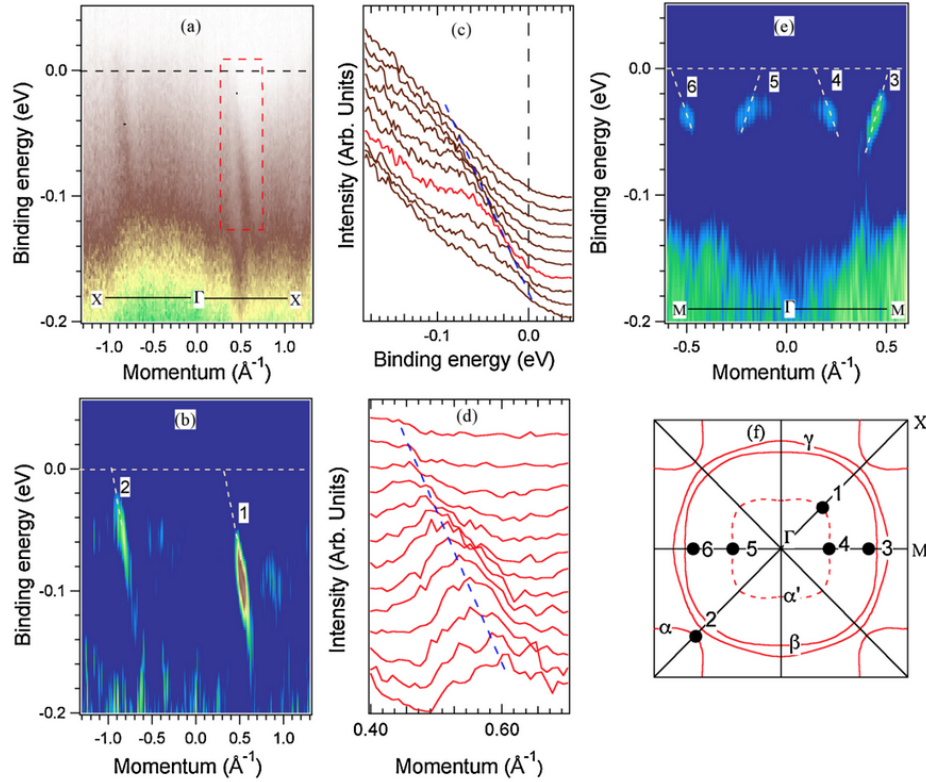


**Fig. 4.1** ARPES data on  $\text{Ca}_{1.8}\text{Sr}_{0.2}\text{RuO}_4$  from Neupane *et al.* (a) Intensity map along  $\Gamma - \text{X}$ . (b) and (e) are second derivatives along  $\Gamma - \text{X}$  and  $\Gamma - \text{M}$  respectively. (c, d) show MDCs where the maxima are fitted with a linear function. (f) schematic FS with Fermi level crossings of the data as indicated by enumeration.

corresponding to the  $\alpha$ - and  $\beta$ -pockets. However, many FS crossings are missing. The authors attribute the complete absence of the  $\gamma$ -band in their data to an OSMT with insulating  $d_{xy}$ -orbitals.

The other study do not only find the missing  $\gamma$ -band but also the orthorhombically folded pockets. In Fig. 4.2 ARPES spectra are presented. Panel 1 shows a cut through the zone diagonal (corresponding to Fig. 4.1 (e)), where three bands including their replica are found. As they move along the FS, the last cut in panel 7 reveals a heavy band that decays with increasing temperature. The authors suspect an association to a vHs close to the Fermi level, similar to the  $\gamma$ -band in  $\text{Sr}_2\text{RuO}_4$  [186]. Indeed, in recent strain-controlled experiments on ruthenates the deviation from FL behaviour is clearly demonstrated by tuning the system through the vHs [86, 187].

Heat capacity measurements on  $\text{Ca}_2\text{RuO}_4$  indicate the existence of heavy fermions with a Sommerfeld constant  $\gamma \approx 180 \text{ mJ}/(\text{mol-Ru K}^2)$  [75, 188]. (ab)-resistivity curves display a nFL  $T^{1.4}$ -dependence above  $T_{\text{FL}} \sim 1 \text{ K}$ . Reconciliation of the low-energy band

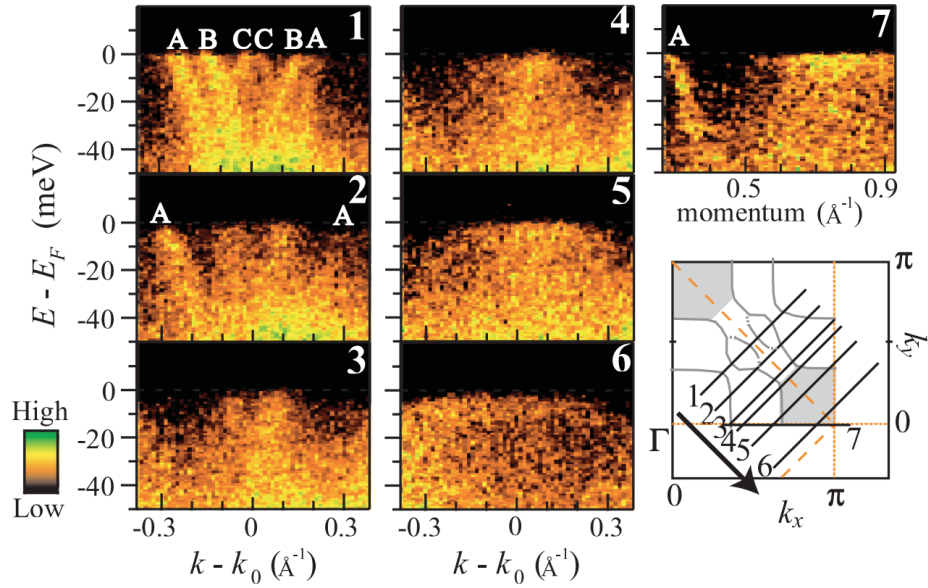


**Fig. 4.2** ARPES spectra of  $\text{Ca}_{1.8}\text{Sr}_{0.2}\text{RuO}_4$  from ref. [98]. (1) Three bands are found along the zone diagonal, labelled A, B & C. (2-7) are spectral cuts as indicated in the FS sketch (inset right bottom corner).

structure and the nFL-resistivity has still yet to be reached. In the following, new ARPES data of  $\text{Ca}_{1.8}\text{Sr}_{0.2}\text{RuO}_4$  are presented. Evidence will be shown that strongly suggests to dismiss the OSMT scenario, in favor of the Hund's metal picture. Additional self-energy analysis and DMFT calculations highlight clear FL behaviour of the  $\alpha$ -band and a FL-breakdown of the  $\gamma$ -band.

## 4.2 Methods

### 4.2.1 Experimental

ARPES data have been taken at the SIS, I05 and  $1^3$  beamlines. Samples were glued and electrically grounded on sample holders by using the E4110 silver epoxy from EPO-TEK, cured at 100°C over two hours. In the ARPES experiment, the samples were cleaved in UHV conditions at base temperature (6 K at SIS and I05, 1.3 K at  $1^3$ ) by the top-post method.

### 4.2.2 Band structure calculations

#### Density functional theory

Our DFT calculations were performed using the projector augmented wave method within the VASP framework in the generalized gradient approximation [189–193]. We used experimental lattice constants ( $a = 5.33 \text{ \AA}$ ,  $b = 5.32 \text{ \AA}$  and  $c = 12.41 \text{ \AA}$ ) and sampled on a  $12 \times 10 \times 4$  Monkhorst-Pack  $k$ -point mesh grid (cutoff energy 400 eV). Additional spin-orbit coupling effects are included in a self-consistent fashion.

#### Dynamical mean field theory

We calculate the electronic structure within DFT+DMFT using the full potential implementation [194] and the TRIQS library [195, 196]. In the DFT part of the computation, the Wien2k [197] package was used. The local-density approximation (LDA) is used for the exchange-correlation functional. For projectors on the correlated  $t_{2g}$  orbital in DFT+DMFT, Wannierlike  $t_{2g}$  orbitals are constructed out of Kohn–Sham bands within the energy window  $(2, 1)$  eV with respect to the Fermi energy. We use the full rotationally invariant Kanamori interaction in order to ensure a correct description of atomic multiplets [20]. To solve the DMFT quantum impurity problem, we used the strong coupling continuous-time Monte Carlo impurity solver [198] as implemented in the TRIQS library [199]. In the U and J parameters of the Kanamori interaction, we used  $U = 2.3 \text{ eV}$  and  $J_H = 0.4 \text{ eV}$ , which successfully explains the correlated phenomena of other ruthenates such as  $\text{Sr}_2\text{RuO}_4$  and  $\text{ARuO}_3$  ( $\text{A} = \{\text{Ca}, \text{Sr}\}$ ) within the DFT+DMFT framework [143, 200].

## 4.3 Results

### 4.3.1 Low-energy band structure

Let's start with the results of the band structure fit. The TBA FS with initial parameters from  $\text{Sr}_2\text{RuO}_4$  [152] are displayed in Fig. 4.3. (a–c) show the  $\alpha$ -,  $\beta$ - and  $\gamma$ -pocket, respectively. In the convergence limit, a fitness  $\xi = 5.5 \text{ meV}$  – comparable to the energy resolution ( $\sim 7.9 \text{ meV}$ ) – is reached (see Fig. 4.4). The resulting FS sheets are shown in Fig. 4.5, plotted in an unfolded fashion for better comparison to the  $\text{Sr}_2\text{RuO}_4$  FS. The  $\alpha$ - and  $\beta$ -band are topologically unchanged, while the  $\gamma$ -sheet switches from electron-like,  $\Gamma$ -centered in  $\text{Sr}_2\text{RuO}_4$  to hole like zone corner-centered in  $\text{Ca}_{1.8}\text{Sr}_{0.2}\text{RuO}_4$ . This change of character has been also reported in  $\text{Ca}_{1.5}\text{Sr}_{0.5}\text{RuO}_4$  [100]. Furthermore a

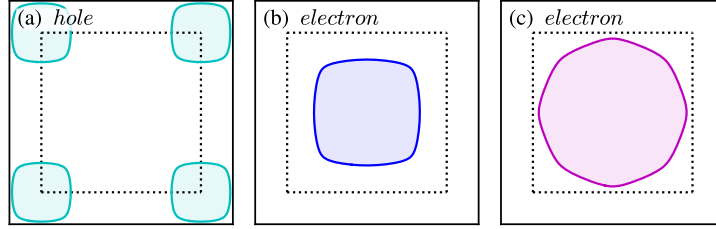


**Fig. 4.3** TBA model of the FS of  $\text{Sr}_2\text{RuO}_4$ , according to ref. [152]. (a) hole-like  $\alpha$ -pocket, (b) electron-like  $\beta$ -band and (c) electron-like  $\gamma$ -sheet. Dotted lines indicate the BZ boundary.

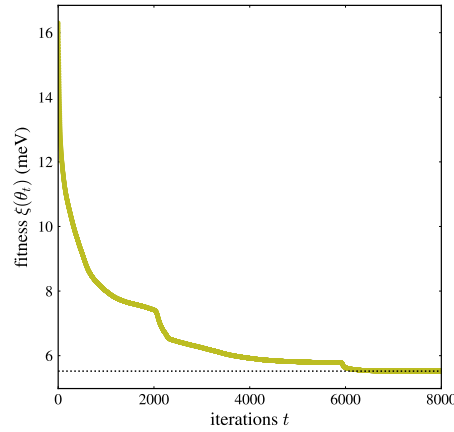


**Fig. 4.4** Tight binding fit. Optimized TBA parameters have been found for the  $\text{Ca}_{1.8}\text{Sr}_{0.2}\text{RuO}_4$  band structure by minimizing the fitness  $\xi$  iteratively.

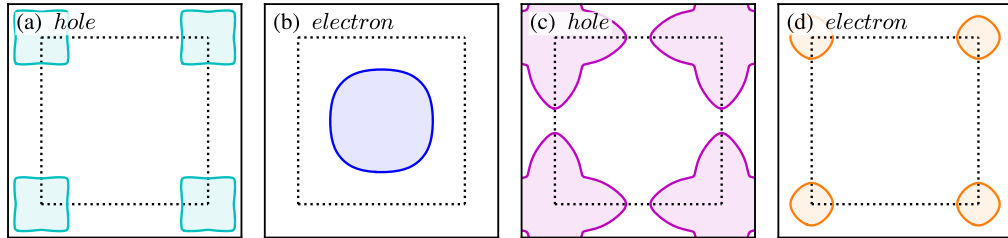


**Fig. 4.5** TBA FS of  $\text{Ca}_{1.8}\text{Sr}_{0.2}\text{RuO}_4$  after fit convergence. (a) hole-like  $\alpha$ -pocket, (b) electron-like  $\beta$ -band, (c) hole-like  $\gamma$ -sheet and a new electron-pocket around the zone corner, labeled  $\delta$  in (d). Dotted lines indicate the BZ boundary.

small electron pocket emerges that is labeled  $\delta$ . The folded FS is plotted in Fig. 4.6 (a). Dotted lines represent the tetragonal BZ and the thick black boundary indicate the orthorhombic BZ. The FS sheets (from Fig. 4.5) are plotted 45 degrees rotated and the folded replica are drawn with dashed lines. In Fig. 4.6 (b-d) ARPES data of the low-energy band structure of  $\text{Ca}_{1.8}\text{Sr}_{0.2}\text{RuO}_4$  are shown. Here, 22 eV circularly

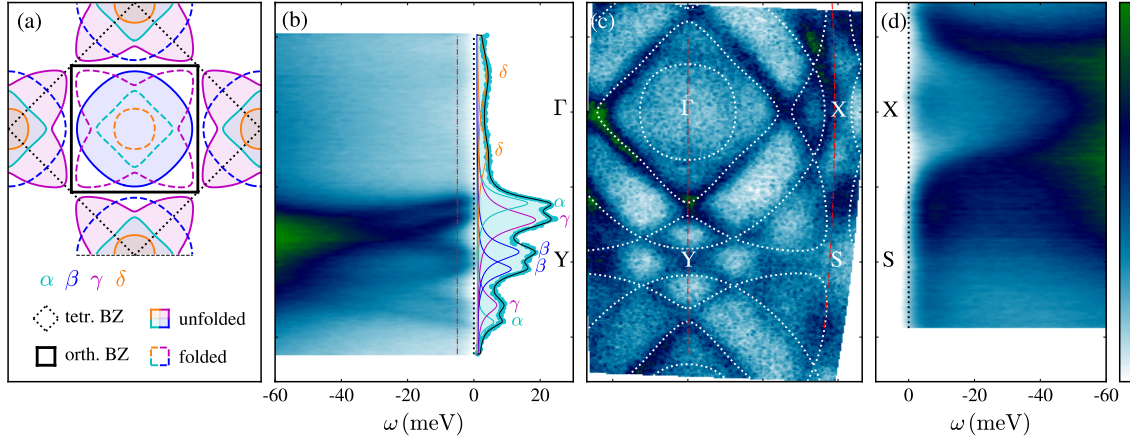


**Fig. 4.6** Low-energy band structure of  $\text{Ca}_2\text{RuO}_4$ . (a) TBA FS showing folded (dashed) and unfolded (solid) contours of the  $\alpha$ ,  $\beta$ ,  $\gamma$  and  $\delta$  sheets. (b) ARPES cut along  $\Gamma$ –Y recorded with 22 eV circularly polarised light ( $\text{C}^+$ ). Cyan circles is an MDC at fixed binding energy  $5 \pm 1$  meV, indicated by the red dashed line. The MDC is fitted by eight Lorentzians (total fit in black), displayed colour coded to the corresponding FS sheets in (a). (c) Experimental FS map ( $\pm 2$  meV integrated) with the TBA model indicated by white dots. The trajectories of ARPES spectra shown (b) and (d) are indicated by dashed red lines. (d) ARPES spectrum along the zone boundary X–S showing flat bands near the Fermi level.

polarised photons have been used at the i05 beamline. The TBA model is laid over the FS data in Fig. 4.6 (c) with high congruence. High statistics spectral cuts are indicated by the dashed red line and showed in Fig. 4.6 (b, d). In Fig. 4.6 (b), an MDC is displayed as an inset at 5 meV binding energy, integrated over  $\pm 1$  meV (indicated by the red dashed line). The MDC is fitted with eight Lorentzians (total in black) and colored/labeled corresponding to the sketch in Fig. 4.6 (a). In the FS and in the MDC, the newly found  $\delta$ -pocket is visible but rather weak. Further evidence is documented in Fig. 4.7, where data have been taken at the SIS beamline with different detector-slit geometry, integrated in a larger range (0 – 10 meV binding energy). In Fig. 4.7 (a, c) MDCs are shown, indicated by the red dashed line in (b). The resonances are fitted by multiple Lorentzians and demonstrate a significant amplitude of the  $\delta$ -band signal. The more metallic  $\text{Ca}_{1.7}\text{Sr}_{0.3}\text{RuO}_4$  displays a similar electronic structure, shown in the Appendix A.

### 4.3.2 Orbital characters

Next we investigate the light polarisation dependence and orbital characters from the TBA and DMFT results. In Fig. 4.8 (a–c) ARPES spectra along  $\Gamma$  – S are presented. The data set was recorded at the 1<sup>3</sup> beamline at base temperature 1.3 K with 40 eV

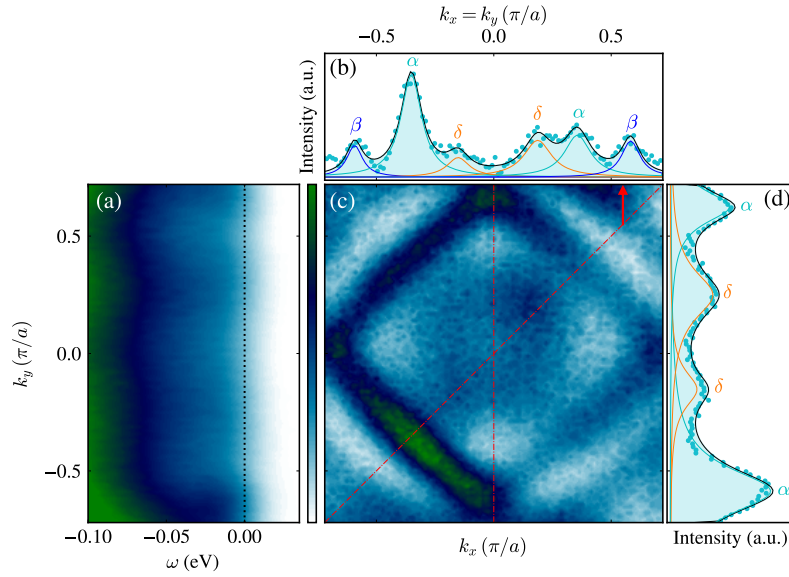


**Fig. 4.7** ARPES data from the SIS beamline, recorded with 25 eV circularly polarised photons. (b) FS map, integrated from  $E_F$  to  $E_F - 10 \text{ meV}$ , reveal the  $\alpha$ ,  $\beta$  and  $\delta$  sheets. (a,c) display MDCs along the zone diagonal  $k_x = k_y$  and  $(0, k_y)$  directions respectively. Solid cyan, blue and orange lines are Lorentzian fits to the  $\alpha$ ,  $\beta$ ,  $\delta$  contributions, and their sum respectively in black.

photon energy and light polarisation as indicated. MDCs close to the Fermi level (indicated with red dashed lines) are shown as cyan circles in the insets.  $C^+$ - and  $\bar{\pi}$ -polarisation (Fig. 4.8 (a,b)) both probe clear  $\alpha$ -band QP dispersions. Switching polarisation to  $\bar{\sigma}$  (Fig. 4.8 (c)), the  $\alpha$ -band vanishes. The flat  $\gamma$ -band is located around at the S-point and is visible with  $C^+$ - and  $\bar{\sigma}$ -polarisation, while in the  $\bar{\pi}$ -channel spectral weight is suppressed.

The incident light and center of our analyser slit, define a mirror plane to which the electromagnetic field has odd (even) parity for  $\bar{\sigma}$  ( $\bar{\pi}$ ) polarisation (see Fig. 4.8 (d,h)). For final states with even character, selection rules [120] dictate that an odd (even) band character is suppressed in the  $\bar{\pi}$  ( $\bar{\sigma}$ ) polarisation channel. The  $\alpha$ -band being suppressed completely in the  $\bar{\sigma}$ -channel therefore has even character. Assuming approximately tetragonal crystal structure, ( $d_{xy}$ ,  $d_{xz}$ , and  $d_{yz}$ ) have (odd, even, and odd) character along the  $a$ -axis. As a result the  $\alpha$ -band along the Ru-O bond direction has pure  $d_{xz}$  character. The  $\gamma$ -band is placed further away from the mirror-plane due to the perpendicular electron analyser-slit geometry. Hence, less strict selection rules are expected. Thus, experimental polarisation results suggest a considerable  $d_{xy}$  character of the  $\gamma$ -band. As one might expect a similar relation of electronic bands to orbital characters in  $\text{Sr}_2\text{RuO}_4$ , the assignments outlined above in  $\text{Ca}_{1.8}\text{Sr}_{0.2}\text{RuO}_4$  correspond

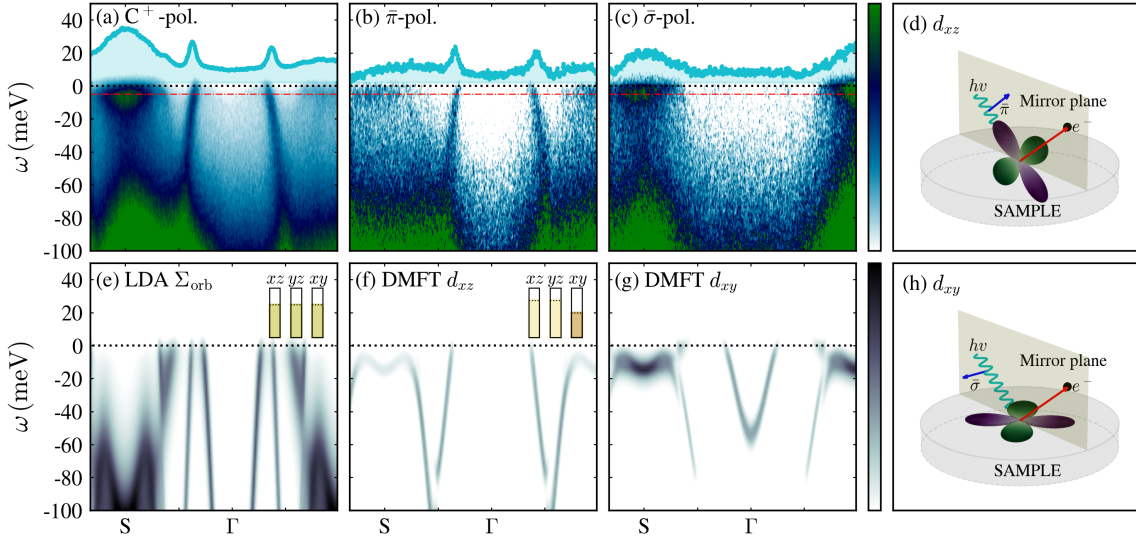


**Fig. 4.8** Heavy fermion quasiparticles and orbital band character. (a–c) ARPES spectra along the zone diagonal ( $\Gamma$ –S) using 40 eV circularly-,  $\bar{\sigma}$ -, and  $\bar{\pi}$ -polarisation, respectively. Cyan points are MDCs near  $E_F$  (dashed turquoise lines). (d, h) Schematics for photoemission selection rules for  $d_{xy}$  and  $d_{xz}$  orbitals. (e) DFT band structure along  $\Gamma$ –S. (f,g) DMFT calculation of the spectral function orbitally resolved. To mimic the experimental data, the DFT and DMFT calculations are plotted in spectral representation, truncated by the Fermi-Dirac distribution ( $T_{\text{DMFT}} = 39$  K), and a constant inverse lifetime of 20 meV is used. Relative orbital fillings are indicated by the insets in (e, f).

essentially to the orbital band characters in the parent compound [201, 202]. From orbitally-resolved DMFT calculations (see Fig. 4.8 (f, g)), we observe the  $\gamma$ -band around the S-point with  $d_{xy}$ -character and a weak  $d_{xz}$ -contribution. Orbital mixing in the DMFT stems from hybridization due to tilting of the  $\text{RuO}_6$ -octahedra. The  $\alpha$ -band has pure  $d_{xz}$ -character and is not seen in the  $d_{xy}$ -channel. A discrepancy to the experiment is the  $\delta$ -band that is absent for this particular data set. As the signal intensity of the  $\delta$ -band appears to be prone to matrix element effects (compare Fig. 4.6 (c) to Fig. 4.7 (b)), further suppression in Fig. 4.8 (a, c) may have the same origin. Lastly, the FS of the TBA model is shown in Fig. 4.9. The bandstructure is projected onto the  $t_{2g}$  basis. The orbital weight is plotted colour-coded in an intensity map. Orange corresponding to  $d_{xy}$ - and purple to  $d_{\gamma z}$ -weight. Along  $\Gamma$  – S, the  $\delta$ - and  $\gamma$ -pocket have  $d_{xy}$ -character and the  $\alpha$ -band has out-of-plane orbital character as found in DMFT. Along  $\Gamma$  – X, the orbital characters are mixed by spin-orbit coupling [150].

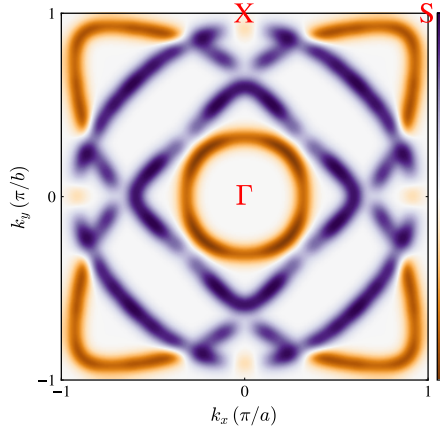


**Fig. 4.9** TBA model of the FS. Orange side of the colorscale is the  $d_{xy}$ -orbital weight, purple corresponds to the  $d_{\gamma z}$ -orbital weight.

## 4.4 Discussion

### 4.4.1 Band filling

In the previous ARPES study in favour of the OSMT-scenario, the apparently missing  $\gamma$ -sheet creates a deficiency in the band filling [97]. This can be experimentally determined from the area in  $\mathbf{k}$ -space that is enclosed by the individual FS pockets with respect to the area of the full BZ. As our new data identifies the missing band, the total FS area and thus the band filling can be directly measured from the TBA fit. Four electrons per Ru site occupy  $t_{2g}$ -orbitals corresponds to a band filling of  $4/(2 \times 3) \approx 0.67$  (factor two from spin-degeneracy). Adding up the relative FS areas, as listed in Tab. 4.1, we obtain 1.92. This yields a band filling of  $1.92/3 = 0.64$ , that is essentially the same value reported in metallic  $\text{Sr}_2\text{RuO}_4$  and  $\text{Ca}_{1.5}\text{Sr}_{0.5}\text{RuO}_4$  [100, 152]. Thus, from a band filling perspective I rule out an OSMP.

FS sheet	$\text{Sr}_2\text{RuO}_4$	$\text{Ca}_{1.5}\text{Sr}_{0.5}\text{RuO}_4$	$\text{Ca}_{1.8}\text{Sr}_{0.2}\text{RuO}_4$
$\alpha$	0.86/0.88	0.86	0.90
$\beta$	0.41/0.40	0.38	0.32
$\gamma$	0.64/0.66	0.68	0.65
$\delta$	-	-	0.05
total	1.91/1.91	1.92	1.92
Ref.	[100]/[152]	[100]	This work

**Table 4.1** FS area with respect to the Brillouin zone area for different compositions of  $\text{Ca}_{2-x}\text{Sr}_x\text{RuO}_4$ .

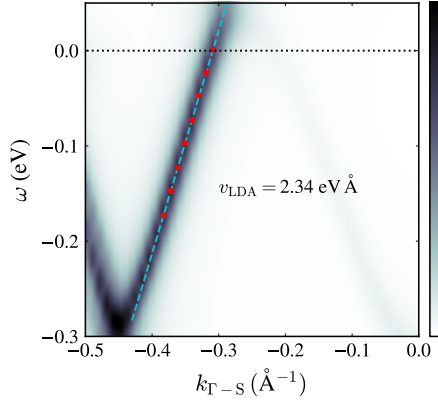


**Fig. 4.10** DFT spectral function in the LDA of  $\text{Ca}_{1.8}\text{Sr}_{0.2}\text{RuO}_4$  along  $\Gamma - \text{S}$  including a constant thermal broadening  $\Im\Sigma = 20 \text{ meV}$ , represented in a linear grey scale, starting at zero. The bare band Fermi velocity is extracted by a linear fit (cyan dashed line) close to the Fermi level.

#### 4.4.2 Self-energy analysis

From resistivity experiments it is clear that  $\text{Ca}_{1.8}\text{Sr}_{0.2}\text{RuO}_4$  exhibits nFL behaviour above  $T_{\text{FL}} \sim 1 \text{ K}$ . This is expected to be reflected in the self-energy  $\Sigma(\mathbf{k}, \omega)$  as it should deviate from the FL-form given in eq. (2.24). From our ARPES data,  $\Sigma(\mathbf{k}, \omega)$  can be extracted in a following self-energy analysis.

The imaginary part can be directly obtained from fitting an MDC with a Lorentzian, given by eq. (3.16), and read off the HWHM  $\Delta k_{\text{HWHM}}$ :

$$\Delta k_{\text{HWHM}} \times v_F^b = \Im\Sigma(\omega), \quad (4.1)$$

where  $v_F^b$  is obtained from the DFT calculation. Fig. 4.10 shows a linear fit of the  $\alpha$ -band near  $E_F$  and results as  $v_F^b = v_{\text{LDA}} = 2.34 \text{ eV \AA}$ . The spectral function is obtained by eq. (2.14) with the DFT eigenenergies and a constant thermal broadening  $\Im\Sigma = 20 \text{ meV}$ .

From the ARPES spectra at (1.3, 10, 20 & 30) K shown in Fig. 4.11 (a-d), MDCs from the Fermi level down to  $\omega = 100 \text{ meV}$  were extracted and fitted by Lorentzians. Fig. 4.11 (e-h) exemplify this procedure at representative  $\omega = (0, -50, -100) \text{ meV}$ , where a fitted linear background has been used [203]. In Fig. 4.11 (i-l), the HWHM are plotted as a function of  $\omega$  and fitted with a quadratic function. Analysis of  $\Delta k_{\text{HWHM}}(\omega)$  at  $T = 30 \text{ K}$  yields  $\Gamma(\omega) = \Gamma_0 + \eta\omega^2$  with  $\Gamma_0 = 0.020(2) \text{ \AA}^{-1}$  and  $\eta = 10.6(6) \text{ \AA}^{-1}\text{eV}^{-2}$  being constants. By using eq. (4.1), the imaginary part of the self-energy is obtained. The real part of  $\Sigma(\omega)$  can be extracted more directly as a result of the deviation of the QP dispersion  $\varepsilon_{\mathbf{k}}^{\text{exp}}$  from the bare band  $\varepsilon_{\mathbf{k}}^b$ .

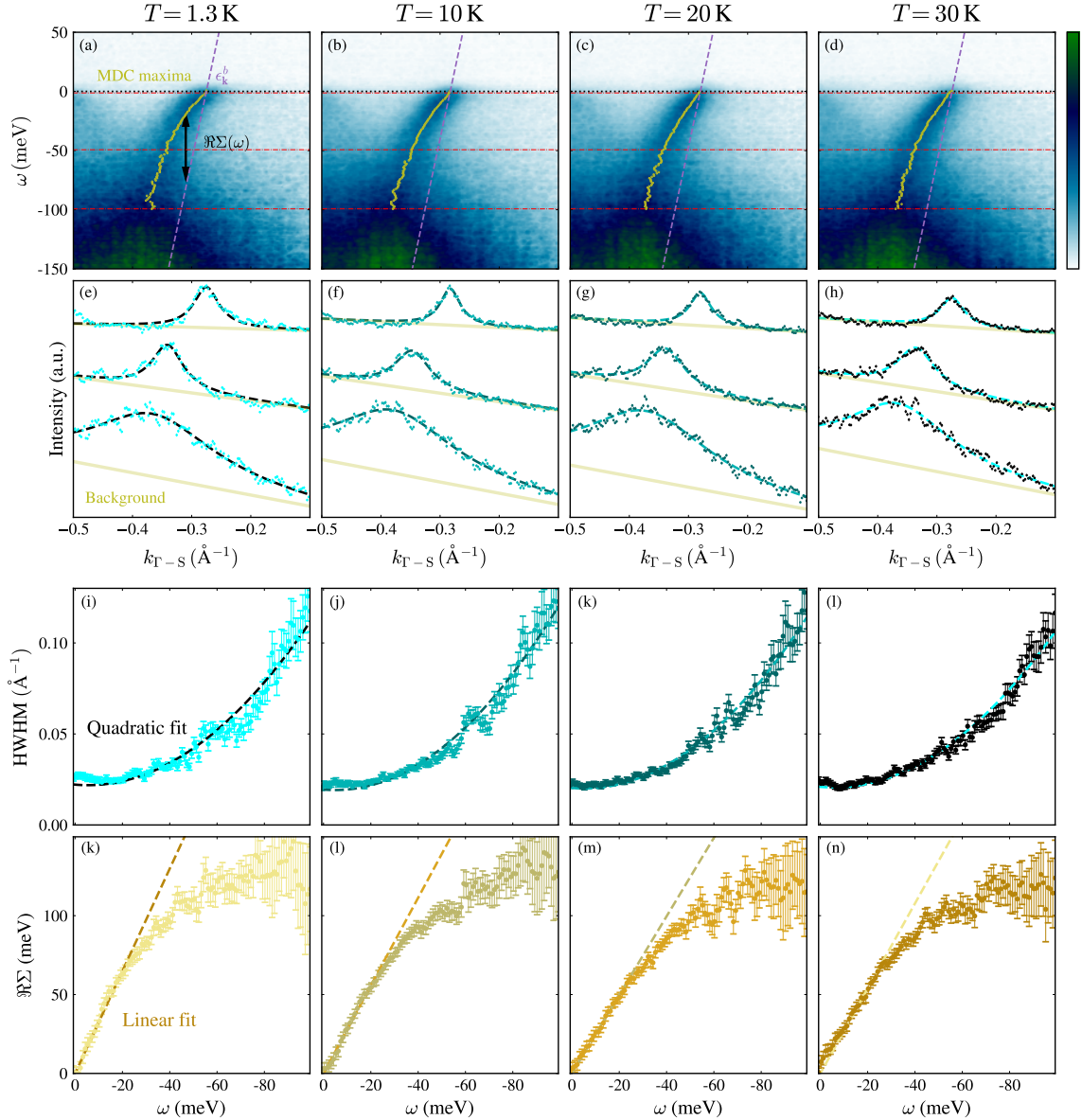


**Fig. 4.11** (a–d) ARPES spectra along the zone diagonal, displaying the dispersion of the  $\alpha$ -band. The purple dashed line is the linearised LDA band structure and  $\Re\Sigma(\omega)$  is drawn in red. Beige points are MDC maxima, extracted from Lorentzian fits with a linear background shown in (e–h). Binding energies of the MDCs are marked by the cyan dashed line in the top row. (i–l) are the HWHM of the Lorentzians as a function of  $\omega$  with a quadratic fit. (k–n) are plots of  $\Re\Sigma(\omega)$  versus  $\omega$ , fitted by a linear function near  $E_F$ .

$$\Re\Sigma(\omega) = \varepsilon_{\mathbf{k}}^{\text{exp}} - \varepsilon_{\mathbf{k}}^b \quad (4.2)$$

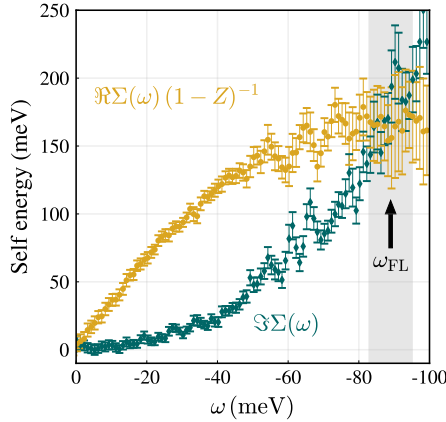


**Fig. 4.12** Self-energy  $\Sigma$  plotted as  $\Im\Sigma$  (green) and  $\Re\Sigma/(1 - Z)$  (yellow) versus binding energy  $\omega$  for the  $\alpha$ -band. The FL cut-off energy scale  $\omega_{\text{FL}}$  is indicated by the arrow.

at a given  $\omega$ . The experimental dispersion stems from the maxima of the fitted MDCs (see Fig. 4.11 (a–d)). By linearisation near  $k_F$ , the real part of the self-energy can be approximated as  $\Re\Sigma(\omega) = (1 - v_F^b/v_F)\omega$ . The quasiparticle residue  $Z$  is obtained by a linear fit of  $\Re\Sigma(\omega)$  (see Fig. 4.11 (k–n)) at the Fermi level and use eq. (2.18). For  $\alpha$ -band I obtain  $Z = 0.26(4)$ , consistent with the DMFT result  $Z_{\text{DMFT}}^{\gamma z} \simeq 0.23$ . To demonstrate that the  $\alpha$ -band hosts coherent FL QPs, the criterion eq. (2.26) is used to estimate a FL cut-off energy scale  $\omega_{\text{FL}}$ . In Fig. 4.12  $\Re\Sigma(\omega)/(1 - Z)$  and  $\Im\Sigma(\omega)$  are plotted against  $\omega$ , yielding  $\omega_{\text{FL}} \sim 90$  meV. From DMFT and the presented self-energy analysis, the  $\alpha$ -band behaves thus genuinely FL-like.

#### 4.4.3 Temperature dependence

As the  $\alpha$ -band with  $d_{\gamma z}$ -character does not contribute to the nFL behaviour, we turn next to the  $d_{xy}$ -orbital driven  $\gamma$ -band. Along the  $\Gamma - \text{X}$ -direction, spin-orbit coupling mixes orbital characters [150] (see also Fig. 4.9) and thus does not offer a discussion in an orbital-pure fashion. However, close to the zone corner, along  $\Gamma - \text{S}$ , the QP amplitudes of the free standing  $\gamma$ -pocket can be accessed by EDCs. Since the band is very flat, MDC self-energy analysis as described above is not feasible.

Fig. 4.13 (a–d) show background subtracted ARPES spectra along  $\Gamma - \text{S}$  at different temperatures as indicated. Qualitatively, a decay of spectral weight of the  $\gamma$ -band by increasing temperature is already recognizable. EDCs at the S-point reveal a small ratio of coherent QP peak to incoherent background (see Fig. 4.13 (e) for 1.3 K and 30 K). Detailed inspection of the  $\gamma$ -feature at the Fermi level is shown in Fig. 4.13 (f). When warming up the sample from 1.3 K to 30 K, the excitation amplitude reduces

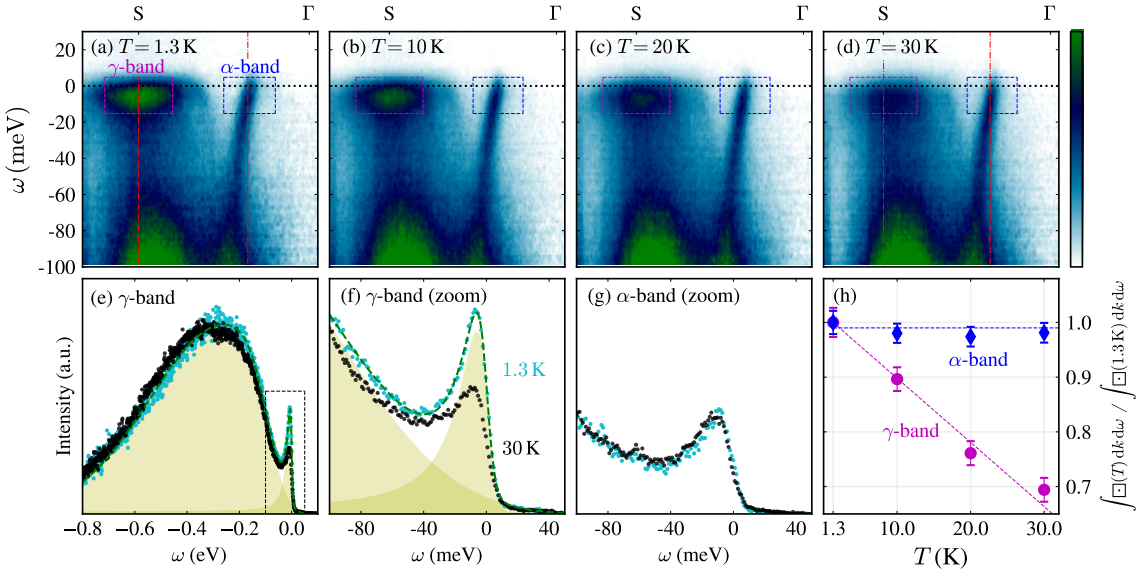


**Fig. 4.13** Temperature dependence of QP spectral weight. (a–d) ARPES spectra along S–Γ for temperatures as indicated. (e–g) Background subtracted (as in Ref. [204, 205]) EDCs of the  $\alpha$ - and  $\gamma$ -band at  $T = 1.3$  K (cyan) and  $30$  K (black) and fixed momenta indicated by dashed vertical lines in (a) and (d). (f) is a zoom near  $E_F$  of the EDC displayed in (e). The shaded area in (e) and (f) represents incoherent and coherent spectral weight modelled by fits to an exponentially modified Gaussian and a Lorentzian function truncated by the Fermi-Dirac distribution, respectively. The dashed line indicates the sum. (h) Normalized spectral weight, integrated within the magenta ( $\gamma$ ) and blue ( $\alpha$ ) boxes shown in (a–d), versus  $T$ .

almost by a factor of two. The EDCs of the  $\alpha$ -band, by contrast, shown in Fig. 4.13 (g) show a temperature-stable QP peak. This fact excludes the thermally broadened Fermi-Dirac distribution being the origin of the spectral weight suppression. In Fig. 4.13 (h) box-integrated ARPES intensity of the  $\alpha$ - and  $\gamma$ -band are normalized and displayed for  $T = (1.3, 10, 20, 30)$  K.

Integration boundaries in momentum-energy space are indicated by the coloured boxes in Fig. 4.13 (a–d)). As both the  $\alpha$ - and  $\gamma$ -bands are measured simultaneously, this band-selective decay is not a result of surface degradation. To emphasize this point, a modeling of the  $\alpha$ -band is showed in Fig. 4.14. In panel (a), the bare band is plotted with a self-energy, taken from the previous analysis and multiplied with the Fermi-Dirac function at zero temperature. In (b), the spectral function is convoluted with a spectral function of  $10$  meV width. From there the temperature is increased (c). (d, e) display MDCs and EDCs at the different temperatures. (f) are the values from box integration with boundaries equivalent to Fig. 4.13 (h). The simulation demonstrates how resolution effects in our ARPES data are quite limited and do not explain the

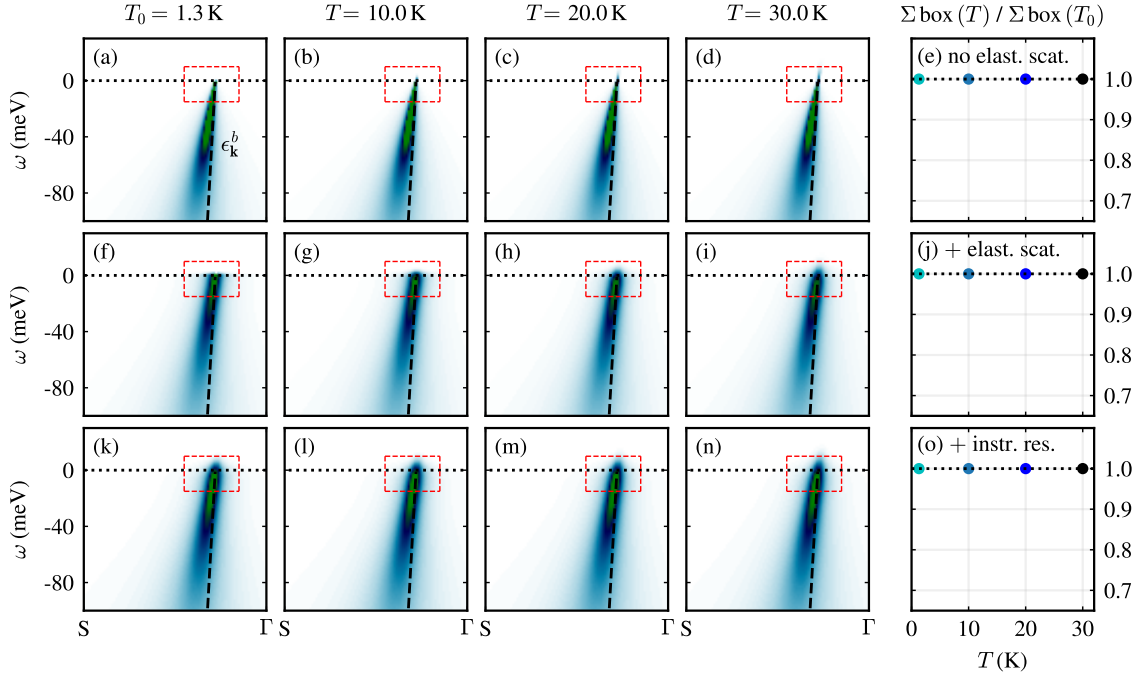


**Fig. 4.14** Resolution effects. The spectral function of the  $\alpha$ -band is shown for the experimental temperature range. (a–d) A FL self-energy is added with no elastic scattering contribution. The latter has been added in (f–i). In (k–n) the spectral function is convoluted with an instrumental resolution function (Gaussian) of width 10 meV. (e, j, o) are box integrations as indicated by the red dashed lines and normalized to the value at  $T_0 = 1.3$  K. The black dashed line is the bare band energy dispersion of the  $\alpha$ -band.

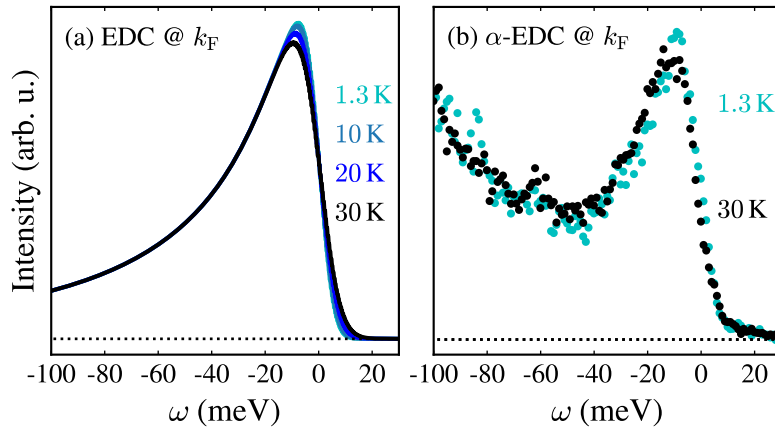


**Fig. 4.15** EDCs at  $k_F$  of the  $\alpha$ -band spectral function showed in Fig. 4.14 (k–n) at temperatures as indicated. Effects of temperature and instrumental resolution conserve the total spectral weight.

orbital	$n_{\text{LDA}}$	$n_{\text{DMFT}}$	$m_{\text{DMFT}}^*/m_b$	$m_{\text{exp}}^*/m_b$	
$d_{\gamma z}$	4/3	1.42	4.4/4.7	$\sim 4$ ( $\alpha$ )	FL
$d_{xy}$	4/3	1.18	19.2	$> 20$ ( $\gamma$ )	nFL

**Table 4.2** The first row with numerical values correspond to  $d_{\gamma z}$  and the second row to  $d_{xy}$ .  $n_{\text{LDA}}$  and  $n_{\text{DMFT}}$  are individual band fillings and renormalization factors are given in terms of effective masses  $m_{\text{DMFT}}^*$  and  $m_{\text{exp}}^*$ .  $d_{\gamma z}$ -driven orbitals are found to be FL while the  $d_{xy}$  electrons display nFL behaviour.

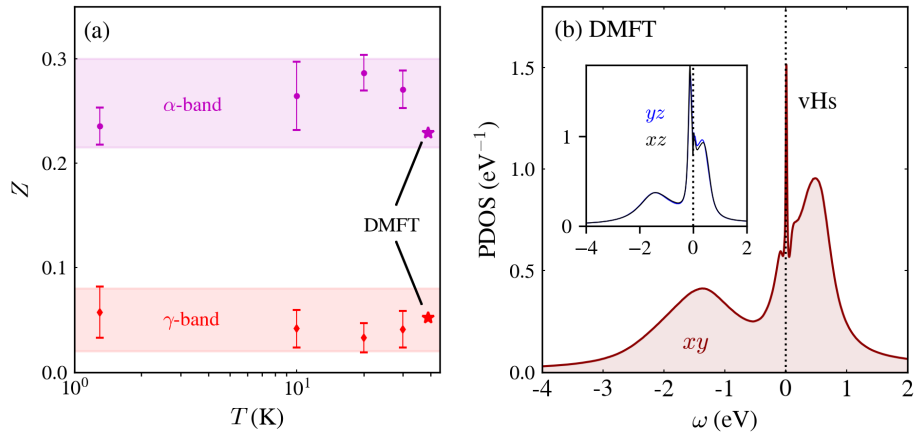


**Fig. 4.16** (a)  $Z$  versus  $T$  in semilog scale. To obtain  $Z$  for the  $\alpha$ -band, self-energy analysis was used. In case of the  $\gamma$ -band, the ratio of coherent QP peak to incoherent weight was determined. DMFT data points ( $T_{\text{DMFT}} = 39$  K) are plotted as stars. (b) PDOS of the  $d_{xy}$ -channel, calculated from DMFT. Close to the Fermi level, a vHs is observed. The inset are the PDOS of the  $d_{\gamma z}$  orbitals for completeion.

trend of temperature-dependent spectral weight in Fig. 4.13. These considerations lead to the conclusion that the  $d_{xy}$  dominated  $\gamma$ -states are responsible for nFL behaviour. Furthermore, the ratio between coherent and incoherent spectral weight (see Fig. 4.13(e)) indicates that  $Z \ll 1$  around the S-point [206, 207], in accordance with the DMFT value  $Z_{\text{DMFT}}^{xy} \simeq 0.05$ . I infer that electrons with  $d_{xy}$  character are stronger correlated and have a comparatively lower  $T_{\text{FL}}$ . In the temperature regime of our experiments, the QP mass renormalization and FL QP breakdown are orbitally selective.

I conclude by discussing possible origins of the orbital-selective FL QP breakdown. The experimentally determined band filling is consistent with our theoretical findings. Tab. 4.2 summarizes these aspects. In the LDA, all  $t_{2g}$  orbitals are occupied equally. When strong correlations are included in DMFT, the electron population is redistributed

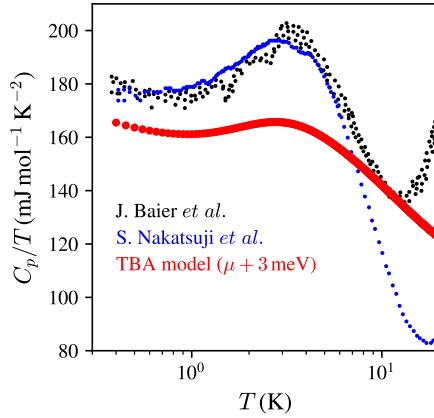


**Fig. 4.17** Heat capacity data  $c_p/T$  taken from ref. [75, 188]. Driving the TBA model through the vHs by shifting the band structure by 2.6 meV reproduces roughly the low-temperature dependence in the electronic specific heat.

from the  $d_{xy}$ - to the  $d_{\gamma z}$ -channel. As a result, the  $d_{xy}$ -orbital is close to half-filling and thus prone to Mott-localisation. This argument is a possible origin of nFL behaviour. Strong correlations in  $\text{Ca}_{1.8}\text{Sr}_{0.2}\text{RuO}_4$  are reflected in the quasiparticle residue (see Fig. 4.16 (a)), as the effective mass of the  $d_{xy}$ -electrons ( $\sim 20 m_b$ ) are largely enhanced compared to the  $d_{\gamma z}$ -electrons ( $\sim 5 m_b$ ). From self-energy analysis ( $\alpha$ -band) and coherent- to incoherent-weight ratio ( $\gamma$ -band), values of same order are obtained. A large band mass (and thus flat band) manifests itself as a vHs in the electronic DOS. As shown in recent strain-controlled experiments, a vHs from the  $\gamma$ -band close to the Fermi level induces a self-energy deviating from FL theory [86, 187]. Indeed, this might be the same driving force in  $\text{Ca}_{1.8}\text{Sr}_{0.2}\text{RuO}_4$  as a vHs, related to  $d_{xy}$ -orbitals, is observed in our DMFT calculations (see Fig. 4.16 (b)). The observed temperature dependence of the specific heat capacity  $C_p/T$  [75, 188] can be attributed to the proximity to the vHs to the Fermi level. This can be seen through evaluation of

$$C_p/T = \frac{1}{T} \frac{\partial}{\partial T} \int_{-\infty}^{\infty} \omega \overbrace{\sum_{\mathbf{k},s} \delta(\omega - \varepsilon_{\mathbf{k}})}^{\text{DOS}(\omega)} f(\omega, T) d\omega. \quad (4.3)$$

In Fig. 4.17, the result is shown when shifting the chemical potential of the TBA band structure by +3 meV. In this fashion the peak in the heat capacity at  $\sim 3$  K can be roughly reproduced.

## 4.5 Conclusions

New ARPES data on the low-energy band structure of  $\text{Ca}_{1.8}\text{Sr}_{0.2}\text{RuO}_4$  is presented. The complete FS is reconstructed, by fitting a six-orbital Hamiltonian to the experimental data. This is understood by folding the  $\text{Sr}_2\text{RuO}_4$  FS and optimizing TBA parameters. The new zone-centered  $\delta$ -band emerges. From FS area counting (Luttinger's theorem), the band filling amounts to the expected four electrons per Ru site, thus ruling out an OSMP. Polarisation-dependent spectra together with DMFT reveal the orbital characters. From resistivity it is clear, that  $\text{Ca}_{1.8}\text{Sr}_{0.2}\text{RuO}_4$  is a nFL system above  $\sim 1$  K. Self-energy analysis of the  $d_{\gamma z}$ -driven  $\alpha$ -band, however, expose FL behaviour with moderate  $Z \sim 0.5$ . Both, experiment and DMFT reveal a quasiparticle residue  $Z \ll 1$  and thus heavy effective mass, associated to the  $d_{xy}$ -electrons. In contrast to the temperature-stable  $\alpha$ -QP peak, the spectral weight of the  $d_{xy}$ -driven  $\gamma$ -pocket near the zone corner decays with increasing temperature, indicating deviation from a FL. This demonstrates a breakdown of FL QPs in an orbital-selective fashion. As a possible origin, DMFT suggests a vHs at the Fermi level and a band-filling close to half in the  $d_{xy}$  channel.



# Chapter 5

## Nature of the Mott insulator $\text{Ca}_2\text{RuO}_4$

### 5.1 Introduction

The Mott instability is perhaps the most prominent mechanism of how band theory breaks down [17]. For half-filled single-band systems it is well understood how the Mott insulating state emerges. In this simple case, every site on a periodic lattice is occupied by a single electron. A high Coulomb interaction to band width ratio  $U/W$  then localises the electron to the site it occupies and the on-site repulsion opens a spectral gap in the DOS near the Fermi level. This simple scenario does not apply to  $\text{Ca}_2\text{RuO}_4$ . The ruthenium-ions have a valency of  $\text{Ru}^{4+}$  and the  $2p$ -shell of the oxygen is completely filled. Thus, leaving four electrons in the  $t_{2g}$  manifold of the  $4d$ -shell of ruthenium ( $2/3$  filling). Additionally, several important energy scales enter the equation. Orbital and spin degrees of freedom in this multiband system are dictated by a delicate interplay of Hund's coupling  $J_H$ ,  $U$  and the crystal field [20]. It has further been shown that the spin-orbit interaction  $\lambda_{\text{so}}$  plays a role in forming the magnetic moments of the antiferromagnetic ground state [110, 208, 209].

The multiorbital nature of  $\text{Ca}_2\text{RuO}_4$  and the  $2/3$ -filling of the valence band have led to contradictory theoretical considerations of how the Mott insulating state is developed [35, 96, 99, 111]. In the OSMP scenario, different orbitals of the  $t_{2g}$ -manifold are Mott-insulating, each at a  $U_c$ , depending on band filling [111]. Generally, it is believed that orbitally-selective behaviour is triggered by a sufficiently high enough  $J_H$ , promoting orbital separation and has been proposed to take a crucial role in  $\text{Ca}_{2-x}\text{Sr}_x\text{RuO}_4$ . In a more conventional fashion – the band-Mott scenario –  $c$ -axis

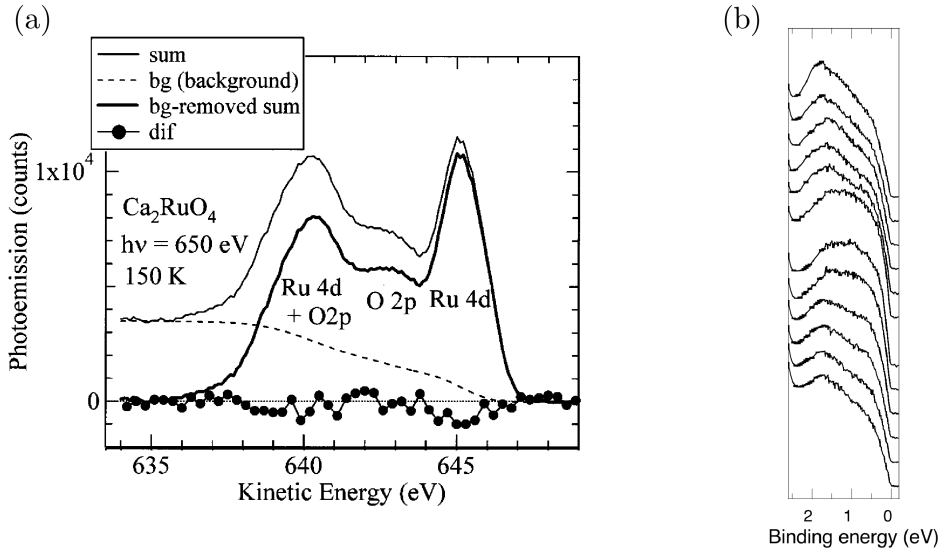


**Fig. 5.1** (a) Angle integrated photoemission data on  $\text{Ca}_2\text{RuO}_4$ . Ruthenium states are observed close to the Fermi level [211] (right hand side on the kinetic energy scale). (b) Photoemission spectra taken along a high symmetry direction [210].

contraction stabilises the completely filled  $d_{xy}$ -orbital [35, 96, 99]. Thus, leaving the  $d_{\gamma z}$ -bands half-filled which undergo a Mott transition.

There are only a few experimental studies of the low-energy electronic band structure of  $\text{Ca}_2\text{RuO}_4$  available [210, 211] (Fig. 5.1). So far, their data have not been able to pin down the exact nature of the Mott transition. An early angle-integrated photoemission spectroscopy study shows that Ru states exist near the Fermi level [211]. Another study measures the photoemission intensity angularly resolved, but do not observe dispersive structures [210].

In this work, we study  $\text{Ca}_2\text{RuO}_4$  in the paramagnetic insulating phase at  $T \simeq 160 \text{ K}$ . Our ARPES experiments reveal the complete electronic structure in the vicinity of the Fermi energy. Three bands, labelled  $\mathcal{A}$ ,  $\mathcal{B}$  and  $\mathcal{C}$  are identified. Together with ab-initio DFT band structure calculations the orbital characters are discussed. By modifying the Green's function, different scenarios are tested and compared to the experimental results on a qualitative level. Good agreement is found, by shifting the  $d_{xy}$  states below  $E_F$  and impose a Mott gap onto the  $d_{\gamma z}$  bands. A qualitative analysis of the atomic multiplet give insight into the origin of the band energies. Additional DMFT calculations support the band-Mott picture and thus ruling out the OSMP scenario.

## 5.2 Methods

### 5.2.1 Experimental

ARPES spectra were recorded at the SIS, I05 and MAESTRO beamlines. Both electron analyzer slit geometries – horizontal and vertical – were used in our experiments. Clean surfaces were obtained by cleaving the samples *in-situ* using the top-post cleaving method.

Insulators are inherently difficult to measure in photoemission experiments. The main reason is that the created photoholes cause the material to charge up electrostatically because the electron reservoir (sample holder) fails to deliver the deficient electrons at the surface. As a consequence, the kinetic energy of the photoelectrons is lower in the presence of the electrostatic potential of the photoholes. Therefore, the photoemission spectra appear shifted towards higher binding energies, misrepresenting the true energy scale. In our ARPES experiments, we held the samples at a constant temperature ( $T \simeq 160$  K, resulting in an overall energy resolution of approximately 50 meV) to increase electron diffusion and to broaden the Fermi-Dirac distribution such that empty states allow a sufficient conduction of charge carriers. No detectable charging was observed when varying the photon flux.

### 5.2.2 Band structure calculations

The same DFT+LDA and DFT+DMFT methodology has been applied as given in 4.2.2 with experimental lattice constants ( $a = 5.39$  Å,  $b = 5.59$  Å and  $c = 11.77$  Å). Furthermore, a first principles tight-binding model Hamiltonian was constructed. The Bloch matrix elements were calculated by projecting onto Wannier orbitals [212, 213] (constructed from Ru  $t_{2g}$  orbitals), resulting in a 24-band spin-orbit coupled model. These matrix elements are used to model Mott physics, outlined in the discussion part of this chapter.

## 5.3 Results

### 5.3.1 Oxygen bands

In Fig. 5.2 the electronic band structure of  $\text{Ca}_2\text{RuO}_4$  is presented. Experimental data (a–c) were taken with  $\bar{\pi}$ -polarized 65 eV photons along the high symmetry axis  $\Gamma$ –X and the zone boundary X–S (solid lines in (c)). The red dashed lines mark the energy of the

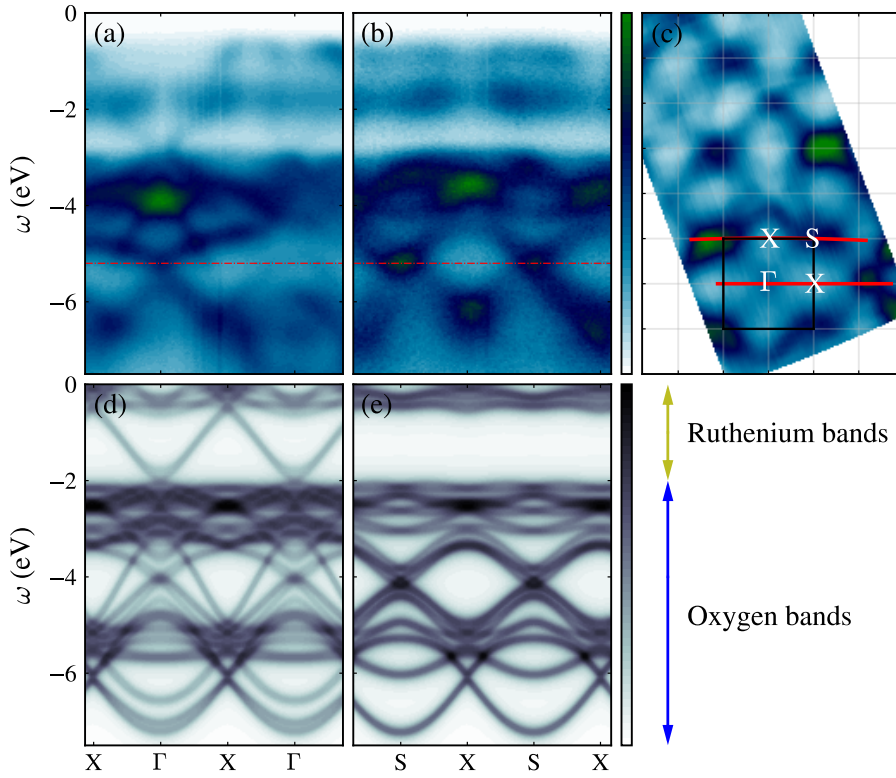


**Fig. 5.2** Electronic band structure of  $\text{Ca}_2\text{RuO}_4$ . ARPES data (a–c) were recorded with  $\pi$ -polarized light at 65 eV photon energy. Red dashed lines indicate the energy of the constant energy map in (c). There, the corresponding spectral cuts in k-space are shown as red solid lines. High symmetry points are labelled as  $\Gamma$ , S and X. (d, e) are DFT band structure calculations. Close to  $E_F$ , we find ruthenium excitations and at higher binding energies are the oxygen bands, indicated by the arrows on the right hand side. The linear color scales start with zero intensity.

( $k_x$ ,  $k_y$ )-map in (c) at  $\omega = -5.2$  eV. In the paramagnetic insulating phase (measured at  $T \simeq 160$  K), no spectral weight is observed at the Fermi level  $E_F$ . In the range  $-3$  eV  $< \omega < -0.5$  eV, relatively weak features are found compared to the intensity signal at higher binding energies.

In our DFT calculations, we find oxygen and ruthenium bands as indicated with arrows in Fig. 5.2 (d, e). On the one hand, up to an arbitrary shift the oxygen excitations are relatively well reproduced. Comparing to the experimental results, regions of high degeneracy are clearly observed at the high symmetry points. On the other hand, we find large discrepancies concerning the ruthenium bands that, for example, are metallic in the DFT results.

### 5.3.2 Ruthenium bands

Let's focus on the ruthenium bands, that are identified by comparison to DFT as being closest to the Fermi level. A compilation of experimental data is shown in Fig. 5.3 – 5.4. Spectral weight is completely suppressed from  $E_F$  down to approximately  $\Delta = 200$  meV binding energy. Assuming a symmetric gap around the Fermi level from valence- to conduction band, this value is in agreement with a resistivity activation behaviour  $\rho_{ab}(T) \propto \exp(E_G/2k_B T)$  with  $E_G \simeq 2\Delta = 0.4$  eV [185].

Throughout all spectra, a non-dispersive and broad band is found at  $\omega \simeq -1.7$  eV. This feature has also been found in a previous angle-integrated photoemission study [211] (see Fig. 5.1 (a)). EDC's reveal a characteristic two-peak structure (Fig. 5.3 (c, f)), where the dispersive structure close to  $E_F$  and the broad flat band are labeled  $\mathcal{A}$  and  $\mathcal{B}$ , respectively. Additionally, a fast dispersing band around the zone centers is observed between  $-2.5$  eV  $< \omega < -2.0$  eV. It is identified by the MDC at  $\omega = -2.25$  eV, indicated by red horizontal dashed line in Fig. 5.3 (a) and is plotted in the top inset. For this band, which is labelled  $\mathcal{C}$ , we estimate a band velocity of  $v = 2.6(4)$  eVÅ.

In our measurements, the band structure shows significant changes in photoemission intensity for different photon energies or polarisations (see Fig. 5.3). Distinct behaviour of the  $\mathcal{A}$ - and  $\mathcal{B}$ -band is observed. As the  $\mathcal{C}$ -band disperses from the  $\Gamma$ -point, it merges with the flat  $\mathcal{B}$ -band. Judging from the data, it is not clear if it extends further as the  $\mathcal{A}$ -band or not. Furthermore, their intensity variations of spectral weight (matrix element effects) correlate only to a certain degree. From an experimental point of view, it thus makes sense to distinguish the  $\mathcal{A}$ - from the  $\mathcal{C}$ -band. A full picture of the low-energy band structure is shown in Fig. 5.4. The spectra are shown along the high symmetry path in  $k$ -space, indicated by the solid red lines in the constant energy map at  $\omega = -2.4$  eV in Fig. 5.4 (b). Theoretical results and discussions refer to this figure by comparison.

### 5.3.3 Orbital characters

Next we turn to the orbital character assignment of the bands. There exist several DFT and DMFT studies on the band structure of  $\text{Ca}_2\text{RuO}_4$  [99, 214–217]. Although details in their methodology differ, they identify a dispersing band centered around the  $\Gamma$ -point and a flat band throughout the whole BZ.

Similar to these studies, we find in our DFT results a fast dispersing band, evolving around the zone center. Plotted in an orbitally resolved fashion in Fig. 5.5 (a), these features carry  $d_{xy}$  character. The flat bands, however, have predominantly  $d_{yz}$  orbital

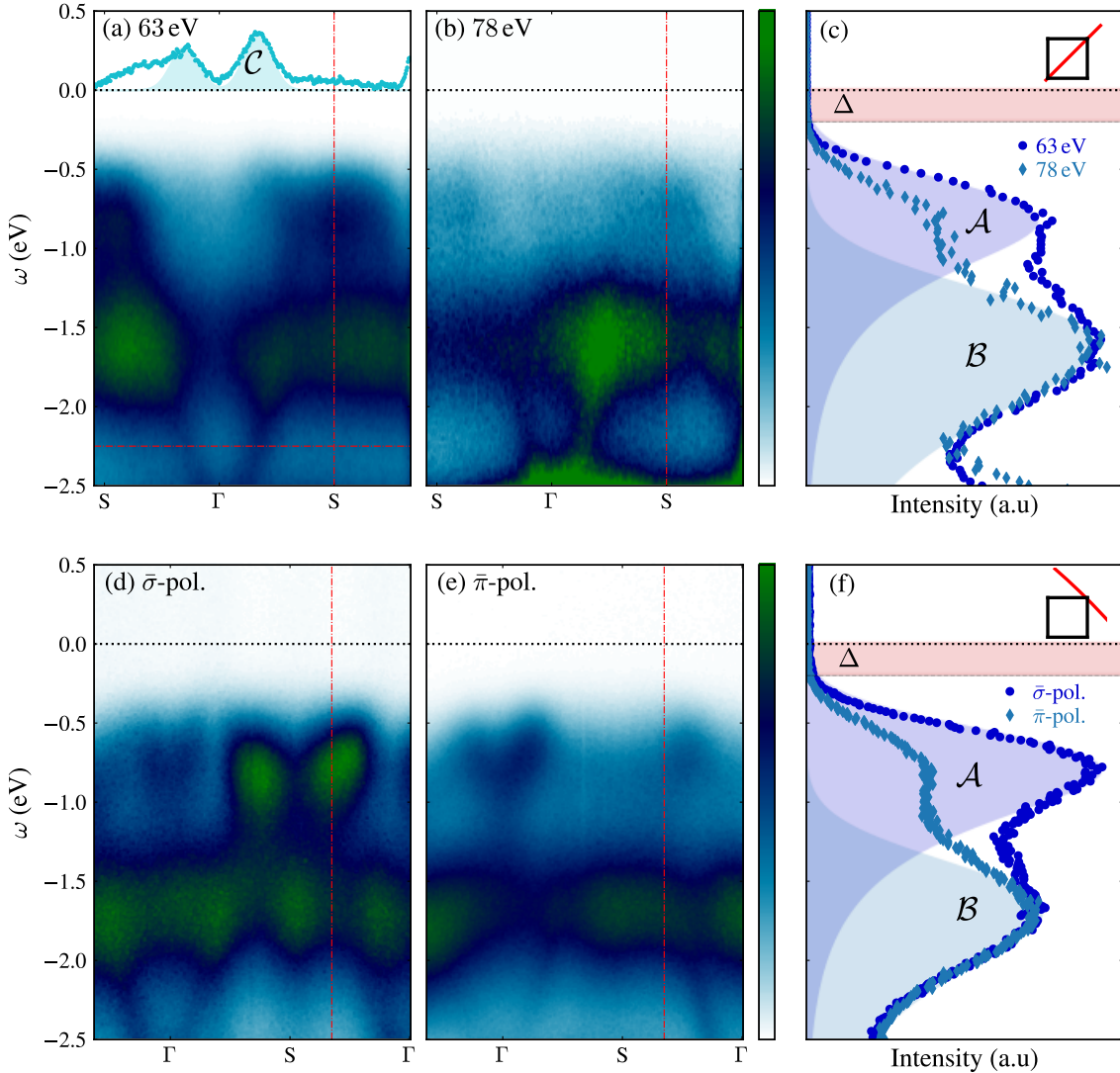


**Fig. 5.3** Photoemission data recorded along the  $\Gamma$ -S direction with circularly polarized light in (a) and (b). Spectra taken with incident photon energies 63 eV and 78 eV are shown. Vertical red dashed lines at the S-point indicate the EDC's shown in (c). A double peak structure reveals the  $\mathcal{A}$ - and  $\mathcal{B}$ -band. No spectral weight is found near  $E_F$ , highlighted by the red shaded area down to  $\Delta \simeq 200$  meV binding energy. The horizontal red dashed line at  $\omega = -2.25$  eV marks the MDC shown as an inset in (a), revealing the fast dispersing  $\mathcal{C}$ -band. Shaded areas in blue tones are exponentially modified Gaussian fits. The inset in (c) shows schematically the BZ boundary and the spectral cut along the zone diagonal indicated by the red solid line. (d, e) Photoemission data recorded along the  $\Gamma$ -S direction in the second zone with incident photon energy  $h\nu = 65$  eV. Spectra taken with light polarisations  $\bar{\sigma}$  and  $\bar{\pi}$  are shown. Vertical red dashed lines close to the S-point indicate the EDC's shown in (f).

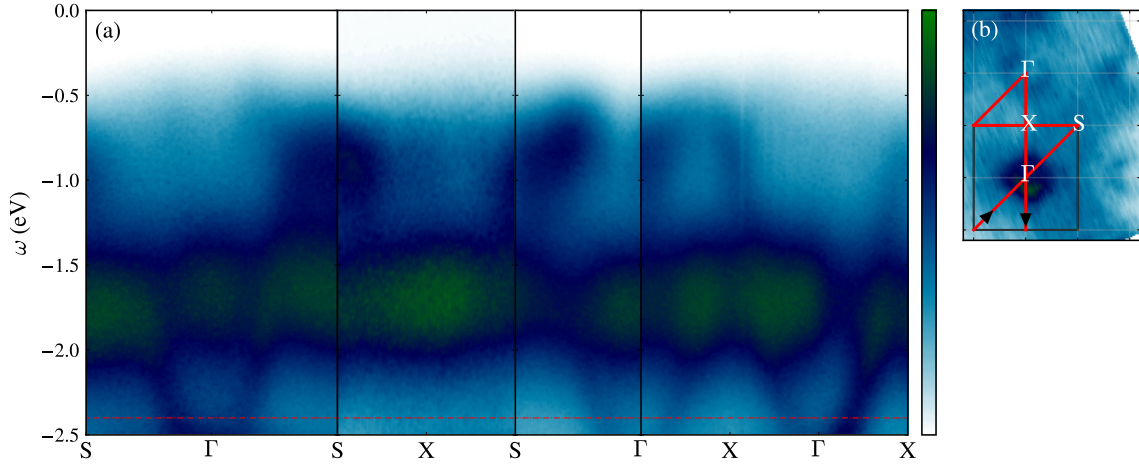


**Fig. 5.4** Photoemission data recorded with 65 eV, circularly polarised light. (a) Compilation of ARPES spectra along the high symmetry path indicated by the solid red line in the  $(k_x, k_y)$ -map, shown in (b) at  $\omega = -2.4$  eV (marked by the red dashed line).

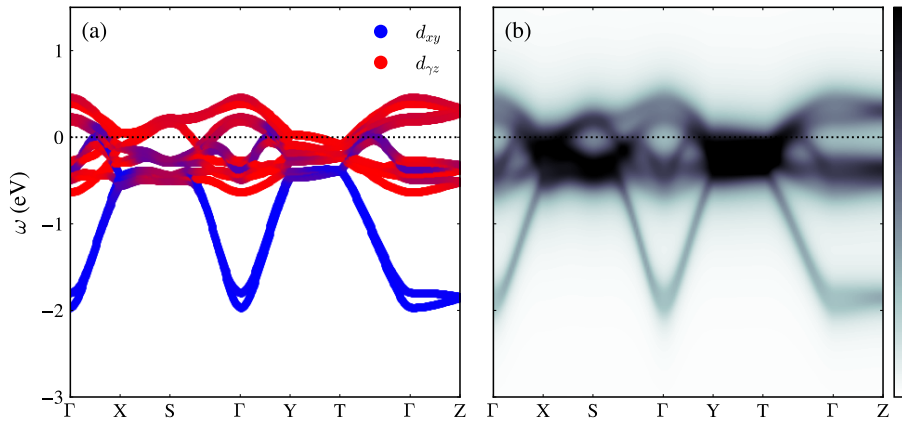


**Fig. 5.5** DFT calculations in the LDA along different high symmetry directions. (a) Results are plotted orbitally resolved. Blue points correspond to  $d_{xy}$  and red to  $d_{\gamma z}$  orbital character. (b) Spectral representation of the spectral function with a thermal broadening ( $T = 160$  K).

character. Fig. 5.5 (b) is a spectral representation of the spectral function with a constant thermal broadening of  $k_B T$  with  $T = 160$  K. Comparing to the experimental data Fig. 5.3 – 5.4, I assign  $d_{xy}$ - to the same V-shaped  $\mathcal{C}$ - and  $d_{\gamma z}$  orbital character to the flat  $\mathcal{B}$ -band, respectively.

As seen in Fig. 5.3, the photoemission intensity varies strongly as a function of photon energy and light polarisation. In principle, matrix element effects contain information about the orbital character of a band. The data suggests that the orbital character of

the  $\mathcal{A}$ -band is different from the  $\mathcal{B}$ -band, but it is not clear if it is smoothly connected to the  $\mathcal{C}$ -band, which has  $d_{xy}$  orbital character. Additional investigation of  $(k_x, k_y)$ -maps at  $\omega = -0.5$  eV with different photon energies and polarisations, do not reveal much regularity of the intensity distribution (see Appendix B). The contrast between linear horizontal and vertical light therefore vary strongly with momentum. This fact inhibits me to draw any simple conclusions based on matrix element effects. To this point, I cannot make a firm conclusion about the orbital nature of the  $\mathcal{A}$ -band near the Fermi level.

## 5.4 Discussion

### 5.4.1 Phenomenological modeling

Let's start discussing the band structure more globally. From DFT calculations (see Fig. 5.5), it is clear that it does not reproduce the Mott insulating state. We can, however, try to mimic the experimental band structure by including a self-energy in a phenomenological fashion. With the imaginary part of the Green's function

$$\mathcal{G}(\mathbf{k}, \omega) = \frac{1}{\omega - \mathcal{H}_{\mathbf{k}}^0 - \Sigma(\omega)}, \quad (5.1)$$

we obtain the spectral function by taking the trace of all orbital degrees of freedom. The matrix elements of the Hamiltonian  $\mathcal{H}_{\mathbf{k}}^0$  stem from our DFT calculations. Note that at this point, no self-energy is included. To first order, imposing a spectral gap  $\Delta$  acting on all bands uniformly would transfer spectral weight away from the Fermi level (see Fig. 5.6 (a)). To reproduce the Mott-gap near the Fermi level, a self-energy with a  $1/\omega$ -term is used:

$$\Sigma(\omega) = \Delta^2/\omega + i(\pi k_B T)^2 \quad (5.2)$$

with  $\Delta = 0.6$  eV and  $T = 160$  K. Comparing this model (see Fig. 5.6 (b)) to the experimental data, we observe that the flat  $\mathcal{B}$ -band is not found at  $\omega \simeq -1.7$  eV. It is clear, that this model yields a poor fitment. Thus I discard the scenario of a uniform gap.

Next, we test the scenario of an orbitally-selective Mott insulator, where distinct subsets of bands open a gap in the DOS for different critical Coulomb interaction strengths  $U_c$  [111] (see Fig. 5.6 (c)). In theory, a significantly high Hund's coupling  $J_H$  is needed to trigger this behaviour, since it tends to suppress orbital fluctuations such

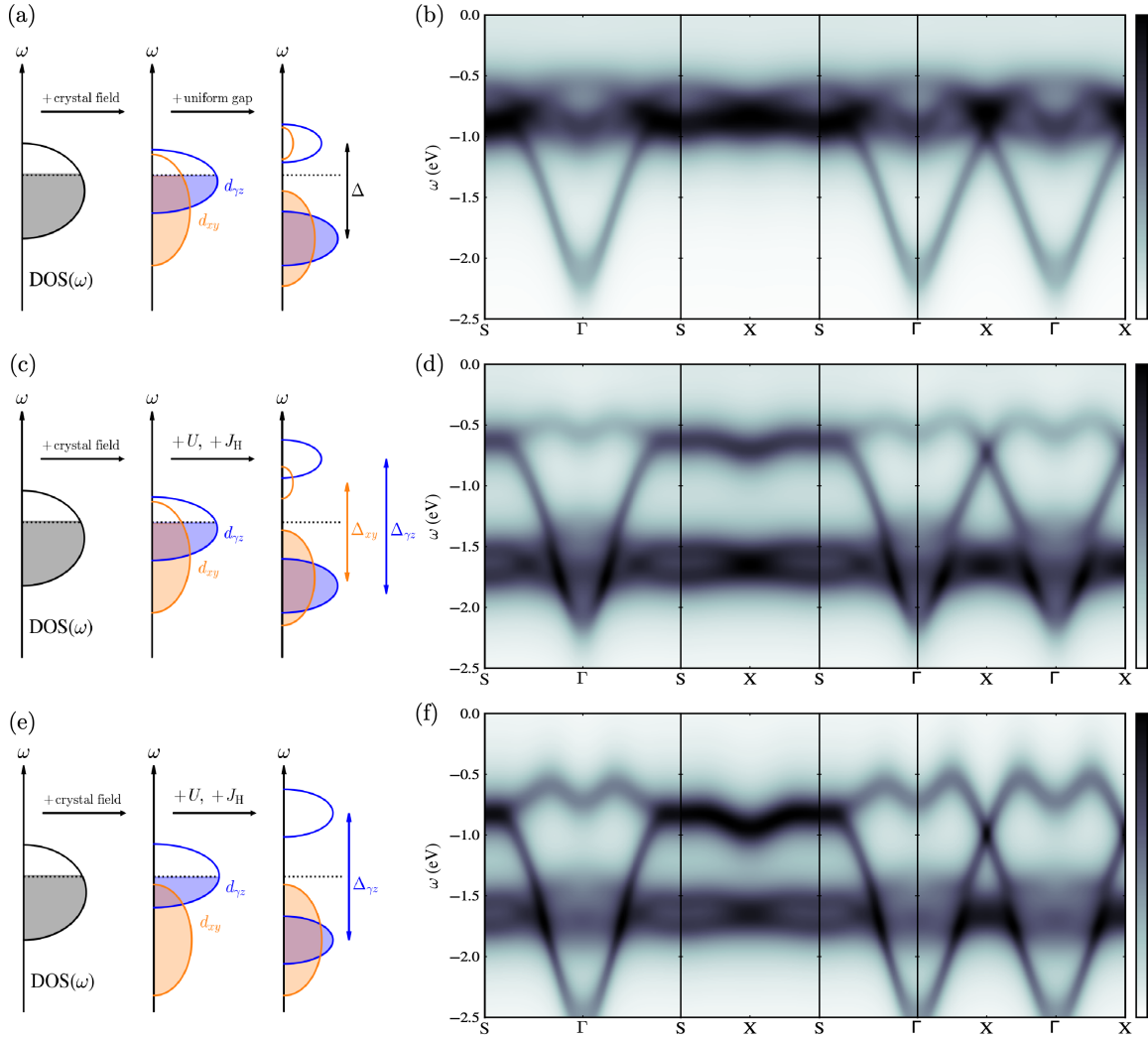


**Fig. 5.6** (a) Schematic DOS, with a uniform gap  $\Delta$ . (b) Spectral function representation of the DFT band structure with a self-energy given by eq. (5.2). (c) Schematic DOS, with orbitally selective gaps  $\Delta_{xy}$  and  $\Delta_{\gamma z}$ . (d) Spectral function representation of the DFT band structure with a self-energy given by eq. (5.3). (e) Schematic DOS, with an enhanced crystal field and Mott gap  $\Delta_{\gamma z}$ . (f) Spectral function representation with self-energy and Hamiltonian given by eq. (5.4).

that bands can be viewed as separate. Here, we use projectors  $\mathcal{P}_\alpha$  to impose spectral gaps  $\Delta_\alpha$  onto a  $t_{2g}$ -orbital  $\alpha$ . The self-energy

$$\Sigma(\omega) = \frac{1}{\omega} (\mathcal{P}_{xy}\Delta_{xy}^2 + \mathcal{P}_{\gamma z}\Delta_{\gamma z}^2) + i(\pi k_B T)^2, \quad (5.3)$$

with  $\Delta_{xy} = 0.6$  eV and  $\Delta_{\gamma z} = 1.55$  eV yields a spectral function, shown in Fig. 5.6 (d). We observe that the  $\mathcal{B}$ -band is reproduced at the correct energy. There is, however, a

discrepancy compared to the experiment (Fig. 5.4). The bottom part of the V-shape of the fast dispersing band does not match the energy of the  $\mathcal{C}$ -band, leading to incompatible band widths. Due to this fact, I tend to discard the OSMP picture as well. Finally, it has been argued that the crystal field is strong enough to push the  $d_{xy}$ -states completely below the Fermi level. As a consequence, the half-filled  $d_{\gamma z}$ -bands naturally become Mott insulating (Fig. 5.6(e)). This scenario has been favoured by several theoretical studies [35, 96, 99]. To model the physics, we insert a Mott gap  $\Delta_{\gamma z} = 1.55$  eV, acting on the  $d_{\gamma z}$ -bands and furthermore shift the  $d_{xy}$ -states by an enhanced crystal field  $\Delta_{\text{CF}} = 0.6$  eV.

$$\Sigma(\omega) = \mathcal{P}_{\gamma z}\Delta_{\gamma z}^2/\omega + i(\pi k_B T)^2, \quad \mathcal{H}_{\mathbf{k}} = \mathcal{H}_{\mathbf{k}}^0 - \mathcal{P}_{xy}\Delta_{\text{CF}}. \quad (5.4)$$

The spectral function of this model is shown in Fig. 5.6(f). Now the bottom of the  $\mathcal{C}$ -band is reproduced and the  $\mathcal{B}$ - and  $\mathcal{A}$ -band are found at the correct energies. The fact that the  $\mathcal{C}$ -band lies well below the flat  $\mathcal{B}$ -band, concludes that the  $d_{xy}$ -states are shifted below  $E_F$  due to an interaction enhanced crystal field. The agreement between the phenomenological model and experimental data suggests to assign predominantly  $d_{xy}$  orbital character to the  $\mathcal{A}$ -band.

### 5.4.2 DMFT and multiplet analysis

We now discuss the DMFT results. As used successfully for other ruthenate studies, we set  $U = 2.3$  eV and  $J_H = 0.4$  eV [20, 143, 200]. The resulting spectral function shows the  $\mathcal{C}$ - and  $\mathcal{B}$ -band correctly. Also the  $\mathcal{A}$ -band appears between  $-0.7$  eV  $< \omega < 0$  eV, although not smoothly connected to the  $\mathcal{C}$ -band. To make progress we investigate the orbitally-resolved results by discussing a simple multiplet analysis. Consider the rotationally invariant, simplified Hamiltonian of the Kanamori form for  $t_{2g}$ -states [20]

$$\mathcal{H}_{t_{2g}} = (U - 3J_H)\frac{\hat{N}(\hat{N} - 1)}{2} - 2J_H\hat{S}^2 - \frac{J_H}{2}\hat{L}^2 + \frac{5}{2}J_H\hat{N} \quad (5.5)$$

where  $\hat{N}$ ,  $\hat{S}$  and  $\hat{L}$  are the number, spin and orbital momentum operator. Note that this Hamiltonian respects the first (maximize  $S$ ) and the second (maximize  $L$ ) Hund's rules. The spectrum is given in Table 5.1.

Since the RuO-octahedra have a contracted  $c$ -axis, it is reasonable to assume the  $d_{xy}$ -states to be lower in energy than the  $d_{\gamma z}$ -states. Having four  $4d$  electrons, we place the first two ( $\uparrow, \downarrow$ ) into the  $d_{xy}$ -orbital, by virtue of the Pauli principle. The remaining two electrons occupy the  $d_{\gamma z}$ -orbitals in a triplet configuration ( $\uparrow, \uparrow$ ), aligned by  $J_H$ .

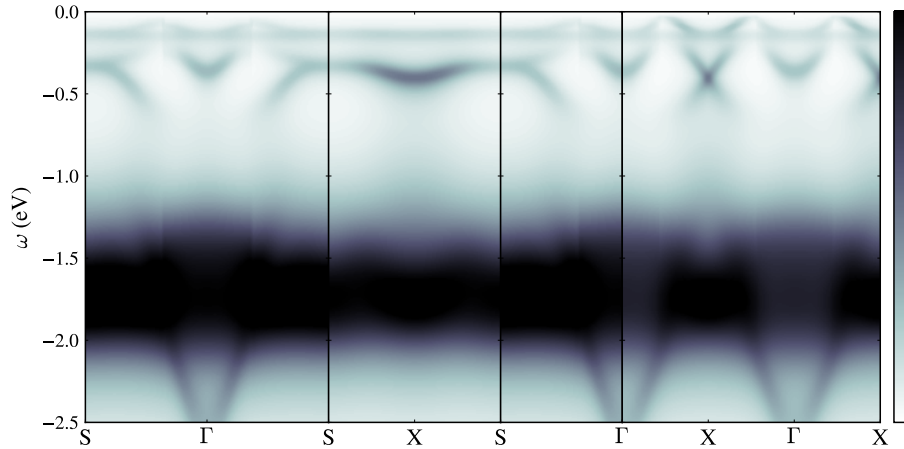


**Fig. 5.7** Spectral function obtained from DMFT. The parameters have been fixed to  $U = 2.3 \text{ eV}$  and  $J_H = 0.4 \text{ eV}$ .

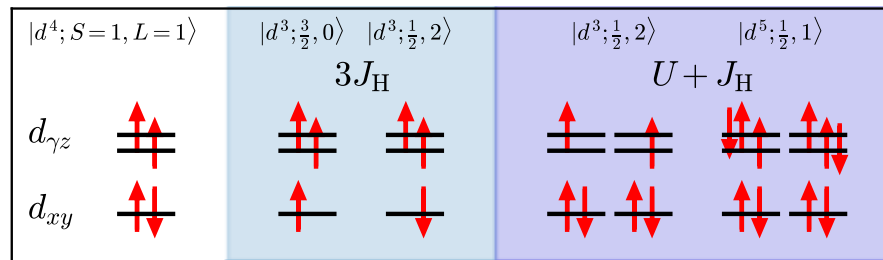


**Fig. 5.8** Multiplet analysis of  $4d$  Ru-shell in the atomic limit. Left (white background): ground state  $d^4$  configuration. Middle (light blue background): configurations for  $d_{xy}$ -electron removal. The low spin- and high spin-state differ by  $3J_H$  in energy. Right (dark blue background): multiplets for the case of  $d_{\gamma z}$ -electron removal or addition. The energy difference between the  $d^3$  and  $d^5$  (each two-fold degenerate) configurations is  $U + 3J_H$ .

Hence the notation  $|d^4; S = 1, L = 1\rangle$  (see Fig. 5.8 on the left). In the  $d_{xy}$ -channel we cannot add an electron since the orbital is full. But we can either remove the  $\downarrow$ - or the  $\uparrow$ -electron, leading to a high spin  $|d^3; \frac{3}{2}, 0\rangle$ - or a low spin  $|d^3; \frac{1}{2}, 2\rangle$ -state, respectively (see Fig. 5.8 in the middle). From Table 5.1, we infer an energy difference of

$$E_{|d^3; \frac{3}{2}, 0\rangle} - E_{|d^3; \frac{1}{2}, 2\rangle} = 3J_H. \quad (5.6)$$

From these considerations, we deduce that the  $\mathcal{A}$ -band can be assigned to the energetically favorable high spin-state while the  $\mathcal{C}$ -band to the low spin-state. In the  $d_{\gamma z}$ -channel, we can either remove or add an electron. For both cases we find the two

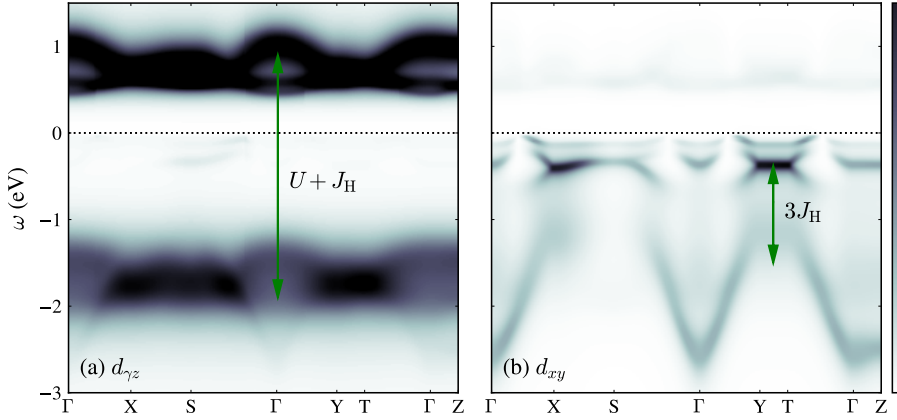


**Fig. 5.9** DMFT calculations orbitally resolved. (a) The  $d_{\gamma z}$ -states open up a gap of order  $U + J_H$ . (b) The  $d_{xy}$ -bands are completely below the Fermi level and split in a high spin- (closer to  $E_F$ ) and a low spin-state, separated by  $\sim 3J_H$ .

degenerate configurations (see Fig. 5.8 on the right)  $|d^3; \frac{1}{2}, 2\rangle$  and  $|d^5; \frac{1}{2}, 1\rangle$ . The Mott gap of the  $d_{\gamma z}$ -doublet is then estimated by our considerations in the atomic limit as

$$\Delta_{\gamma z} = (E_{|d^5; \frac{1}{2}, 1\rangle} - E_{|d^4; 1, 1\rangle}) - (E_{|d^4; 1, 1\rangle} - E_{|d^3; \frac{1}{2}, 2\rangle}) = U + J_H. \quad (5.7)$$

$N$	$S$	$L$	Energy
$\mathcal{U} = U - 3J_H$			
0, (6)	0	0	$(0, 15\mathcal{U})$
1, (5)	$1/2$	1	$-5J_H/2, (10\mathcal{U} - 5J_H/2)$
2, (4)	1	1	$\mathcal{U} - 5J_H, (6\mathcal{U} - 5J_H)$
2, (4)	0	2	$\mathcal{U} - 3J_H, (6\mathcal{U} - 3J_H)$
2, (4)	0	0	$\mathcal{U}, (6\mathcal{U})$
3	$3/2$	0	$3\mathcal{U} - 15J_H/2$
3	$1/2$	2	$3\mathcal{U} - 9J_H/2$
3	$1/2$	1	$3\mathcal{U} - 5J_H/2$

**Table 5.1** Spectrum of the rotationally invariant Kanamori Hamiltonian from eq. (5.5). Note that  $\mathcal{U} = U - 3J_H$ .

Plotting the DMFT results in an orbitally-resolved fashion highlights the characteristics found in our multiplet-analysis, shown in Fig. 5.9. Panel (a) shows a Mott gap

developing in the  $d_{\gamma z}$ -doublet of order  $U + J_{\text{H}}$ . In panel (b) the completely filled  $d_{xy}$ -band splits into a high- and low spin-state, separated by an energy of order  $3J_{\text{H}}$ .

## 5.5 Conclusions

In summary, new ARPES data of the low-energy band structure of  $\text{Ca}_2\text{RuO}_4$  in the paramagnetic Mott-insulating state ( $T \simeq 160$  K) were presented. We observe a dispersing band near the Fermi level ( $\mathcal{A}$ ), a flat band ( $\mathcal{B}$ ) and a V-shaped band ( $\mathcal{C}$ ). With DFT calculations we assign a  $d_{xy}$  orbital character to the  $\mathcal{C}$ -band and a  $d_{\gamma z}$ -character to the  $\mathcal{B}$ -states. By imposing a self-energy in a phenomenological fashion, we reproduced the experimental band structure. Together with DMFT results I infer that

1. The  $\mathcal{A}$ -band near  $E_{\text{F}}$  has  $d_{xy}$ -character.
2. Orbitally-selective Mott gaps are absent.
3. The  $d_{xy}$  orbital driven bands are completely filled.
4. A Mott gaps opens in the (half-filled)  $d_{\gamma z}$ -doublet.

It is important to notice that Hund's coupling has a large influence on the  $d_{xy}$ -states. Further, our results highlight the crystal field stabilization of the  $d_{xy}$ -orbital. The impact of  $U$  and  $J_{\text{H}}$  on the MIT of  $\text{Ca}_{2-x}\text{Sr}_x\text{RuO}_4$  would be of great interest. Findings of this work were published 2017 in Nature Communications [218].



# Chapter 6

## Conclusions & Outlook

Ever since Karl Alex Müller and Georg Bednorz discovered HTSC in cuprates, huge scientific efforts have been made for the study of strongly correlated systems.  $\text{Sr}_2\text{RuO}_4$  entered the stage as it exhibits SC while being isostructural to  $\text{La}_{2-x}\text{Ba}_x\text{CuO}_4$ . As ruthenate research progressed, dense phase diagrams for partial substitutions in the chemical compositions of single- and multi-layered systems were found. Several energy scales compete with each other and generate a wealth of different ground states. Due to the multi-orbital nature of the intermediately filled  $4d-t_{2g}$  manifold, Hund's coupling takes a prominent role. It suppresses orbital fluctuations and potentially triggers orbital-selective physics. For the Mott-insulating parent compound  $\text{Ca}_2\text{RuO}_4$  and the critical composition for the MIT  $\text{Ca}_{1.8}\text{Sr}_{0.2}\text{RuO}_4$ , it was not clear to what extent orbital-selective physics is effective.

In this work I presented new ARPES data together with band structure calculations of those two mentioned materials. In  $\text{Ca}_2\text{RuO}_4$  the contraction of the  $c$ -axis stabilises the  $d_{xy}$ -orbital and becomes band-insulating. The remaining half-filled  $d_{\gamma z}$  bands then undergo a Mott-transition, thus explaining the insulating nature of  $\text{Ca}_2\text{RuO}_4$ . From our  $\text{Ca}_{1.8}\text{Sr}_{0.2}\text{RuO}_4$ -study, we exclude the OSMP scenario. Although resistivity measurements clearly show nFL behaviour, we demonstrate the existence of FL QPs associated to the  $d_{\gamma z}$ -driven  $\alpha$ -band. With increasing temperature spectral weight of the  $d_{xy}$ -driven  $\gamma$ -band decays, contrasting the temperature-stable  $\alpha$ -states. Our experiment and DMFT calculations demonstrate strong band renormalizations ( $Z(d_{\gamma z}) \sim 0.5$ ,  $Z(d_{xy}) \ll 1$ ) and an orbital-selective breakdown of FL QPs.

It would be interesting to study the  $\gamma$ -band systematically in  $\text{Ca}_{2-x}\text{Sr}_x\text{RuO}_4$  for  $x$  around 0.2. Fig. A.1, for example, shows ARPES data on the more metallic  $\text{Ca}_{1.7}\text{Sr}_{0.3}\text{RuO}_4$ , taken with 22 eV, circularly polarised photons at 6 K. The spectra appear to be generally sharper and the  $\gamma$ -band around S (see zone corners in Fig. A.1 (b))

displays a sharper crossing of the Fermi level (see Fig. A.2). A complete data set including temperature dependence along  $\Gamma$ –S and self-energy analysis for different  $x$  allows direct comparison to the orbital-selective FL breakdown in  $\text{Ca}_{1.8}\text{Sr}_{0.2}\text{RuO}_4$ . As the  $\delta$ -band also appears in Appendix Fig. A.1 (a, b), it would be naturally to ask at which critical composition  $x$  the  $\delta$ -pocket vanishes.

In-situ alkali metal evaporation in an ARPES experiment offers new possibilities to explore exotic ground states. As an example, by doping the surface with K, the spin-orbit assisted Mott-insulator  $\text{Sr}_2\text{IrO}_4$  develops *Fermi arcs* (partially gapped FS states) indicating the emergence of unconventional SC. Inspired by these results, we conducted similar experiments on  $\text{Ca}_2\text{RuO}_4$  at the MAESTRO beamline at the ALS. Our ARPES results reveal peculiar interactions between the alkali atoms and the Mott-insulating substrate. Experimental evaluations and theoretical considerations are object of current research.

In a big picture, due to rich phase diagrams of the ruthenates, these systems hold great potential as prototypical materials for strongly correlated systems. An understanding of novel ground states form the basics for technological advances. Although immediate practical applications are often difficult to realize, a fundamental comprehension of the origins and driving forces of these ground states, enables an effective search for suitable alternatives. The field of strongly correlated electrons is therefore an exciting pillar of condensed matter physics and a promising pathway to new technologies.

# Appendix A

## Low-energy band structure of $\text{Ca}_{1.7}\text{Sr}_{0.3}\text{RuO}_4$

Fig. A.1 shows spectral cuts along  $\Gamma$ -Y and X-S and the FS of  $\text{Ca}_{1.7}\text{Sr}_{0.3}\text{RuO}_4$ . Generally, the spectral features appear sharper compared to the data of  $\text{Ca}_{1.8}\text{Sr}_{0.2}\text{RuO}_4$  (see Fig. 4.6). A significant difference is the missing spectral weight at the S-point (see Fig. A.1 (c)). In the ARPES recording along  $\Gamma$ -S (see Fig. A.2), the  $\gamma$ -band crosses the FS, displayed in the MDC at  $E_F$  and fitted by two Lorentzians. These findings suggest, that the vHs in the  $x = 0.3$  compound might be found above the Fermi level.

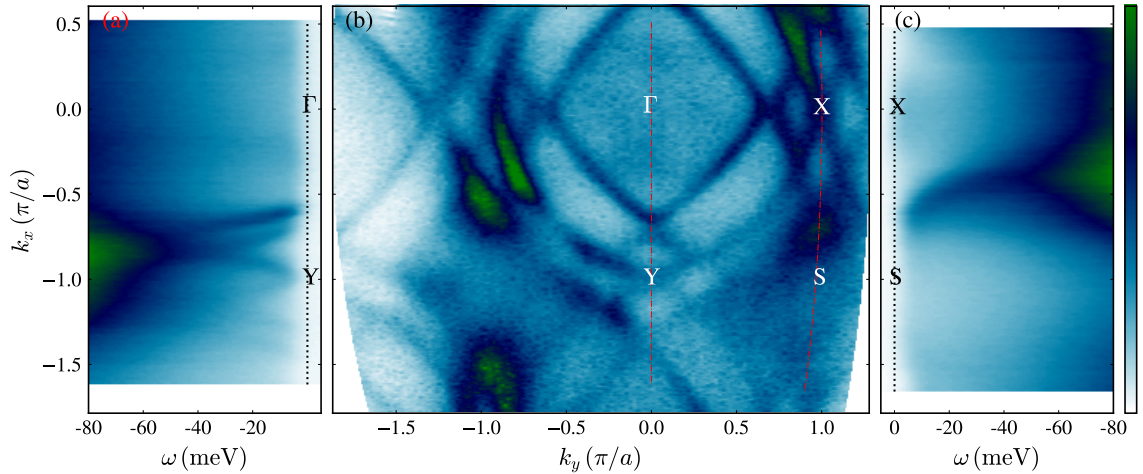


**Fig. A.1** Low-energy band structure of  $\text{Ca}_{1.7}\text{Sr}_{0.3}\text{RuO}_4$ . (a) ARPES spectrum along  $\Gamma$ -Y recorded with 22 eV circularly polarised light. (b) Experimental FS map. The trajectories of ARPES spectra shown (a) and (c) are indicated by dashed cyan lines. (c) Spectral cut along the zone boundary X-S.

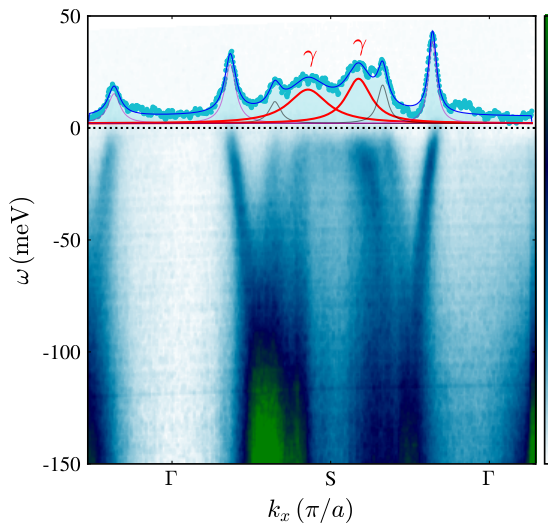


**Fig. A.2** ARPES cut along  $\Gamma$ -S with circularly polarised 72 eV photons. An MDC integrated from  $E_F$  to  $E_F - 5$  meV is shown, fitted by lorentzians. Peaks from the  $\gamma$ -band are indicated as a thicker line in red, displaying a more clear Fermi-level crossing than in  $\text{Ca}_{1.8}\text{Sr}_{0.2}\text{RuO}_4$ .

## Appendix B

### Matrix element effects in $\text{Ca}_2\text{RuO}_4$

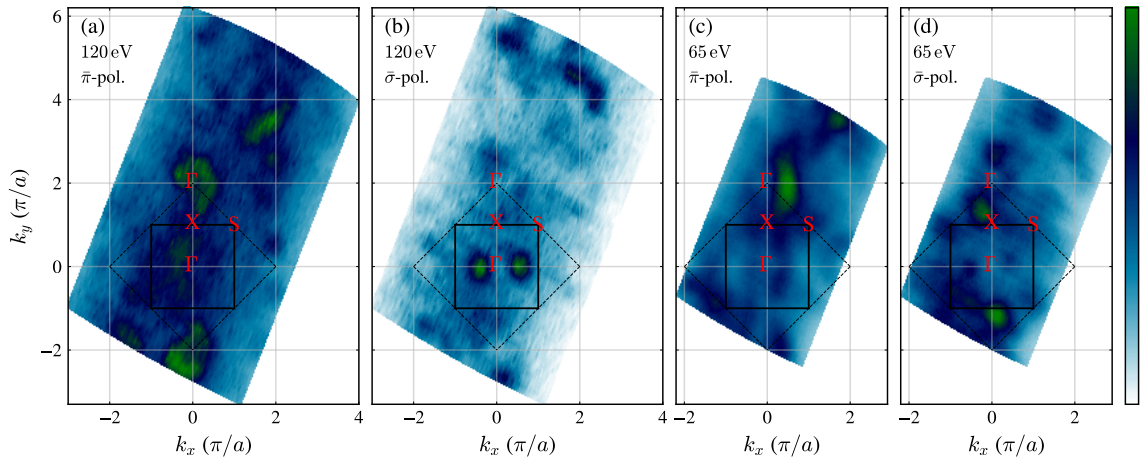


**Fig. B.1**  $(k_x, k_y)$ -map of the  $\mathcal{A}$ -band at  $\omega = -0.5 \text{ eV}$ . Different photon energies and polarisations are used as indicated in the upper left corner. Solid black lines indicate the orthorhombic BZ, while the dashed black lines mark the tetragonal BZ.

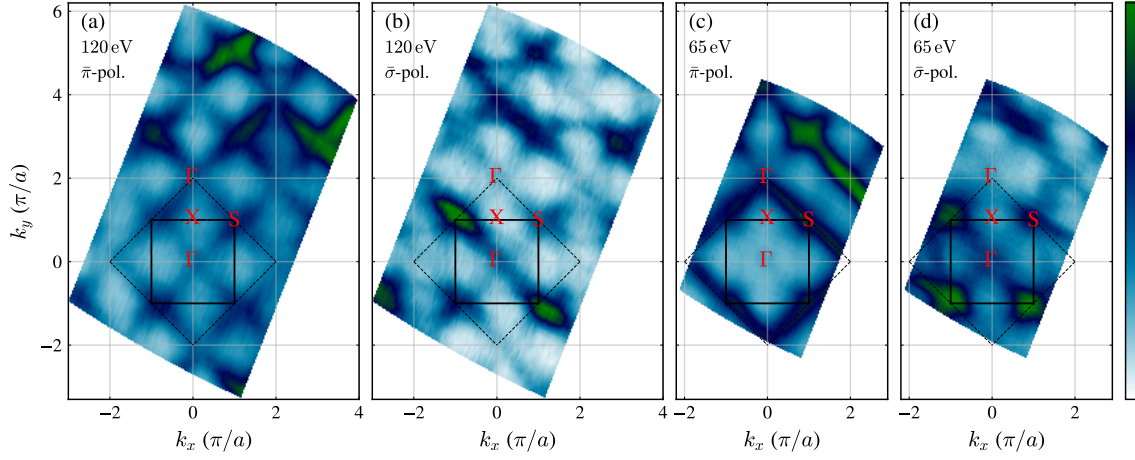


**Fig. B.2** ARPES  $(k_x, k_y)$ -maps at  $\omega = -5.2$  eV, through the oxygen bands. (a, b) are taken at 120 eV photon energy with  $\bar{\pi}$ - and  $\bar{\sigma}$ -polarisation, respectively. (c, d) are recorded with 65 eV photons with both polarisations as well. Solid lines indicate the orthorhombic zone boundary and the dashed line mark the tetragonal BZ.

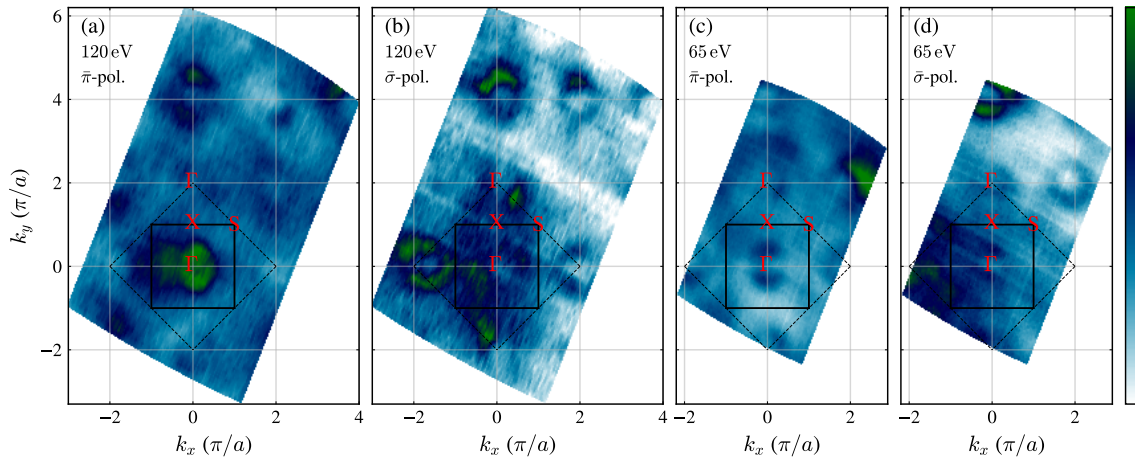


**Fig. B.3** ARPES  $(k_x, k_y)$ -maps at  $\omega = -2.4$  eV, through the  $\mathcal{C}$ -band. Photon energy and polarisations in (a-d) are identical as in Fig. B.2.

# Appendix C

## Drawings PSI sample transportation

items	part	description	material	supplier	art. nr.	CHF/item	CHF tot.
2	1037	Grundplatte	PMMA	UZH			
4	1039	Halter	PMMA	UZH			
8	1026	Distanzhalter M2x10	Stahl verzinkt	Bossard	1545086	0.58	4.64
1	1027 & 1029	Universalgehäuse	several	Distrelec	302859	40.05	40.05
4	1030	Hohe Rändelmutter	Messing	Bossard	1197495	0.93	3.72
8	1701030006	Zylinderkopfschr. M3x6	Stahl verzinkt	UZH			
4	2202050010	Schaftschr. M5x10	Stahl verzinkt	Bossard	1183060	0.09	0.36
28	1001030004	Madenschr. M3x4	Stahl verzinkt	Bossard	1177621	0.07	1.96
							total: 50.73

Table C.1 Part list

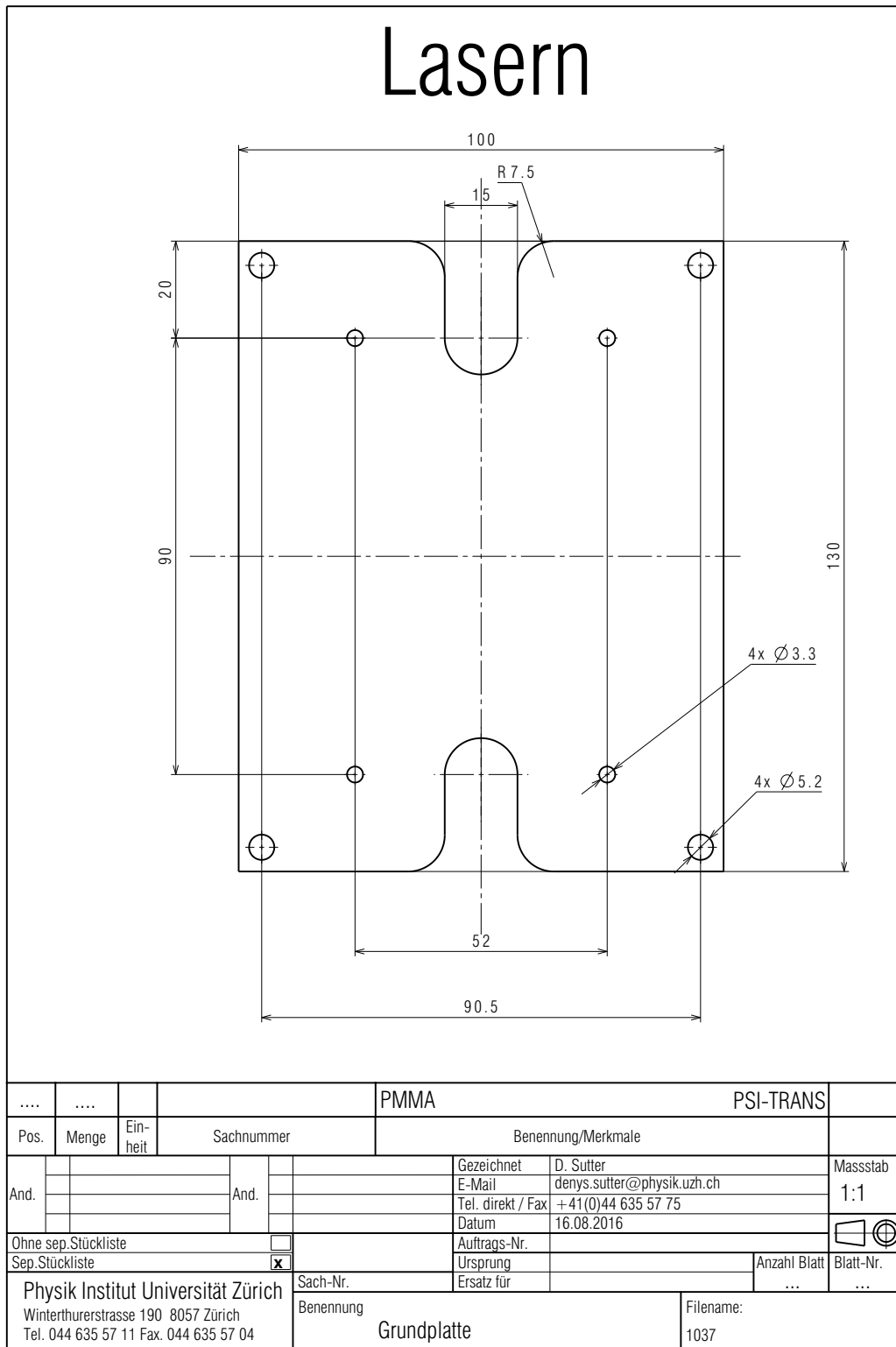


Fig. C.1 Part 1037 drawing

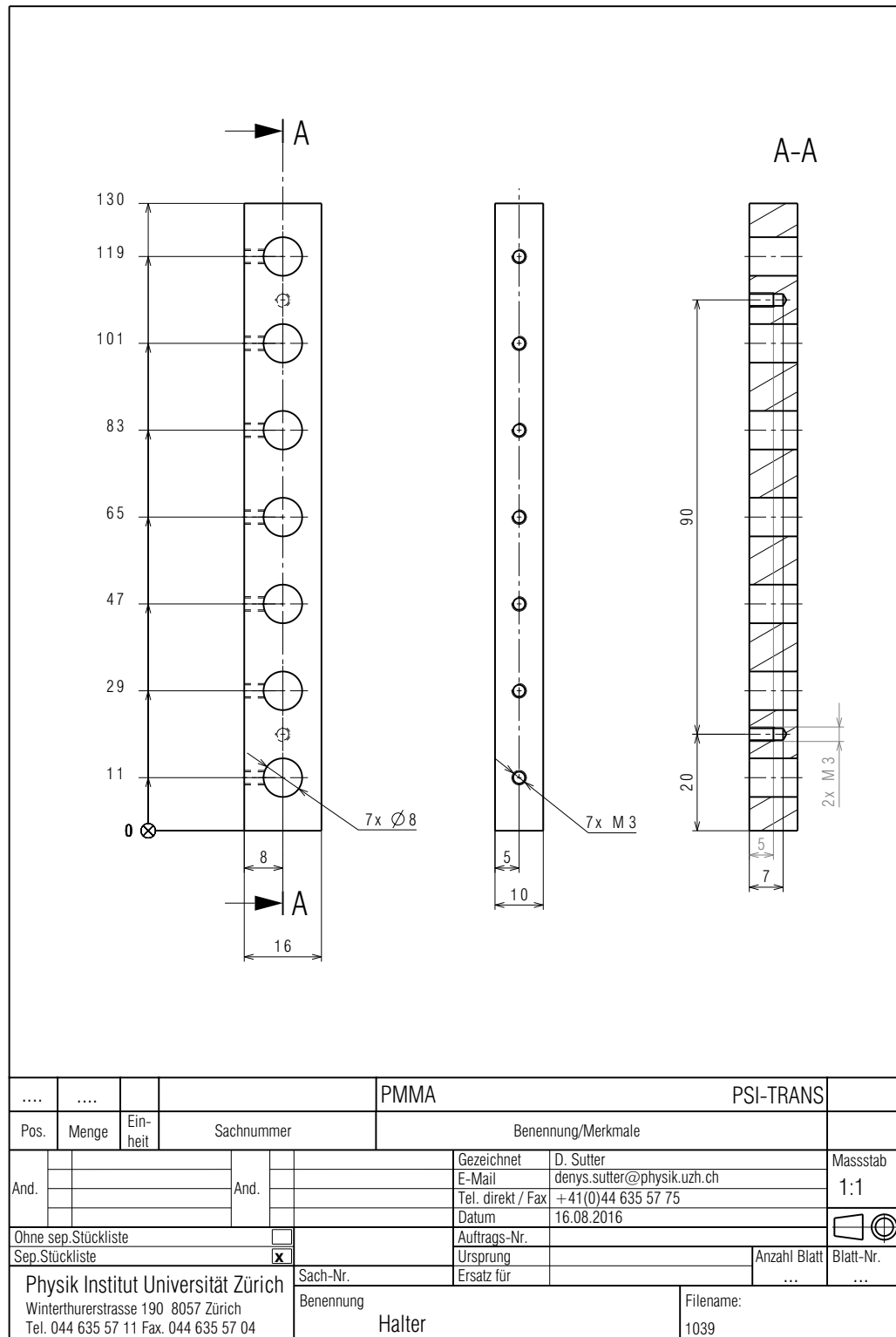
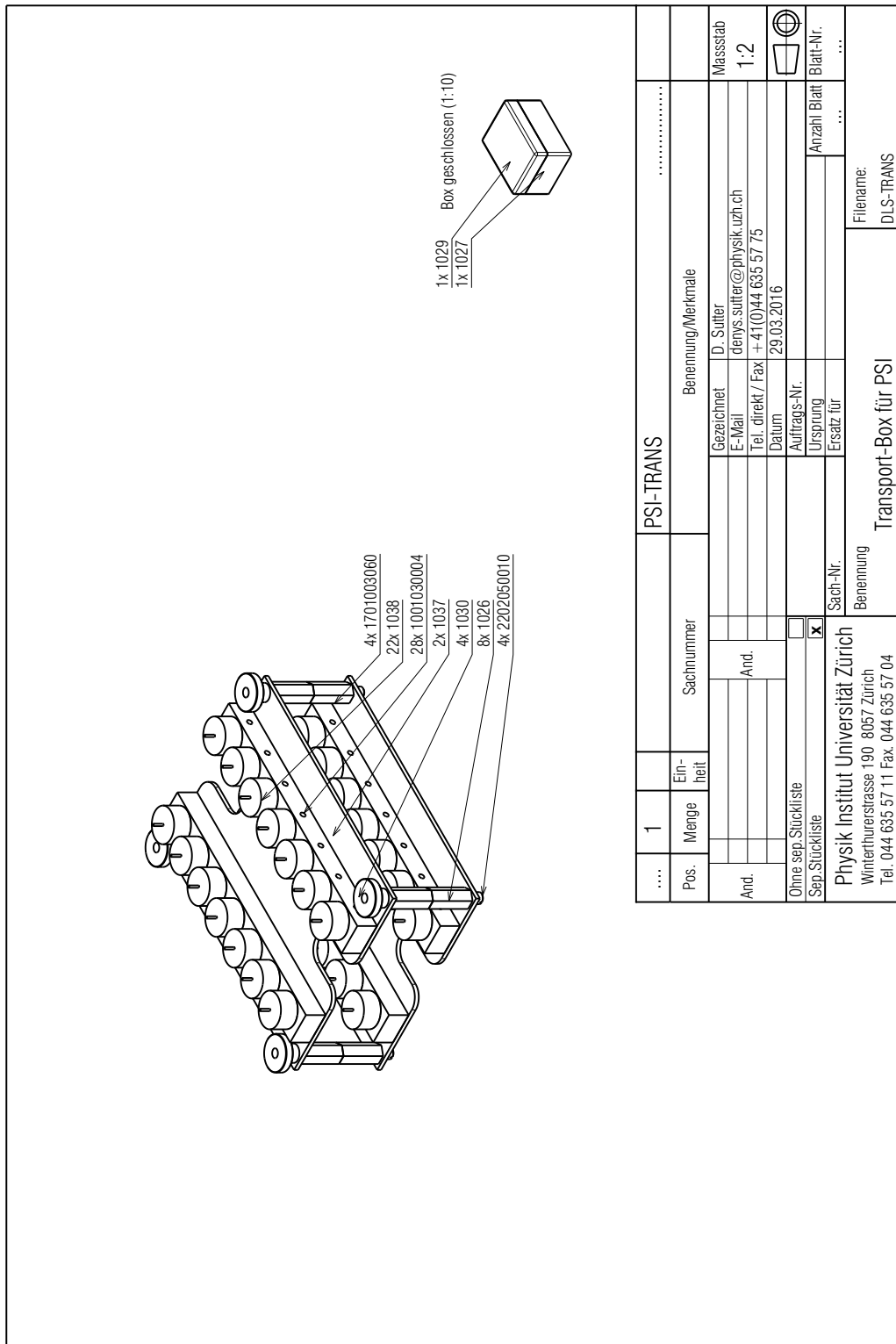


Fig. C.2 Part 1039 drawing

**Fig. C.3** Assembly drawing

# References

- [1] Anderson, P. W. More Is Different. *Science* **177**, 393–396 (1972). URL <http://science.sciencemag.org/content/177/4047/393>.
- [2] Onnes, H. K. The resistance of pure mercury at helium temperatures. *Commun. Phys. Lab. Univ. Leiden* **12**, 120+ (1911).
- [3] Bardeen, J., Cooper, L. N. & Schrieffer, J. R. Microscopic Theory of Superconductivity. *Phys. Rev.* **106**, 162–164 (1957). URL <https://link.aps.org/doi/10.1103/PhysRev.106.162>.
- [4] Bednorz, J. G. & Müller, K. A. Possible high  $T_c$  superconductivity in the Ba-La-Cu-O system. *Zeitschrift für Physik B Condensed Matter* **64**, 189–193 (1986). URL <https://doi.org/10.1007/BF01303701>.
- [5] Wu, M. K. *et al.* Superconductivity at 93 K in a new mixed-phase Y-Ba-Cu-O compound system at ambient pressure. *Phys. Rev. Lett.* **58**, 908–910 (1987). URL <https://link.aps.org/doi/10.1103/PhysRevLett.58.908>.
- [6] Cava, R. J. *et al.* Bulk superconductivity at 91 K in single-phase oxygen-deficient perovskite  $\text{Ba}_2\text{YC}_{3}\text{O}_{9-\delta}$ . *Phys. Rev. Lett.* **58**, 1676–1679 (1987). URL <https://link.aps.org/doi/10.1103/PhysRevLett.58.1676>.
- [7] Dagotto, E., Hotta, T. & Moreo, A. Colossal magnetoresistant materials: the key role of phase separation. *Physics Reports* **344**, 1 – 153 (2001). URL <http://www.sciencedirect.com/science/article/pii/S0370157300001216>.
- [8] Salamon, M. B. & Jaime, M. The physics of manganites: Structure and transport. *Rev. Mod. Phys.* **73**, 583–628 (2001).
- [9] Terasaki, I., Sasago, Y. & Uchinokura, K. Large thermoelectric power in  $\text{NaCo}_2\text{O}_4$  single crystals. *Phys. Rev. B* **56**, R12685–R12687 (1997). URL <https://link.aps.org/doi/10.1103/PhysRevB.56.R12685>.
- [10] Lee, M. *et al.* Large enhancement of the thermopower in  $\text{Na}_x\text{CoO}_2$  at high Na doping. *Nature Materials* **5**, 537–540 (2006). URL <https://doi.org/10.1038/nmat1669>.
- [11] Takada, K. *et al.* Superconductivity in two-dimensional  $\text{CoO}_2$  layers. *Nature* **422**, 53–55 (2003). URL <https://doi.org/10.1038/nature01450>.

- [12] Wigner, E. Effects of the electron interaction on the energy levels of electrons in metals. *Trans. Faraday Soc.* **34**, 678–685 (1938). URL <http://dx.doi.org/10.1039/TF9383400678>.
- [13] Mott, N. F. Metal-Insulator Transition. *Rev. Mod. Phys.* **40**, 677–683 (1968). URL <https://link.aps.org/doi/10.1103/RevModPhys.40.677>.
- [14] Gibert, M., Zubko, P., Scherwitzl, R., Íñiguez, J. & Triscone, J.-M. Exchange bias in  $\text{LaNiO}_3$ – $\text{LaMnO}_3$  superlattices. *Nature Materials* **11**, 195–198 (2012). URL <https://doi.org/10.1038/nmat3224>.
- [15] Middey, S. *et al.* Physics of Ultrathin Films and Heterostructures of Rare-Earth Nickelates. *Annual Review of Materials Research* **46**, 305–334 (2016). URL <https://doi.org/10.1146/annurev-matsci-070115-032057>.
- [16] Mott, N. F. The Basis of the Electron Theory of Metals, with Special Reference to the Transition Metals. *Proceedings of the Physical Society. Section A* **62**, 416 (1949). URL <http://stacks.iop.org/0370-1298/62/i=7/a=303>.
- [17] Imada, M., Fujimori, A. & Tokura, Y. Metal-insulator transitions. *Rev. Mod. Phys.* **70**, 1039–1263 (1998). URL <https://link.aps.org/doi/10.1103/RevModPhys.70.1039>.
- [18] Dagotto, E. Correlated electrons in high-temperature superconductors. *Rev. Mod. Phys.* **66**, 763–840 (1994). URL <https://link.aps.org/doi/10.1103/RevModPhys.66.763>.
- [19] *et al.*, P. A. L. Doping a Mott insulator: Physics of high-temperature superconductivity. *Rev. Mod. Phys.* **78**, 17–85 (2006).
- [20] Georges, A., Medici, L. d. & Mravlje, J. Strong correlations from Hund's coupling. *Annual Review of Condensed Matter Physics* **4**, 137–178 (2013). URL <https://doi.org/10.1146/annurev-conmatphys-020911-125045>.
- [21] Kamihara, Y., Watanabe, T., Hirano, M. & Hosono, H. Iron-based layered superconductor  $\text{La}[\text{O}_{1-x}\text{F}_x]\text{FeAs}$  ( $x = 0.05 – 0.12$ ) with  $T_c = 26\text{ K}$ . *Journal of the American Chemical Society* **130**, 3296–3297 (2008).
- [22] de' Medici, L., Hassan, S. R., Capone, M. & Dai, X. Orbital-Selective Mott Transition out of Band Degeneracy Lifting. *Phys. Rev. Lett.* **102**, 126401 (2009). URL <https://link.aps.org/doi/10.1103/PhysRevLett.102.126401>.
- [23] de' Medici, L., Mravlje, J. & Georges, A. Janus-Faced Influence of Hund's Rule Coupling in Strongly Correlated Materials. *Phys. Rev. Lett.* **107**, 256401 (2011). URL <https://link.aps.org/doi/10.1103/PhysRevLett.107.256401>.
- [24] de' Medici, L. Hund's coupling and its key role in tuning multiorbital correlations. *Phys. Rev. B* **83**, 205112 (2011). URL <https://link.aps.org/doi/10.1103/PhysRevB.83.205112>.
- [25] Maeno, Y. *et al.* Superconductivity in a layered perovskite without copper. *Nature* **372**, 532 (1994). URL <https://doi.org/10.1038/372532a0>.

- [26] Eom, C. B. *et al.* Single-Crystal Epitaxial Thin Films of the Isotropic Metallic Oxides  $\text{Sr}_{1-x}\text{Ca}_x\text{RuO}_3$  ( $0 \leq x \leq 1$ ). *Science* **258**, 1766–1769 (1992). URL <http://science.sciencemag.org/content/258/5089/1766>.
- [27] Kennedy, B. J. & Hunter, B. A. High-temperature phases of  $\text{SrRuO}_3$ . *Phys. Rev. B* **58**, 653–658 (1998). URL <https://link.aps.org/doi/10.1103/PhysRevB.58.653>.
- [28] Capogna, L. *et al.* Sensitivity to Disorder of the Metallic State in the Ruthenates. *Phys. Rev. Lett.* **88**, 076602 (2002). URL <https://link.aps.org/doi/10.1103/PhysRevLett.88.076602>.
- [29] Allen, P. B. *et al.* Transport properties, thermodynamic properties, and electronic structure of  $\text{SrRuO}_3$ . *Phys. Rev. B* **53**, 4393–4398 (1996). URL <https://link.aps.org/doi/10.1103/PhysRevB.53.4393>.
- [30] Kostic, P. *et al.* Non-Fermi-Liquid Behavior of  $\text{SrRuO}_3$ : Evidence from Infrared Conductivity. *Phys. Rev. Lett.* **81**, 2498–2501 (1998). URL <https://link.aps.org/doi/10.1103/PhysRevLett.81.2498>.
- [31] Dodge, J. S. *et al.* Low-Frequency Crossover of the Fractional Power-Law Conductivity in  $\text{SrRuO}_3$ . *Phys. Rev. Lett.* **85**, 4932–4935 (2000). URL <https://link.aps.org/doi/10.1103/PhysRevLett.85.4932>.
- [32] Okamoto, J. *et al.* Correlation effects in the electronic structure of  $\text{SrRuO}_3$ . *Phys. Rev. B* **60**, 2281–2285 (1999). URL <https://link.aps.org/doi/10.1103/PhysRevB.60.2281>.
- [33] Fang, Z. *et al.* The Anomalous Hall Effect and Magnetic Monopoles in Momentum Space. *Science* **302**, 92–95 (2003). URL <http://science.sciencemag.org/content/302/5642/92>.
- [34] Shai, D. E. *et al.* Quasiparticle Mass Enhancement and Temperature Dependence of the Electronic Structure of Ferromagnetic  $\text{SrRuO}_3$  Thin Films. *Phys. Rev. Lett.* **110**, 087004 (2013). URL <https://link.aps.org/doi/10.1103/PhysRevLett.110.087004>.
- [35] Anisimov, V., Nekrasov, I., Kondakov, D., Rice, T. & Sigrist, M. Orbital-selective Mott-insulator transition in  $\text{Ca}_{2-x}\text{Sr}_x\text{RuO}_4$ . *The European Physical Journal B - Condensed Matter and Complex Systems* **25**, 191–201 (2002). URL <https://doi.org/10.1140/epjb/e20020021>.
- [36] Zayak, A. T., Huang, X., Neaton, J. B. & Rabe, K. M. Structural, electronic, and magnetic properties of  $\text{SrRuO}_3$  under epitaxial strain. *Phys. Rev. B* **74**, 094104 (2006). URL <https://link.aps.org/doi/10.1103/PhysRevB.74.094104>.
- [37] Klein, L., Antognazza, L., Geballe, T. H., Beasley, M. R. & Kapitulnik, A. Possible non-Fermi-liquid behavior of  $\text{CaRuO}_3$ . *Phys. Rev. B* **60**, 1448–1451 (1999). URL <https://link.aps.org/doi/10.1103/PhysRevB.60.1448>.
- [38] Lee, Y. S. *et al.* Non-Fermi liquid behavior and scaling of the low-frequency suppression in the optical conductivity spectra of  $\text{CaRuO}_3$ . *Phys. Rev. B* **66**, 041104 (2002). URL <https://link.aps.org/doi/10.1103/PhysRevB.66.041104>.

- [39] Shepard, M., McCall, S., Cao, G. & Crow, J. E. Thermodynamic properties of perovskite ARuO<sub>3</sub> (A=Ca, Sr, and Ba) single crystals. *Journal of Applied Physics* **81**, 4978–4980 (1997). URL <https://doi.org/10.1063/1.365018>.
- [40] Cao, G., Korneta, O., Chikara, S., DeLong, L. & Schlottmann, P. Non-Fermi-liquid behavior in single-crystal CaRuO<sub>3</sub>: Comparison to ferromagnetic SrRuO<sub>3</sub>. *Solid State Communications* **148**, 305 – 309 (2008). URL <http://www.sciencedirect.com/science/article/pii/S0038109808005139>.
- [41] Werner, P., Gull, E., Troyer, M. & Millis, A. J. Spin Freezing Transition and Non-Fermi-Liquid Self-Energy in a Three-Orbital Model. *Phys. Rev. Lett.* **101**, 166405 (2008). URL <https://link.aps.org/doi/10.1103/PhysRevLett.101.166405>.
- [42] Koster, G. *et al.* Structure, physical properties, and applications of SrRuO<sub>3</sub> thin films. *Rev. Mod. Phys.* **84**, 253–298 (2012). URL <https://link.aps.org/doi/10.1103/RevModPhys.84.253>.
- [43] Crawford, M. K. *et al.* Structure and magnetism of single crystal Sr<sub>4</sub>Ru<sub>3</sub>O<sub>10</sub> : A ferromagnetic triple-layer ruthenate. *Phys. Rev. B* **65**, 214412 (2002). URL <https://link.aps.org/doi/10.1103/PhysRevB.65.214412>.
- [44] Mao, Z. Q., Zhou, M., Hooper, J., Golub, V. & O'Connor, C. J. Phase Separation in the Itinerant Metamagnetic Transition of Sr<sub>4</sub>Ru<sub>3</sub>O<sub>10</sub>. *Phys. Rev. Lett.* **96**, 077205 (2006). URL <https://link.aps.org/doi/10.1103/PhysRevLett.96.077205>.
- [45] Jo, Y. J. *et al.* Orbital-dependent metamagnetic response in Sr<sub>4</sub>Ru<sub>3</sub>O<sub>10</sub>. *Phys. Rev. B* **75**, 094413 (2007). URL <https://link.aps.org/doi/10.1103/PhysRevB.75.094413>.
- [46] Fobes, D. *et al.* Anisotropy of magnetoresistivities in Sr<sub>4</sub>Ru<sub>3</sub>O<sub>10</sub>: Evidence for an orbital-selective metamagnetic transition. *Phys. Rev. B* **81**, 172402 (2010). URL <https://link.aps.org/doi/10.1103/PhysRevB.81.172402>.
- [47] Zheng, H. *et al.* Observation of a pressure-induced transition from interlayer ferromagnetism to intralayer antiferromagnetism in Sr<sub>4</sub>Ru<sub>3</sub>O<sub>10</sub>. *Phys. Rev. B* **98**, 064418 (2018). URL <https://link.aps.org/doi/10.1103/PhysRevB.98.064418>.
- [48] Fobes, D. *et al.* Phase diagram of the electronic states of trilayered ruthenate Sr<sub>4</sub>Ru<sub>3</sub>O<sub>10</sub>. *Phys. Rev. B* **75**, 094429 (2007). URL <https://link.aps.org/doi/10.1103/PhysRevB.75.094429>.
- [49] Cao, G. *et al.* Competing ground states in triple-layered Sr<sub>4</sub>Ru<sub>3</sub>O<sub>10</sub> : Verging on itinerant ferromagnetism with critical fluctuations. *Phys. Rev. B* **68**, 174409 (2003). URL <https://link.aps.org/doi/10.1103/PhysRevB.68.174409>.
- [50] Lin, X., Bondarenko, V., Cao, G. & Brill, J. Specific heat of Sr<sub>4</sub>Ru<sub>3</sub>O<sub>10</sub>. *Solid State Communications* **130**, 151 – 154 (2004). URL <http://www.sciencedirect.com/science/article/pii/S003810980400105X>.
- [51] Chikara, S. *et al.* Borderline magnetism in Sr<sub>4</sub>Ru<sub>3</sub>O<sub>10</sub>: Impact of La and Ca doping on itinerant ferromagnetism and metamagnetism. *Phys. Rev. B* **73**, 224420 (2006). URL <https://link.aps.org/doi/10.1103/PhysRevB.73.224420>.

- [52] Kikugawa, N., Winfried Rost, A., William Hicks, C., John Schofield, A. & Peter Mackenzie, A.  $\text{Ca}_3\text{Ru}_2\text{O}_7$ : Density Wave Formation and Quantum Oscillations in the Hall Resistivity. *Journal of the Physical Society of Japan* **79**, 024704 (2010). URL <https://doi.org/10.1143/JPSJ.79.024704>.
- [53] Baumberger, F. *et al.* Nested Fermi Surface and Electronic Instability in  $\text{Ca}_3\text{Ru}_2\text{O}_7$ . *Phys. Rev. Lett.* **96**, 107601 (2006). URL <https://link.aps.org/doi/10.1103/PhysRevLett.96.107601>.
- [54] Fradkin, E., Kivelson, S. A., Lawler, M. J., Eisenstein, J. P. & Mackenzie, A. P. Nematic Fermi Fluids in Condensed Matter Physics. *Annual Review of Condensed Matter Physics* **1**, 153–178 (2010). URL <https://doi.org/10.1146/annurev-conmatphys-070909-103925>.
- [55] Grigera, S. A. *et al.* Magnetic Field-Tuned Quantum Criticality in the Metallic Ruthenate  $\text{Sr}_3\text{Ru}_2\text{O}_7$ . *Science* **294**, 329–332 (2001). URL <http://science.sciencemag.org/content/294/5541/329>.
- [56] Perry, R. S. *et al.* Metamagnetism and Critical Fluctuations in High Quality Single Crystals of the Bilayer Ruthenate  $\text{Sr}_3\text{Ru}_2\text{O}_7$ . *Phys. Rev. Lett.* **86**, 2661–2664 (2001). URL <https://link.aps.org/doi/10.1103/PhysRevLett.86.2661>.
- [57] Tamai, A. *et al.* Fermi Surface and van Hove Singularities in the Itinerant Metamagnet  $\text{Sr}_3\text{Ru}_2\text{O}_7$ . *Phys. Rev. Lett.* **101**, 026407 (2008). URL <https://link.aps.org/doi/10.1103/PhysRevLett.101.026407>.
- [58] Allan, M. P. *et al.* Formation of heavy d-electron quasiparticles in  $\text{Sr}_3\text{Ru}_2\text{O}_7$ . *New Journal of Physics* **15**, 063029 (2013). URL <http://stacks.iop.org/1367-2630/15/i=6/a=063029>.
- [59] Borzi, R. A. *et al.* Formation of a Nematic Fluid at High Fields in  $\text{Sr}_3\text{Ru}_2\text{O}_7$ . *Science* **315**, 214–217 (2007). URL <http://science.sciencemag.org/content/315/5809/214>.
- [60] Lester, C. *et al.* Field-tunable spin-density-wave phases in  $\text{Sr}_3\text{Ru}_2\text{O}_7$ . *Nature Materials* **14**, 373 (2015). URL <https://doi.org/10.1038/nmat4181>.
- [61] Cao, G., McCall, S., Crow, J. E. & Guertin, R. P. Observation of a Metallic Antiferromagnetic Phase and Metal to Non-metal Transition in  $\text{Ca}_3\text{Ru}_2\text{O}_7$ . *Phys. Rev. Lett.* **78**, 1751–1754 (1997). URL <https://link.aps.org/doi/10.1103/PhysRevLett.78.1751>.
- [62] Yoshida, Y. *et al.* Crystal and magnetic structure of  $\text{Ca}_3\text{Ru}_2\text{O}_7$ . *Phys. Rev. B* **72**, 054412 (2005). URL <https://link.aps.org/doi/10.1103/PhysRevB.72.054412>.
- [63] Yoshida, Y. *et al.* Quasi-two-dimensional metallic ground state of  $\text{Ca}_3\text{Ru}_2\text{O}_7$ . *Phys. Rev. B* **69**, 220411 (2004). URL <https://link.aps.org/doi/10.1103/PhysRevB.69.220411>.
- [64] Qu, Z. *et al.* Complex electronic states in double-layered ruthenates  $(\text{Sr}_{1-x}\text{Ca}_x)_3\text{Ru}_2\text{O}_7$ . *Phys. Rev. B* **80**, 115130 (2009). URL <https://link.aps.org/doi/10.1103/PhysRevB.80.115130>.

- [65] Xing, H. *et al.* Existence of electron and hole pockets and partial gap opening in the correlated semimetal  $\text{Ca}_3\text{Ru}_2\text{O}_7$ . *Phys. Rev. B* **97**, 041113 (2018). URL <https://link.aps.org/doi/10.1103/PhysRevB.97.041113>.
- [66] McCall, S., Cao, G. & Crow, J. E. Impact of magnetic fields on anisotropy in  $\text{Ca}_3\text{Ru}_2\text{O}_7$ . *Phys. Rev. B* **67**, 094427 (2003). URL <https://link.aps.org/doi/10.1103/PhysRevB.67.094427>.
- [67] Cao, G., Balicas, L., Xin, Y., Crow, J. E. & Nelson, C. S. Quantum oscillations, colossal magnetoresistance, and the magnetoelastic interaction in bilayered  $\text{Ca}_3\text{Ru}_2\text{O}_7$ . *Phys. Rev. B* **67**, 184405 (2003). URL <https://link.aps.org/doi/10.1103/PhysRevB.67.184405>.
- [68] Ohmichi, E., Yoshida, Y., Ikeda, S. I., Shirakawa, N. & Osada, T. Colossal magnetoresistance accompanying a structural transition in a highly two-dimensional metallic state of  $\text{Ca}_3\text{Ru}_2\text{O}_7$ . *Phys. Rev. B* **70**, 104414 (2004). URL <https://link.aps.org/doi/10.1103/PhysRevB.70.104414>.
- [69] Lin, X. N., Zhou, Z. X., Durairaj, V., Schlottmann, P. & Cao, G. Colossal Magnetoresistance by Avoiding a Ferromagnetic State in the Mott System  $\text{Ca}_3\text{Ru}_2\text{O}_7$ . *Phys. Rev. Lett.* **95**, 017203 (2005). URL <https://link.aps.org/doi/10.1103/PhysRevLett.95.017203>.
- [70] Singh, D. J. & Auluck, S. Electronic Structure and Bulk Spin-Valve Behavior in  $\text{Ca}_3\text{Ru}_2\text{O}_7$ . *Phys. Rev. Lett.* **96**, 097203 (2006). URL <https://link.aps.org/doi/10.1103/PhysRevLett.96.097203>.
- [71] Bao, W., Mao, Z. Q., Qu, Z. & Lynn, J. W. Spin Valve Effect and Magnetoresistivity in Single Crystalline  $\text{Ca}_3\text{Ru}_2\text{O}_7$ . *Phys. Rev. Lett.* **100**, 247203 (2008). URL <https://link.aps.org/doi/10.1103/PhysRevLett.100.247203>.
- [72] Cao, G., Durairaj, V., Chikara, S., DeLong, L. E. & Schlottmann, P. Observation of Strong Spin Valve Effect in Bulk  $\text{Ca}_3(\text{Ru}_{1-x}\text{Cr}_x)_2\text{O}_7$ . *Phys. Rev. Lett.* **100**, 016604 (2008). URL <https://link.aps.org/doi/10.1103/PhysRevLett.100.016604>.
- [73] Nakatsuji, S. & Maeno, Y. Switching of magnetic coupling by a structural symmetry change near the Mott transition in  $\text{Ca}_{2-x}\text{Sr}_x\text{RuO}_4$ . *Phys. Rev. B* **62**, 6458–6466 (2000). URL <https://link.aps.org/doi/10.1103/PhysRevB.62.6458>.
- [74] Nakatsuji, S. & Maeno, Y. Quasi-Two-Dimensional Mott Transition System  $\text{Ca}_{2-x}\text{Sr}_x\text{RuO}_4$ . *Phys. Rev. Lett.* **84**, 2666–2669 (2000). URL <https://link.aps.org/doi/10.1103/PhysRevLett.84.2666>.
- [75] Nakatsuji, S. *et al.* Heavy-Mass Fermi Liquid near a Ferromagnetic Instability in Layered Ruthenates. *Phys. Rev. Lett.* **90**, 137202 (2003). URL <https://link.aps.org/doi/10.1103/PhysRevLett.90.137202>.
- [76] Carlo, J. P. *et al.* New magnetic phase diagram of  $(\text{Sr}, \text{Ca})_2\text{RuO}_4$ . *Nature Materials* **11**, 323 (2012). URL <https://doi.org/10.1038/nmat3236>.

- [77] Braden, M., Moudden, A., Nishizaki, S., Maeno, Y. & Fujita, T. Structural analysis of  $\text{Sr}_2\text{RuO}_4$ . *Physica C: Superconductivity* **273**, 248 – 254 (1997). URL <http://www.sciencedirect.com/science/article/pii/S0921453496006375>.
- [78] Braden, M., André, G., Nakatsuji, S. & Maeno, Y. Crystal and magnetic structure of  $\text{Ca}_2\text{RuO}_4$ : Magnetoelastic coupling and the metal-insulator transition. *Phys. Rev. B* **58**, 847–861 (1998). URL <https://link.aps.org/doi/10.1103/PhysRevB.58.847>.
- [79] Damascelli, A. *et al.* Fermi surface, surface states, and surface reconstruction in  $\text{Sr}_2\text{RuO}_4$ . *Phys. Rev. Lett.* **85**, 5194–5197 (2000). URL <https://link.aps.org/doi/10.1103/PhysRevLett.85.5194>.
- [80] Mackenzie, A. P. & Maeno, Y. The superconductivity of  $\text{Sr}_2\text{RuO}_4$  and the physics of spin-triplet pairing. *Rev. Mod. Phys.* **75**, 657–712 (2003). URL <https://link.aps.org/doi/10.1103/RevModPhys.75.657>.
- [81] Rice, T. & Sigrist, M.  $\text{Sr}_2\text{RuO}_4$ : an electronic analogue of  ${}^3\text{He}$ ? *Journal of Physics: Condensed Matter* **7**, L643 (1995). URL <http://stacks.iop.org/0953-8984/7/i=47/a=002>.
- [82] Ishida, K. *et al.* Spin-triplet superconductivity in  $\text{Sr}_2\text{RuO}_4$  identified by  ${}^{17}\text{O}$  Knight shift. *Nature* **396**, 658 (1998). URL <https://doi.org/10.1038/25315>.
- [83] Hicks, C. W. *et al.* Strong Increase of  $T_c$  of  $\text{Sr}_2\text{RuO}_4$  Under Both Tensile and Compressive Strain. *Science* **344**, 283–285 (2014). URL <http://science.sciencemag.org/content/344/6181/283>.
- [84] Steppke, A. *et al.* Strong peak in  $T_c$  of  $\text{Sr}_2\text{RuO}_4$  under uniaxial pressure. *Science* **355** (2017). URL <http://science.sciencemag.org/content/355/6321/eaaf9398>.
- [85] Liu, Y.-C., Zhang, F.-C., Rice, T. M. & Wang, Q.-H. Theory of the evolution of superconductivity in  $\text{Sr}_2\text{RuO}_4$  under anisotropic strain. *npj Quantum Materials* **2**, 12 (2017). URL <https://doi.org/10.1038/s41535-017-0014-y>.
- [86] Barber, M. E., Gibbs, A. S., Maeno, Y., Mackenzie, A. P. & Hicks, C. W. Resistivity in the Vicinity of a van Hove Singularity:  $\text{Sr}_2\text{RuO}_4$  under Uniaxial Pressure. *Phys. Rev. Lett.* **120**, 076602 (2018). URL <https://link.aps.org/doi/10.1103/PhysRevLett.120.076602>.
- [87] Maeno, Y., Kittaka, S., Nomura, T., Yonezawa, S. & Ishida, K. Evaluation of Spin-Triplet Superconductivity in  $\text{Sr}_2\text{RuO}_4$ . *Journal of the Physical Society of Japan* **81**, 011009 (2012). URL <https://doi.org/10.1143/JPSJ.81.011009>.
- [88] Mackenzie, A. P., Scaffidi, T., Hicks, C. W. & Maeno, Y. Even odder after twenty-three years: the superconducting order parameter puzzle of  $\text{Sr}_2\text{RuO}_4$ . *npj Quantum Materials* **2**, 40 (2017). URL <https://doi.org/10.1038/s41535-017-0045-4>.
- [89] Mackenzie, A. P. *et al.* Quantum Oscillations in the Layered Perovskite Superconductor  $\text{Sr}_2\text{RuO}_4$ . *Phys. Rev. Lett.* **76**, 3786–3789 (1996). URL <https://link.aps.org/doi/10.1103/PhysRevLett.76.3786>.

- [90] Oguchi, T. Electronic band structure of the superconductor  $\text{Sr}_2\text{RuO}_4$ . *Phys. Rev. B* **51**, 1385–1388 (1995).
- [91] Wang, Z. *et al.* Quasiparticle interference and strong electron-mode coupling in the quasi-one-dimensional bands of  $\text{Sr}_2\text{RuO}_4$ . *Nature Physics* **13**, 799 (2017). URL <https://doi.org/10.1038/nphys4107>.
- [92] Bergemann, C., Julian, S. R., Mackenzie, A. P., NishiZaki, S. & Maeno, Y. Detailed Topography of the Fermi Surface of  $\text{Sr}_2\text{RuO}_4$ . *Phys. Rev. Lett.* **84**, 2662–2665 (2000). URL <https://link.aps.org/doi/10.1103/PhysRevLett.84.2662>.
- [93] Damascelli, A. *et al.* Fermi surface of  $\text{Sr}_2\text{RuO}_4$  from angle resolved photoemission. *Journal of Electron Spectroscopy and Related Phenomena* **114-116**, 641 – 646 (2001). URL <http://www.sciencedirect.com/science/article/pii/S036820480000356X>, proceeding of the Eight International Conference on Electronic Spectroscopy and Structure.,
- [94] Puchkov, A. V., Shen, Z.-X., Kimura, T. & Tokura, Y. ARPES results on  $\text{Sr}_2\text{RuO}_4$  : Fermi surface revisited. *Phys. Rev. B* **58**, R13322–R13325 (1998). URL <https://link.aps.org/doi/10.1103/PhysRevB.58.R13322>.
- [95] Lee, J. S., Moon, S. J., Noh, T. W., Nakatsuji, S. & Maeno, Y. Orbital-Selective Mass Enhancements in Multiband  $\text{Ca}_{2-x}\text{Sr}_x\text{RuO}_4$  Systems Analyzed by the Extended Drude Model. *Phys. Rev. Lett.* **96**, 057401 (2006). URL <https://link.aps.org/doi/10.1103/PhysRevLett.96.057401>.
- [96] Liebsch, A. & Ishida, H. Subband filling and Mott transition in  $\text{Ca}_{2-x}\text{Sr}_x\text{RuO}_4$ . *Phys. Rev. Lett.* **98**, 216403 (2007). URL <https://link.aps.org/doi/10.1103/PhysRevLett.98.216403>.
- [97] Neupane, M. *et al.* Observation of a Novel Orbital Selective Mott Transition in  $\text{Ca}_{1.8}\text{Sr}_{0.2}\text{RuO}_4$ . *Phys. Rev. Lett.* **103**, 097001 (2009). URL <https://link.aps.org/doi/10.1103/PhysRevLett.103.097001>.
- [98] Shimoyamada, A. *et al.* Strong Mass Renormalization at a Local Momentum Space in Multiorbital  $\text{Ca}_{1.8}\text{Sr}_{0.2}\text{RuO}_4$ . *Phys. Rev. Lett.* **102**, 086401 (2009). URL <https://link.aps.org/doi/10.1103/PhysRevLett.102.086401>.
- [99] Gorelov, E. *et al.* Nature of the Mott Transition in  $\text{Ca}_2\text{RuO}_4$ . *Phys. Rev. Lett.* **104**, 226401 (2010). URL <https://link.aps.org/doi/10.1103/PhysRevLett.104.226401>.
- [100] Wang, S.-C. *et al.* Fermi Surface Topology of  $\text{Ca}_{1.5}\text{Sr}_{0.5}\text{RuO}_4$  Determined by Angle-Resolved Photoelectron Spectroscopy. *Phys. Rev. Lett.* **93**, 177007 (2004). URL <https://link.aps.org/doi/10.1103/PhysRevLett.93.177007>.
- [101] Uruma, M. *et al.* *arXiv:0711.2160* (2007). URL <https://arxiv.org/abs/0711.2160>.
- [102] Steffens, P. *et al.* Magnetic excitations in the metallic single-layer ruthenates  $\text{Ca}_{2-x}\text{Sr}_x\text{RuO}_4$  studied by inelastic neutron scattering. *Phys. Rev. B* **83**, 054429 (2011). URL <https://link.aps.org/doi/10.1103/PhysRevB.83.054429>.

- [103] Friedt, O. *et al.* Structural and magnetic aspects of the metal-insulator transition in  $\text{Ca}_{2-x}\text{Sr}_x\text{RuO}_4$ . *Phys. Rev. B* **63**, 174432 (2001). URL <https://link.aps.org/doi/10.1103/PhysRevB.63.174432>.
- [104] Cao, G., McCall, S., Shepard, M., Crow, J. E. & Guertin, R. P. Magnetic and transport properties of single-crystal  $\text{Ca}_2\text{RuO}_4$  Relationship to superconducting  $\text{Sr}_2\text{RuO}_4$ . *Phys. Rev. B* **56**, R2916–R2919 (1997). URL <https://link.aps.org/doi/10.1103/PhysRevB.56.R2916>.
- [105] Alireza, P. L. *et al.* Evidence of superconductivity on the border of quasi-2D ferromagnetism in  $\text{Ca}_2\text{RuO}_4$  at high pressure. *Journal of Physics: Condensed Matter* **22**, 052202 (2010). URL <http://stacks.iop.org/0953-8984/22/i=5/a=052202>.
- [106] Nobukane, H. *et al.* Observation of localized high- $T_c$  superconductivity in a  $\text{Ca}_2\text{RuO}_4$  nanofilm single crystal. *arXiv* (2017). URL <https://arxiv.org/abs/1703.09459>.
- [107] Qi, T. F. *et al.* Negative Volume Thermal Expansion Via Orbital and Magnetic Orders in  $\text{Ca}_2\text{Ru}_{1-x}\text{Cr}_x\text{O}_4$  ( $0 < x < 0.13$ ). *Phys. Rev. Lett.* **105**, 177203 (2010). URL <https://link.aps.org/doi/10.1103/PhysRevLett.105.177203>.
- [108] Sow, C. *et al.* Current-induced strong diamagnetism in the Mott insulator  $\text{Ca}_2\text{RuO}_4$ . *Science* **358**, 1084–1087 (2017). URL <http://science.sciencemag.org/content/358/6366/1084>.
- [109] Souliou, S.-M. *et al.* Raman Scattering from Higgs Mode Oscillations in the Two-Dimensional Antiferromagnet  $\text{Ca}_2\text{RuO}_4$ . *Phys. Rev. Lett.* **119**, 067201 (2017). URL <https://link.aps.org/doi/10.1103/PhysRevLett.119.067201>.
- [110] Jain, A. *et al.* Higgs mode and its decay in a two-dimensional antiferromagnet. *Nature Physics* **13**, 633 EP – (2017). URL <http://dx.doi.org/10.1038/nphys4077>.
- [111] Koga, A., Kawakami, N., Rice, T. M. & Sigrist, M. Orbital-selective Mott transitions in the degenerate Hubbard model. *Phys. Rev. Lett.* **92**, 216402 (2004). URL <https://link.aps.org/doi/10.1103/PhysRevLett.92.216402>.
- [112] Georges, A., Kotliar, G., Krauth, W. & Rozenberg, M. J. Dynamical mean-field theory of strongly correlated fermion systems and the limit of infinite dimensions. *Rev. Mod. Phys.* **68**, 13–125 (1996). URL <https://link.aps.org/doi/10.1103/RevModPhys.68.13>.
- [113] Onida, G., Reining, L. & Rubio, A. Electronic excitations: density-functional versus many-body Green's-function approaches. *Rev. Mod. Phys.* **74**, 601–659 (2002). URL <https://link.aps.org/doi/10.1103/RevModPhys.74.601>.
- [114] Ziman, J. M. *Principles of the Theory of Solids* (Cambridge University Press, 1972), 2 edn.
- [115] Meevasana, W. *et al.* Hierarchy of multiple many-body interaction scales in high-temperature superconductors. *Phys. Rev. B* **75**, 174506 (2007). URL <https://link.aps.org/doi/10.1103/PhysRevB.75.174506>.

- [116] Meevasana, W. *et al.* Extracting the spectral function of the cuprates by a full two-dimensional analysis: Angle-resolved photoemission spectra of  $\text{Bi}_2\text{Sr}_2\text{CuO}_6$ . *Phys. Rev. B* **77**, 104506 (2008). URL <https://link.aps.org/doi/10.1103/PhysRevB.77.104506>.
- [117] Landau, L. Theory of the Superfluidity of Helium II. *Phys. Rev.* **60**, 356–358 (1941). URL <https://link.aps.org/doi/10.1103/PhysRev.60.356>.
- [118] Kordyuk, A. A. *et al.* Bare electron dispersion from experiment: Self-consistent self-energy analysis of photoemission data. *Phys. Rev. B* **71**, 214513 (2005). URL <https://link.aps.org/doi/10.1103/PhysRevB.71.214513>.
- [119] Varma, C., Nussinov, Z. & van Saarloos, W. Singular or non-Fermi liquids. *Physics Reports* **361**, 267 – 417 (2002). URL <http://www.sciencedirect.com/science/article/pii/S0370157301000606>.
- [120] Damascelli, A., Hussain, Z. & Shen, Z.-X. Angle-resolved photoemission studies of the cuprate superconductors. *Rev. Mod. Phys.* **75**, 473–541 (2003). URL <https://link.aps.org/doi/10.1103/RevModPhys.75.473>.
- [121] Deng, X. *et al.* How bad metals turn good: Spectroscopic signatures of resilient quasiparticles. *Phys. Rev. Lett.* **110**, 086401 (2013). URL <https://link.aps.org/doi/10.1103/PhysRevLett.110.086401>.
- [122] Andres, K., Graebner, J. E. & Ott, H. R. 4f-Virtual-Bound-State Formation in  $\text{CeAl}_3$  at Low Temperatures. *Phys. Rev. Lett.* **35**, 1779–1782 (1975). URL <https://link.aps.org/doi/10.1103/PhysRevLett.35.1779>.
- [123] Stewart, G. R. Heavy-fermion systems. *Rev. Mod. Phys.* **56**, 755–787 (1984). URL <https://link.aps.org/doi/10.1103/RevModPhys.56.755>.
- [124] Kadowaki, K. & Woods, S. Universal relationship of the resistivity and specific heat in heavy-Fermion compounds. *Solid State Communications* **58**, 507 – 509 (1986). URL <http://www.sciencedirect.com/science/article/pii/0038109886907854>.
- [125] Rice, M. J. Electron-Electron Scattering in Transition Metals. *Phys. Rev. Lett.* **20**, 1439–1441 (1968). URL <https://link.aps.org/doi/10.1103/PhysRevLett.20.1439>.
- [126] Jacko, A. C., Fjærrestad, J. O. & Powell, B. J. A unified explanation of the Kadowaki–Woods ratio in strongly correlated metals. *Nature Physics* **5**, 422 EP – (2009). URL <https://doi.org/10.1038/nphys1249>.
- [127] Zlatić, V., Monnier, R. & Freericks, J. K. Enhancement of thermal transport in the degenerate periodic Anderson model. *Phys. Rev. B* **78**, 045113 (2008). URL <https://link.aps.org/doi/10.1103/PhysRevB.78.045113>.
- [128] Chang, J. *et al.* Anisotropic breakdown of Fermi liquid quasiparticle excitations in overdoped  $\text{La}_{2-x}\text{Sr}_x\text{CuO}_4$ . *Nature Communications* **4**, 2559 (2013). URL <https://doi.org/10.1038/ncomms3559>.

- [129] Luttinger, J. M. An Exactly Soluble Model of a Many-Fermion System. *Journal of Mathematical Physics* **4**, 1154–1162 (1963). URL <https://doi.org/10.1063/1.1704046>.
- [130] Mattis, D. C. & Lieb, E. H. Exact Solution of a Many-Fermion System and Its Associated Boson Field. *Journal of Mathematical Physics* **6**, 304–312 (1965). URL <https://doi.org/10.1063/1.1704281>.
- [131] Ishii, H. *et al.* Direct observation of Tomonaga–Luttinger-liquid state in carbon nanotubes at low temperatures. *Nature* **426**, 540 EP – (2003). URL <https://doi.org/10.1038/nature02074>.
- [132] Anderson, P. W. Experimental Constraints on the Theory of High- $T_c$  Superconductivity. *Science* **256**, 1526–1531 (1992). URL <http://science.sciencemag.org/content/256/5063/1526>.
- [133] Keimer, B., Kivelson, S. A., Norman, M. R., Uchida, S. & Zaanen, J. From quantum matter to high-temperature superconductivity in copper oxides. *Nature* **518**, 179 EP – (2015). URL <https://doi.org/10.1038/nature14165>.
- [134] Giraldo-Gallo, P. *et al.* Scale-invariant magnetoresistance in a cuprate superconductor. *Science* **361**, 479–481 (2018). URL <http://science.sciencemag.org/content/361/6401/479>.
- [135] Landau, L. D. The theory of a Fermi Liquid. *Soviet Physics JETP* **3** (1957).
- [136] Mott, N. Discussion of the paper by de Boer and Verwey. *Proc. Phys. Soc.* **49**, 72 (1937).
- [137] Mott, N. The basis of the electron theory of metals, with special reference to the transition metals. *Proc. Phys. Soc. London* **62**, 416 (1949).
- [138] Watanabe, S. & Imada, M. Precise Determination of Phase Diagram for Two-Dimensional Hubbard Model with Filling- and Bandwidth-Control Mott Transitions: Grand-Canonical Path-Integral Renormalization Group Approach. *Journal of the Physical Society of Japan* **73**, 1251–1266 (2004). URL <https://doi.org/10.1143/JPSJ.73.1251>.
- [139] Yee, C.-H. & Balents, L. Phase Separation in Doped Mott Insulators. *Phys. Rev. X* **5**, 021007 (2015). URL <https://link.aps.org/doi/10.1103/PhysRevX.5.021007>.
- [140] Xiang, P.-H. *et al.* Room temperature Mott metal-insulator transition and its systematic control in  $\text{Sm}_{1-x}\text{Ca}_x\text{NiO}_3$  thin films. *Applied Physics Letters* **97**, 032114 (2010). URL <https://doi.org/10.1063/1.3467199>.
- [141] Belik, A. A., Shpanchenko, R. V. & Takayama-Muromachi, E. Carrier-doping metal-insulator transition in solid solutions of  $\text{CdVO}_3$ - $\text{YVO}_3$ . *Journal of Magnetism and Magnetic Materials* **310**, e240 – e242 (2007). URL <http://www.sciencedirect.com/science/article/pii/S0304885306023092>, proceedings of the 17th International Conference on Magnetism.

- [142] Russell, H. N. & Saunders, F. A. New Regularities in the Spectra of the Alkaline Earths. *Astrophysical Journal* **61**, 38 (1925).
- [143] Mravlje, J. *et al.* Coherence-incoherence crossover and the mass-renormalization puzzles in  $\text{Sr}_2\text{RuO}_4$ . *Phys. Rev. Lett.* **106**, 096401 (2011). URL <https://link.aps.org/doi/10.1103/PhysRevLett.106.096401>.
- [144] Yin, Z. P., Haule, K. & Kotliar, G. Kinetic frustration and the nature of the magnetic and paramagnetic states in iron pnictides and iron chalcogenides. *Nature Materials* **10**, 932–935 (2011). URL <https://www.nature.com/articles/nmat3120.pdf>.
- [145] Schafgans, A. A. *et al.* Electronic Correlations and Unconventional Spectral Weight Transfer in the High-Temperature Pnictide  $\text{BaFe}_{2-x}\text{Co}_x\text{As}_2$  Superconductor Using Infrared Spectroscopy. *Phys. Rev. Lett.* **108**, 147002 (2012). URL <https://link.aps.org/doi/10.1103/PhysRevLett.108.147002>.
- [146] Wang, N. L. *et al.* High energy pseudogap and its evolution with doping in Fe-based superconductors as revealed by optical spectroscopy. *Journal of Physics: Condensed Matter* **24**, 294202 (2012). URL <http://stacks.iop.org/0953-8984/24/i=29/a=294202>.
- [147] Kondo, T. *et al.* Orbital-Dependent Band Narrowing Revealed in an Extremely Correlated Hund’s Metal Emerging on the Topmost Layer of  $\text{Sr}_2\text{RuO}_4$ . *Phys. Rev. Lett.* **117**, 247001 (2016). URL <https://link.aps.org/doi/10.1103/PhysRevLett.117.247001>.
- [148] Kostin, A. *et al.* Imaging orbital-selective quasiparticles in the Hund’s metal state of FeSe. *Nature Materials* **17**, 869–874 (2018). URL <https://www.nature.com/articles/s41563-018-0151-0.pdf>.
- [149] Sprau, P. O. *et al.* Discovery of orbital-selective Cooper pairing in FeSe. *Science* **357**, 75–80 (2017). URL <http://science.sciencemag.org/content/357/6346/75>.
- [150] Haverkort, M. W., Elfimov, I. S., Tjeng, L. H., Sawatzky, G. A. & Damascelli, A. Strong Spin-Orbit Coupling Effects on the Fermi Surface of  $\text{Sr}_2\text{RuO}_4$  and  $\text{Sr}_2\text{RhO}_4$ . *Phys. Rev. Lett.* **101**, 026406 (2008). URL <https://link.aps.org/doi/10.1103/PhysRevLett.101.026406>.
- [151] Zabolotnyy, V. B. *et al.* Surface and bulk electronic structure of the unconventional superconductor  $\text{Sr}_2\text{RuO}_4$ : unusual splitting of the  $\beta$  band. *New Journal of Physics* **14**, 063039 (2012). URL <http://stacks.iop.org/1367-2630/14/i=6/a=063039>.
- [152] Zabolotnyy, V. *et al.* Renormalized band structure of  $\text{Sr}_2\text{RuO}_4$ : A quasiparticle tight-binding approach. *Journal of Electron Spectroscopy and Related Phenomena* **191**, 48 – 53 (2013). URL <http://www.sciencedirect.com/science/article/pii/S0368204813001655>.
- [153] Lee, W.-C., Arovas, D. P. & Wu, C. Quasiparticle interference in the unconventional metamagnetic compound  $\text{Sr}_3\text{Ru}_2\text{O}_7$ . *Phys. Rev. B* **81**, 184403 (2010). URL <https://link.aps.org/doi/10.1103/PhysRevB.81.184403>.

- [154] Puetter, C. M. & Kee, H.-Y. Identifying spin-triplet pairing in spin-orbit coupled multi-band superconductors. *EPL (Europhysics Letters)* **98**, 27010 (2012). URL <http://stacks.iop.org/0295-5075/98/i=2/a=27010>.
- [155] Kingma P., D. & Ba, J. Adam: A method for stochastic optimization. *arXiv:1412.6980* (2014). URL <https://arxiv.org/abs/1412.6980>.
- [156] Thomson, J. J. XL. Cathode rays. *The London, Edinburgh, and Dublin Philosophical Magazine and Journal of Science* **44**, 293–316 (1897). URL <https://doi.org/10.1080/14786449708621070>.
- [157] Hertz, H. Ueber einen Einfluss des ultravioletten Lichtes auf die electrische Entladung. *Annalen der Physik* **267**, 983–1000 (1887). URL <https://onlinelibrary.wiley.com/doi/abs/10.1002/andp.18872670827>.
- [158] Lenard, P. Ueber die lichtelektrische Wirkung. *Annalen der Physik* **313**, 149–198 (1902). URL <https://onlinelibrary.wiley.com/doi/abs/10.1002/andp.19023130510>.
- [159] Einstein, A. Über einen die Erzeugung und Verwandlung des Lichtes betreffenden heuristischen Gesichtspunkt. *Annalen der Physik* **322**, 132–148 (1905). URL <https://onlinelibrary.wiley.com/doi/abs/10.1002/andp.19053220607>.
- [160] Millikan, R. A. A direct photoelectric determination of Planck's "h". *Phys. Rev.* **7**, 355–388 (1916). URL <https://link.aps.org/doi/10.1103/PhysRev.7.355>.
- [161] Steinhardt, R. & Serfass, E. X-Ray photoelectron spectrometer for chemical analysis. *Analytical Chemistry* **23**, 1585–1590 (1951). URL <https://doi.org/10.1021/ac60059a019>.
- [162] Siegbahn, K. Electron spectroscopy – an outlook. *Journal of Electron Spectroscopy and Related Phenomena* **5**, 3 – 97 (1974). URL <http://www.sciencedirect.com/science/article/pii/036820487485005X>, the International Journal on Theoretical and Experimental Aspects of Electron Spectroscopy.
- [163] Lu, D. *et al.* Angle-resolved photoemission studies of quantum materials. *Annual Review of Condensed Matter Physics* **3**, 129–167 (2012). URL <https://doi.org/10.1146/annurev-conmatphys-020911-125027>.
- [164] Smallwood, C. L., Kaindl, R. A. & Lanzara, A. Ultrafast angle-resolved photoemission spectroscopy of quantum materials. *EPL (Europhysics Letters)* **115**, 27001 (2016). URL <http://stacks.iop.org/0295-5075/115/i=2/a=27001>.
- [165] Johnson, P. D. Spin-polarized photoemission. *Reports on Progress in Physics* **60**, 1217 (1997). URL <http://stacks.iop.org/0034-4885/60/i=11/a=002>.
- [166] Rotenberg, E. & Bostwick, A. microARPES and nanoARPES at diffraction-limited light sources: opportunities and performance gains. *Journal of Synchrotron Radiation* **21**, 1048–1056 (2014). URL <https://doi.org/10.1107/S1600577514015409>.
- [167] Fan, H. Y. Theory of photoelectric emission from metals. *Phys. Rev.* **68**, 43–52 (1945). URL <https://link.aps.org/doi/10.1103/PhysRev.68.43>.

- [168] Berglund, C. N. & Spicer, W. E. Photoemission studies of copper and silver: theory. *Phys. Rev.* **136**, A1030–A1044 (1964). URL <https://link.aps.org/doi/10.1103/PhysRev.136.A1030>.
- [169] Feibelman, P. J. & Eastman, D. E. Photoemission spectroscopy—Correspondence between quantum theory and experimental phenomenology. *Phys. Rev. B* **10**, 4932–4947 (1974). URL <https://link.aps.org/doi/10.1103/PhysRevB.10.4932>.
- [170] Randeria, M. *et al.* Momentum distribution sum rule for angle-resolved photoemission. *Phys. Rev. Lett.* **74**, 4951–4954 (1995). URL <https://link.aps.org/doi/10.1103/PhysRevLett.74.4951>.
- [171] Seah, M. P. & Dench, W. A. Quantitative electron spectroscopy of surfaces: A standard data base for electron inelastic mean free paths in solids. *Surface and Interface Analysis* **1**, 2–11 (1979). URL <https://onlinelibrary.wiley.com/doi/abs/10.1002/sia.740010103>.
- [172] Hüfner, S. *Photoelectron Spectroscopy: Principles and Applications* (Springer, Berlin Heidelberg New York, 2003).
- [173] Baumberger, F., Greber, T. & Osterwalder, J. Fermi surfaces of the two-dimensional surface states on vicinal Cu(111). *Phys. Rev. B* **64**, 195411 (2001). URL <https://link.aps.org/doi/10.1103/PhysRevB.64.195411>.
- [174] LaShell, S., Jensen, E. & Balasubramanian, T. Nonquasiparticle structure in the photoemission spectra from the Be(0001) surface and determination of the electron self energy. *Phys. Rev. B* **61**, 2371–2374 (2000). URL <https://link.aps.org/doi/10.1103/PhysRevB.61.2371>.
- [175] Fatuzzo, C. G. *et al.* Nodal Landau Fermi-liquid quasiparticles in overdoped  $\text{La}_{1.77}\text{Sr}_{0.23}\text{CuO}_4$ . *Phys. Rev. B* **89**, 205104 (2014). URL <https://link.aps.org/doi/10.1103/PhysRevB.89.205104>.
- [176] Valla, T. *et al.* Charge-density-wave-induced modifications to the quasiparticle self-energy in 2H-TaSe<sub>2</sub>. *Phys. Rev. Lett.* **85**, 4759–4762 (2000). URL <https://link.aps.org/doi/10.1103/PhysRevLett.85.4759>.
- [177] Nakatsuji, S. & Maeno, Y. Synthesis and single-crystal growth of  $\text{Ca}_{2-x}\text{Sr}_x\text{RuO}_4$ . *Journal of Solid State Chemistry* **156**, 26 – 31 (2001). URL <http://www.sciencedirect.com/science/article/pii/S0022459600989539>.
- [178] Als-Nielsen, J. & McMorrow, D. *Elements of Modern X-ray Physics* (Wiley, 2011), 2nd edn.
- [179] Attwood, D. *Soft X-Rays and Extreme Ultraviolet Radiation: Principles and Applications* (Cambridge University Press, New York, NY, USA, 2007), 1st edn.
- [180] Flechsig, U., Patthey, L. & Schmidt, T. Performance Measurements at the SLS Spectroscopy Beamline. *AIP Conference Proceedings* **705**, 316–319 (2004). URL <https://aip.scitation.org/doi/abs/10.1063/1.1757797>.

- [181] Hoesch, M. *et al.* A facility for the analysis of the electronic structures of solids and their surfaces by synchrotron radiation photoelectron spectroscopy. *Review of Scientific Instruments* **88**, 013106 (2017). URL <https://doi.org/10.1063/1.4973562>.
- [182] Shirley, D. A. High-Resolution X-Ray Photoemission Spectrum of the Valence Bands of Gold. *Phys. Rev. B* **5**, 4709–4714 (1972). URL <https://link.aps.org/doi/10.1103/PhysRevB.5.4709>.
- [183] Matsui, H. *et al.* BCS-Like Bogoliubov Quasiparticles in High- $T_c$  Superconductors Observed by Angle-Resolved Photoemission Spectroscopy. *Phys. Rev. Lett.* **90**, 217002 (2003). URL <https://link.aps.org/doi/10.1103/PhysRevLett.90.217002>.
- [184] Ingle, N. J. C. *et al.* Quantitative analysis of  $\text{Sr}_2\text{RuO}_4$  angle-resolved photoemission spectra: Many-body interactions in a model Fermi liquid. *Phys. Rev. B* **72**, 205114 (2005). URL <https://link.aps.org/doi/10.1103/PhysRevB.72.205114>.
- [185] Nakatsuji, S. *et al.* Mechanism of hopping transport in disordered Mott insulators. *Phys. Rev. Lett.* **93**, 146401 (2004). URL <https://link.aps.org/doi/10.1103/PhysRevLett.93.146401>.
- [186] Singh, D. J. Relationship of  $\text{Sr}_2\text{RuO}_4$  to the superconducting layered cuprates. *Phys. Rev. B* **52**, 1358–1361 (1995). URL <https://link.aps.org/doi/10.1103/PhysRevB.52.1358>.
- [187] Burganov, B. *et al.* Strain Control of Fermiology and Many-Body Interactions in Two-Dimensional Ruthenates. *Phys. Rev. Lett.* **116**, 197003 (2016). URL <https://link.aps.org/doi/10.1103/PhysRevLett.116.197003>.
- [188] Baier, J. *et al.* Thermodynamic properties of  $(\text{Ca}, \text{Sr})_2\text{RuO}_4$  in magnetic fields. *Physica B: Condensed Matter* **378–380**, 497 – 498 (2006). URL <http://www.sciencedirect.com/science/article/pii/S0921452606002420>, proceedings of the International Conference on Strongly Correlated Electron Systems.
- [189] Kresse, G. & Hafner, J. Ab initio molecular dynamics for open-shell transition metals. *Phys. Rev. B* **48**, 13115–13118 (1993). URL <https://link.aps.org/doi/10.1103/PhysRevB.48.13115>.
- [190] Blöchl, P. E. Projector augmented-wave method. *Phys. Rev. B* **50**, 17953–17979 (1994). URL <https://link.aps.org/doi/10.1103/PhysRevB.50.17953>.
- [191] Kresse, G. & Furthmüller, J. Efficient iterative schemes for ab initio total-energy calculations using a plane-wave basis set. *Phys. Rev. B* **54**, 11169–11186 (1996). URL <https://link.aps.org/doi/10.1103/PhysRevB.54.11169>.
- [192] Perdew, J. P., Burke, K. & Ernzerhof, M. Generalized gradient approximation made simple. *Phys. Rev. Lett.* **77**, 3865–3868 (1996). URL <https://link.aps.org/doi/10.1103/PhysRevLett.77.3865>.
- [193] Kresse, G. & Joubert, D. From ultrasoft pseudopotentials to the projector augmented-wave method. *Phys. Rev. B* **59**, 1758–1775 (1999). URL <https://link.aps.org/doi/10.1103/PhysRevB.59.1758>.

- [194] Aichhorn, M. *et al.* Dynamical mean-field theory within an augmented plane-wave framework: Assessing electronic correlations in the iron pnictide LaFeAsO. *Phys. Rev. B* **80**, 085101 (2009). URL <https://link.aps.org/doi/10.1103/PhysRevB.80.085101>.
- [195] Parcollet, O. *et al.* TRIQS: A toolbox for research on interacting quantum systems. *Computer Physics Communications* **196**, 398 – 415 (2015). URL <http://www.sciencedirect.com/science/article/pii/S0010465515001666>.
- [196] Aichhorn, M. *et al.* TRIQS/DFT tools: A TRIQS application for ab initio calculations of correlated materials. *Computer Physics Communications* **204**, 200 – 208 (2016). URL <http://www.sciencedirect.com/science/article/pii/S0010465516300728>.
- [197] Blaha, P., Schwarz, K., Madsen, G. K. H., Kvasnicka, D. & Luitz, J. *WIEN2K, An Augmented Plane Wave + Local Orbitals Program for Calculating Crystal Properties* (Karlheinz Schwarz, Techn. Universität Wien, Austria, 2001).
- [198] Gull, E. *et al.* Continuous-time Monte Carlo methods for quantum impurity models. *Rev. Mod. Phys.* **83**, 349–404 (2011). URL <https://link.aps.org/doi/10.1103/RevModPhys.83.349>.
- [199] Seth, P., Krivenko, I., Ferrero, M. & Parcollet, O. TRIQS/CTHYB: A continuous-time quantum Monte Carlo hybridisation expansion solver for quantum impurity problems. *Computer Physics Communications* **200**, 274 – 284 (2016). URL <http://www.sciencedirect.com/science/article/pii/S001046551500404X>.
- [200] Dang, H. T., Mravlje, J., Georges, A. & Millis, A. J. Electronic correlations, magnetism, and Hund’s rule coupling in the ruthenium perovskites SrRuO<sub>3</sub> and CaRuO<sub>3</sub>. *Phys. Rev. B* **91**, 195149 (2015). URL <https://link.aps.org/doi/10.1103/PhysRevB.91.195149>.
- [201] Iwasawa, H. *et al.* Interplay among Coulomb Interaction, Spin-Orbit Interaction, and Multiple Electron-Boson Interactions in Sr<sub>2</sub>RuO<sub>4</sub>. *Phys. Rev. Lett.* **105**, 226406 (2010). URL <https://link.aps.org/doi/10.1103/PhysRevLett.105.226406>.
- [202] Iwasawa, H. *et al.* High-Energy Anomaly in the Band Dispersion of the Ruthenate Superconductor. *Phys. Rev. Lett.* **109**, 066404 (2012). URL <https://link.aps.org/doi/10.1103/PhysRevLett.109.066404>.
- [203] Kaminski, A. *et al.* Identifying the background signal in angle-resolved photoemission spectra of high-temperature cuprate superconductors. *Phys. Rev. B* **69**, 212509 (2004). URL <https://link.aps.org/doi/10.1103/PhysRevB.69.212509>.
- [204] Matt, C. E. *et al.* Direct observation of orbital hybridisation in a cuprate superconductor. *Nature Communications* **9**, 972 (2018). URL <https://doi.org/10.1038/s41467-018-03266-0>.
- [205] Horio, M. *et al.* Two-dimensional type-II Dirac fermions in layered oxides. *Nature Communications* **9**, 3252 (2018). URL <https://doi.org/10.1038/s41467-018-05715-2>.

- [206] Nicolaou, A. *et al.* Experimental Study of the Incoherent Spectral Weight in the Photoemission Spectra of the Misfit Cobaltate  $[\text{Bi}_2\text{Ba}_2\text{O}_4][\text{CoO}_2]_2$ . *Phys. Rev. Lett.* **104**, 056403 (2010). URL <https://link.aps.org/doi/10.1103/PhysRevLett.104.056403>.
- [207] de la Torre, A. *et al.* Coherent Quasiparticles with a Small Fermi Surface in Lightly Doped  $\text{Sr}_3\text{Ir}_2\text{O}_7$ . *Phys. Rev. Lett.* **113**, 256402 (2014). URL <https://link.aps.org/doi/10.1103/PhysRevLett.113.256402>.
- [208] Khaliullin, G. Excitonic magnetism in Van Vleck-type  $d^4$  Mott insulators. *Phys. Rev. Lett.* **111**, 197201 (2013). URL <https://link.aps.org/doi/10.1103/PhysRevLett.111.197201>.
- [209] Kunkemöller, S. *et al.* Highly anisotropic magnon dispersion in  $\text{Ca}_2\text{RuO}_4$ : Evidence for strong spin orbit coupling. *Phys. Rev. Lett.* **115**, 247201 (2015). URL <https://link.aps.org/doi/10.1103/PhysRevLett.115.247201>.
- [210] Puchkov, A. V. *et al.* Layered ruthenium oxides: from band metal to Mott insulator. *Phys. Rev. Lett.* **81**, 2747–2750 (1998). URL <https://link.aps.org/doi/10.1103/PhysRevLett.81.2747>.
- [211] Mizokawa, T. *et al.* Spin-orbit coupling in the Mott insulator  $\text{Ca}_2\text{RuO}_4$ . *Phys. Rev. Lett.* **87**, 077202 (2001). URL <https://link.aps.org/doi/10.1103/PhysRevLett.87.077202>.
- [212] Marzari, N. & Vanderbilt, D. Maximally localized generalized Wannier functions for composite energy bands. *Phys. Rev. B* **56**, 12847–12865 (1997). URL <https://link.aps.org/doi/10.1103/PhysRevB.56.12847>.
- [213] Souza, I., Marzari, N. & Vanderbilt, D. Maximally localized Wannier functions for entangled energy bands. *Phys. Rev. B* **65**, 035109 (2001). URL <https://link.aps.org/doi/10.1103/PhysRevB.65.035109>.
- [214] Park, K. T. Electronic structure calculations for layered  $\text{LaSrMnO}_4$  and  $\text{Ca}_2\text{RuO}_4$ . *Journal of Physics: Condensed Matter* **13**, 9231 (2001). URL <http://stacks.iop.org/0953-8984/13/i=41/a=313>.
- [215] Liu, G.-Q. Spin-orbit coupling induced Mott transition in  $\text{Ca}_{2-x}\text{Sr}_x\text{RuO}_4$  ( $0 \leq x \leq 0.2$ ). *Phys. Rev. B* **84**, 235136 (2011). URL <https://link.aps.org/doi/10.1103/PhysRevB.84.235136>.
- [216] Woods, L. M. Electronic structure of  $\text{Ca}_2\text{RuO}_4$ : A comparison with the electronic structures of other ruthenates. *Phys. Rev. B* **62**, 7833–7838 (2000). URL <https://link.aps.org/doi/10.1103/PhysRevB.62.7833>.
- [217] Karolak, M., Wehling, T. O., Lechermann, F. & Lichtenstein, A. I. General DFT + + method implemented with projector augmented waves: electronic structure of  $\text{SrVO}_3$  and the Mott transition in  $\text{Ca}_{2-x}\text{Sr}_x\text{RuO}_4$ . *Journal of Physics: Condensed Matter* **23**, 085601 (2011). URL <http://stacks.iop.org/0953-8984/23/i=8/a=085601>.

- [218] Sutter, D. *et al.* Hallmarks of Hunds coupling in the Mott insulator Ca<sub>2</sub>RuO<sub>4</sub>. *Nature Communications* **8**, 15176 EP – (2017). URL <http://dx.doi.org/10.1038/ncomms15176>.

## Acknowledgements

The list for whom I am grateful for is long. During my PhD project I have received advice, guidance and support from Johan Chang, who gave me the great opportunity to emancipate myself as a scientist and as a person. I always benefited tremendously from our discussions and Johan's constructive criticism. Johan always helped me to expand my knowledge and skills as an experimentalist.

I would like to thank Jürg Osterwalder, who during my Bachelor, Master and PhD studies taught and inspired me through the whole spectrum of condensed matter physics. As I got to know Moritz Hösch during our experiments at his beamline, I learned to appreciate his expertise and knowledge in the ARPES methodology and strongly correlated systems. Both Jürg and Moritz helped me to push the PhD project into the right direction.

There are many people and experts that I would like to thank, who helped me with details in all aspects relevant to my education, personal and scientific. I am grateful for advice and physics wisdom from Hugo Keller, Andreas Schilling, Titus Neupert and René Monnier. Starting from my time as a technician, I have picked up and learned many things from Cornel Andreoli, Martin Klöckner and Matthias Hengsberger. The bulk of my technical knowledge in UHV technology and engineering stem from working with Urs Maier and Dominik Rechsteiner. Dominik joined our group so we can continue our promising projects together.

The time spent in our synchrotron office at Irchel was a great pleasure. It was fun to discuss random topics with Oleh about life, journal referees, science, data analysis and new blackboard posters. Christian was only for a short time in our office, but our shared beamtimes are stuff of legends and I learned tremendously about nuances in ARPES experiments. Kevin (the real one) and I have an almost commensurate time overlap regarding our super cool student life at the university. He encouraged me to immerse myself in python and we exchanged a lot of data-analysis knowledge

during and besides our beamtimes. I would also like to thank Masafumi, the silent hard worker next to me. He is a master of night shifts and never loses focus in his scientific efforts. Before he leaves for Japan one day, he must try a double espresso. Also many thanks to the synchrotron team for nurturing my plant, that is now a part of the office.

Related to my development as a physicist, I am grateful for having learned from many different personalities over the years. Claudia Fatuzzo and Simon Moser supported me greatly, especially in the first important experiments. ARPES beamtimes at the ALS are really great, even the night shifts. I would also like to thank Yasmine, who eagerly helped us in essentially all beamtimes. It didn't matter where we went for experiments, she came to help us in our endeavours and was especially skilled in advising and creating a comfy atmosphere. I learned much during my research stay at the university of Salerno. The crystal grower team, consisting of Antonio Vecchione, Rosalba Fittipaldi and Veronica Granata are true masters of their craft. None of our experiments on ruthenates have been possible without their work. Also many thanks to Mario Cuoco and Fiona Forte for their theory efforts in our mutual projects. During my stay we had many fruitful discussions. I would also like to thank all other present and former members group members, Lakshmi, Daniel, Jaewon, Qisi, Kevin (the other one) and many others. The size of our group evolves and became very dynamic.

Finally, I want to thank my family and friends who contrasted intense times during my study. Special thanks go to my two flatmates Martin and Jascha, who themselves work hard on their own studies. Together we synergistically inspire each other to focus on studying, having nice dinners and going on trips. Closely entangled, I would like to thank Ö, Alex and Robin for shenanigans and (international) adventures. Additionally, I would like to thank the Branzuela-, Burke- and Sutter-clan for personal growth and good times. I am tremendously grateful to Arianne, who supports and inspires me on a daily basis. Last but not least I want to thank my beloved parents, Leah and Reto and my sister Larry for their endless support and warmth.

THANK YOU!

# Curriculum Vitæ



**Denys Sutter**  
Graue Gasse 12  
8001 Zürich  
[dsutter@physik.uzh.ch](mailto:dsutter@physik.uzh.ch)

## Education

- 2015–2019 **Fast-Track PhD in Experimental Condensed Matter Physics**  
UZH, Laboratory for Quantum Matter Research, Group J. Chang
- 2015–2016 **Master of Science in Physics – Grade 5.9 of 6.0**  
UZH, Laboratory for Quantum Matter Research, Group J. Chang
- 2010–2015 **Bachelor of Science in Physics – Grade 5.6 of 6.0**  
UZH, Surface Physics, Group J. Osterwalder
- 2009–2010 **Examination "Passerelle" for University Studies**  
AKAD Zürich

## Professional Experience

- 2008–2015 **Physics Laboratory Technician**, Ferrovac GmbH Zurich
- 2004–2008 **Physics Laboratory Technician**, Apprenticeship, ETH Zurich



# List of publications

## Published / Accepted

1. M. Horio, K. Hauser, Y. Sassa, Z. Mingazheva, **D. Sutter**, K. Kramer, A. M. Cook, E. Nocerino, O. K. Forslund, O. Tjernberg, M. Kobayashi, A. Chikina, N. B. M. Schröter, J. A. Krieger, T. Schmitt, V. N. Strocov, S. Pyon, T. Takayama, H. Takagi, O.J. Lipscombe, S.M. Hayden, M. Ishikado, H. Eisaki, T. Neupert, M. Måansson, C.E. Matt, J. Chang;  
*Three-dimensional Fermi surface of overdoped La-based cuprates*  
Physical Review Letters **121**, 077004 (2018)
2. M. Horio, C.E. Matt, K. Kramer, **D. Sutter**, A.M. Cook, Y. Sassa, K. Hauser, M. Måansson, N.C. Plumb, M. Shi, O.J. Lipscombe, S.M. Hayden, T. Neupert, J. Chang;  
*Two-dimensional type-II Dirac fermions in layered oxides*  
Nature Communications **9**, 3252 (2018)
3. C.E. Matt, **D. Sutter**, A.M. Cook, Y. Sassa, M. Mansson, O. Tjernberg, L. Das, M. Horio, D. Destraz, C.G. Fatuzzo, K. Hauser, M. Shi, M. Kobayashi, V.N. Strocov, T. Schmitt, P. Dudin, M. Hoesch, S. Pyon, T. Takayama, H. Takagi, O.J. Lipscombe, S.M. Hayden, T. Kurosawa, N. Momono, M. Oda, T. Neupert, J. Chang;  
*Direct observation of orbital hybridisation in a cuprate superconductor*  
Nature Communications **8**, 972 (2018)
4. **D. Sutter**, C.G. Fatuzzo, S. Moser, M. Kim, R. Fittipaldi, A. Vecchione, V. Granata, Y. Sassa, F. Cossalter, G. Gatti, M. Grioni, H.M. Ronnow, N.C. Plumb, C.E. Matt, M. Shi, M. Hoesch, T.K. Kim, T.-R. Chang, H.-T. Jeng, C. Jozwiak, A. Bostwick, E. Rotenberg, A. Georges, T. Neupert, J. Chang;  
*Hallmarks of Hund's coupling in the Mott insulator  $Ca_2RuO_4$*   
Nature Communications **8**, 15176 (2017)
5. G. Mette, **D. Sutter**, Y. Gurdal, S. Schnidrig, B. Probst, M. Iannuzzi, J. Hutter, R. Alberto, J. Osterwalder;  
*From porphyrins to pyrphyrins: Adsorption study and metalation of a molecular catalyst on Au(111)*  
Nanoscale **8**, 7958 (2016)

## Submitted

1. **D. Sutter**, M. Kim, C.E. Matt, M. Horio, R. Fittipaldi, A. Vecchione, V. Granata, K. Hauser, Y. Sassa, G. Gatti, M. Grioni, M. Hoesch, T.K. Kim, E. Rienks, N.C. Plumb, M. Shi, T. Neupert, A. Georges J. Chang;  
*Orbitally-selective breakdown of Fermi liquid quasiparticles in  $Ca_{1.8}Sr_{0.2}RuO_4$*   
Physical Review Letters, in review

